Fluctuation Electron Microscopy of

Amorphous and Polycrystalline Materials

by

Aram Rezikyan

A Dissertation Presented in Partial Fulfillment
of the Requirements for the Degree
Doctor of Philosophy

Approved April 2015 by the
Graduate Supervisory Committee:

Michael M. J. Treacy, Chair
Peter Rez
David J. Smith
Martha R. McCartney

ARIZONA STATE UNIVERSITY

May 2015

ABSTRACT

Fluctuation Electron Microscopy (FEM) has become an effective materials' structure characterization technique, capable of probing medium-range order (MRO) that may be present in amorphous materials. Although its sensitivity to MRO has been exercised in numerous studies, FEM is not yet a quantitative technique. The holdup has been the discrepancy between the computed kinematical variance and the experimental variance, which previously was attributed to source incoherence. Although high-brightness, high coherence, electron guns are now routinely available in modern electron microscopes, they have not eliminated this discrepancy between theory and experiment. The main objective of this thesis was to explore, and to reveal, the reasons behind this conundrum.

The study was started with an analysis of the speckle statistics of tilted dark-field TEM images obtained from an amorphous carbon sample, which confirmed that the structural ordering is sensitively detected by FEM. This analysis also revealed the inconsistency between predictions of the source incoherence model and the experimentally observed variance.

FEM of amorphous carbon, amorphous silicon and ultra nanocrystalline diamond samples was carried out in an attempt to explore the conundrum. Electron probe and sample parameters were varied to observe the scattering intensity variance behavior. Results were compared to models of probe incoherence, diffuse scattering, atom displacement damage, energy loss events and multiple scattering. Models of displacement decoherence matched the experimental results best.

Decoherence was also explored by an interferometric diffraction method using bilayer amorphous samples, and results are consistent with strong displacement decoherence in addition to temporal decoherence arising from the electron source energy spread and energy loss events in thick samples.

It is clear that decoherence plays an important role in the long-standing discrepancy between experimental FEM and its theoretical predictions.

ACKNOWLEDGEMENTS

I would like to express the deepest gratitude to my adviser and the committee chair, Professor Michael Treacy, for his excellent guidance, generous support and constant patience. Despite the family tragedy that he experienced during the second year of our teamwork he continued guiding me towards my doctorate degree with his courage towards new challenges, not to mention his outstanding knowledge, experience in the field of study and unsurpassed teaching skills. He is an excellent mentor who was always there to cheer me up.

I want to sincerely thank Professor Peter Rez for his extremely useful advice and indispensable assistance with initiation of my fluctuation microscopy experiments, as well as for involving me later in his interesting studies of nitrogen vacancies in diamond and calcite studies. He was like my second adviser and I always felt his support and willingness to help with any questions.

Special thanks to Professors David Smith and Martha McCartney for taking care of me during my first year at Arizona State University and for providing me with excellent atmosphere for adjusting and studying in a new research group. I am thankful that I could always consult with the experts in experimental electron microscopy with such a huge experience. I deeply appreciate their helpful advice on all matters and that they were always open for questions and discussions during the rest of my attendance at ASU.

I would like to acknowledge productive collaboration with Professor Robert Nemanich's group and express appreciation for his kind and generous financial support

for electron microscope time. Also thank you to his group members, Franz Koeck and Tianyin Sun for fruitful discussions and providing some of the samples for my research.

I gratefully acknowledge the Department of Energy for funding under contract number DE-SC0004929 and the use of facilities within the LeRoy Eyring Center for Solid State Science (LECSSS) at Arizona State University. Thank you for your help to all of the present and former stuff of LECSSS including Zhenquan Liu, late Jason Ng, Gordon Tam, Grant Baumgardner, Kenneth Mossman, Karl Weiss and Sisouk Phrasavath. Special thanks to John Mardinly and Toshihiro Aoki for technical support with the instruments in ASU Aberration-Corrected Microscopy Center for they were always patient and willing to help and give their best suggestions.

I am grateful to fellow students and colleagues for their kindness, friendship and support. Colby Dowson, Vitaliy Kapko, Jae Jin Kim, Kai He, Dexin Kong, Bryant Doss, Rory Staunton, Allison Boley, Sahar Hihath, David Cullen, Zhaofeng Gan, Wenfeng Zhao, Dinghao Tang, Luing Lee, Ajit Dhamdhere are among them.

I would also like to thank Valery Smirnov and Alla Mityureva, my former advisers at Saint Petersburg State University, who actually guided my way to Arizona State University. It would not have been possible for me to start the doctoral program here at ASU without their kind effort.

Last, but by no means least, I would like to express my deepest appreciation to my family and friends some of whom were already mentioned. They were always supporting and encouraging me throughout my education and stood by me through the good times and bad.

TABLE OF CONTENTS

Page

LIST OF TABLES vii

LIST OF FIGURES viii

CHAPTER

1. INTRODUCTION 1

    1.1. Disordered Materials. Applications. 1

    1.2. Structural Characterization Techniques. 10

    1.3. Overview of Fluctuation Electron Microscopy 17

2. EXPERIMENTAL PROCEDURES AND DATA PROCESSING 26

    2.1. Experimental 26

    2.2. Samples' Descriptions and Preparation Procedures 29

    2.3. Data Processing and Modeling 33

3. TILTED DARK-FIELD TEM MODE FLUCTUATION ELECTRON MICROSCOPY STUDIES OF AMORPHOUS CARBON 36

    3.1. Information Theory Aspects of Tilted Dark-Field TEM images 36

    3.2. Results and Discussion. 44

4. DECOHERENCE IN SCANNING TRANSMISSION FLUCTUATION ELECTRON MICROSCOPY OF AMORPHOUS CARBON AND AMORPHOUS SILICON. BEAM ENERGY DEPENDENCE. 51

    4.1. Probe Coherence and Scattering Decoherence Effects. 51

    4.2. Decoherence. Beam Energy Effect. 60

CHAPTER Page

5. DECOHERENCE IN STFEM OF AMORPHOUS CARBON AND AMORPHOUS SILICON. SAMPLE THICKNESS DEPENDENCE. INTERFEROMETRIC BILAYER DIFFRACTION..... 63

5.1. Sample Thickness Dependence of Variance..... 63

5.2. FEM of FIB-Prepared Multi-Step Amorphous Carbon 64

5.3. FEM of Multi-Layer Amorphous Carbon..... 68

5.4. Interferometric Diffraction in Bilayer Amorphous Carbon Sample 71

6. FLUCTUATION ELECTRON MICROSCOPY OF NITROGEN-DOPED ULTRA NANO-CRYSTALLINE DIAMOND FILMS..... 86

6.1. Brief Overview of Ultra Nano-Crystalline Diamond..... 86

6.2. Structural Characterization of UNCD films. 86

6.3. Decoherence in STFEM Explored Through Electron Dose Variation on UNCD Films..... 94

7. CONCLUSION..... 97

REFERENCES 100

APPENDIX

A GAMMA DISTRIBUTION DERIVATION FROM THE PRINCIPLE OF MAXIMUM ENTROPY 119

LIST OF TABLES

Table Page

1. STFEM Probe Characteristics..... 27

2. List of a-Si Bilayer Separation Values Obtained by the Fringe Analysis..... 78

LIST OF FIGURES

Figure Page

1. Schematic of the FEM Experiment in the Tilted Dark-Field TEM Mode. The Specimen is Illuminated by a Tilted, Plane-Wave Electron Beam. The Objective Aperture is Aligned with the Optical Axis of the Microscope in Order to Select Only Diffracted Beams and Block the Unscattered Beam. The Scattered Electrons Entering the Objective Aperture Contribute to the Tilted Dark-Field Image Formed Further Down the Column. The Tilt Angle is Varied and Images are Collected at Each Tilt Angle. 22
2. Schematic of the FEM Experiment in the STEM Mode (Stfem). The Specimen is Illuminated by a Small-Convergence, Focused Electron Probe that is Scanned Over a Grid of Positions on the Sample. Diffraction Patterns are Collected at Each Position of the Electron Probe. 23
3. Schematic of the Experimental STFEM Data Processing. The Stack of Diffraction Patterns, Which in Its Entirety is Nothing Less Than $I(x, y, k_x, k_y)$ Data, is Used to Calculate the Normalized Variance. The Resulting Variance Map is Radially Averaged to Give a Plot of Normalized Variance Versus the Scattering Vector Amplitude $V(k)$. 23
4. HAADF Intensity from Five Quantized-Thickness Areas with a 30 nm Quantum Step of an Amorphous Carbon Film, Fitted to the Curve Giving a Simple Approximation of HAADF Intensity Thickness Dependence. The Fit Shows that the Data Points are in the Linear Dependence Region. 29

Figure Page

5. BF TEM Image of a Curled-Up Region of a-C Film. the Curled-Up Fragment is Lying on the a-C Film Support Film. 30

6. Secondary-Electron SEM Images Showing the Multi-Layer Carbon Films Preparation Process. (a) – the Existing 30-nm Carbon Support Film is Torn from the Cu Grid by the Omniprobe^{tm} Pt Needle and Rolled Into a Conical Or Cylindrical Shape. (b) – the Assembly is Moved to a Clean Area of Carbon Film by Inserting and Moving the Needle, and Dropped on a Fresh, Unaffected Support Film Area. (c) – the Omniprobe^{tm} Needle is Withdrawn. (d) – the Needle Applies Pressure to the Exterior Curved Carbon Walls. (e) – the Rolled Film Starts to Crack. (f) – the Needle is "Stroked" Along the Cracks to Complete the Flattening Process to Produce a Layered Structure..... 31

7. SEM Image of a Fragment of a-Si Attached, Presumably Through Van Der Waals Force, to the Film from One End and Loose from the Other, Providing a Bilayer Structure with Variety of Gap Values. 32

8. Normalized Variance Versus Scattering Vector for a Set of Tilted Dark-Field Images of Amorphous Carbon Taken for 30 Different Tilts at 200 keV. Peaks of Variance Indicate MRO. The Peak Near 3 Nm^{-1} May Be Due to Graphitic (002) Planes, the Other Two Peaks at About 5 nm^{-1} and 9 nm^{-1} are Most Probably Due to the Diamond (111) and (220), (311), (222) Reflections Combined, Respectively. 44

9. (a) – Tilted Dark-Field Image of the Amorphous Carbon Sample at the Tilt Corresponding to the Dip at 7.1 Nm^{-1} of the Normalized Variance Plot

Figure Page

Above. (b) – The Intensity Histogram of this Image, and the Fit to a Gamma Distribution with $m \approx 42$, $\langle I \rangle \approx 100$..... 45

10. (a) – Tilted Dark-Field Image of the Amorphous Carbon Sample at the Tilt Corresponding to the Peak at About 5 nm^{-1} of the Normalized Variance Plot Above. (b) – The Intensity Histogram of this Image, and the Fit to a Gamma Distribution with $m \approx 26$, $\langle I \rangle \approx 100$..... 45

11. Histogram of Intensity of "Noisy" Images Obtained by Adding Shot Noise to the Original Image for Which the Intensity Histogram is a Gamma Distribution, with Parameters $m_0 = 30$ and $\langle I \rangle_0 = 100$. (a) $\langle I \rangle = 10$, the Fit Deviates Slightly from the "Noisy" Image Statistics as a Result of a Poor Signal to Noise Ratio. (b) $\langle I \rangle = 100$, Noise Does Not Introduce Any Significant Deviation from the Noise-Free Gamma Distribution..... 47

12. (a) – Ratio of the Parameter $\langle I \rangle_{fit}$ of the Gamma Distribution Fit to the Simulated $\langle I \rangle$ Versus $\langle I \rangle$. as the Signal to Noise Ratio Drops the Noise Starts Affecting the Mean at About $\langle I \rangle = 50$. Eventually, the Ratio Soars to the Point Where the Noise Clearly Dominates the Signal. (b) – Ratio of the Parameter m_{fit} of the Gamma Distribution Fit to the Original $m_0 = 30$ Versus $\langle I \rangle$. as the Signal to Noise Ratio Drops the Fitted Parameter m_{fit} Plummets..... 48

13. Illustration of Electron Probe Parameters, in a JEOL ARM200F Instrument Operated at 200 keV in the NBD-S Mode of the Condenser System with 10

Figure Page

μm Probe-Forming Aperture. Diffraction Speckle from a-Si, Unsaturated and Saturated Probe Images with Profile Insets are Presented for Two Different Probes, Both Having Nominal Diffraction Limited Resolution of About 2.4 nm. (a), (b) and (c) – Low Spatial Coherence (Probe2). (d), (e) and (f) – High Spatial Coherence (Probe 1). 52

14. Experimental 200 keV STFEM Data from a-Si Showing the Influence of Spatial Incoherence on the Normalized Variance. All Plots Were Obtained with a Nominal, Diffraction-Limited, Probe Resolution of 2.4 nm. Exposure Times Along with Electron Fluence Values for Each Case are Given in the Legend. There is About Factor of Four Difference in Peak Variance Between High (Probe1) and Low (Probe 2) Spatial Coherence Cases. 54

15. Normalized Variance Computed by Treacy, for Two Models of Amorphous Silicon, Assuming Randomized and Uncorrelated Atomic Displacements that are Induced by Interactions with the Electron Beam. Displacement Root-Mean Square Amplitudes, Between 0.0 and 0.15 nm are Presented. (a) – CRN Model, (b) – Random Model, (c) – Paracrystalline Model. Variance is Strongly Suppressed with Increasing R.M.S. Displacement Amplitude, Especially at High *k*. Peaks that Match Qualitatively the Experimental Data Emerge in the CRN Model as Opposed to the Random Model. The Red Trace in (a) is the High Spatial Coherence Experimental Data from Fig. 14. 56

16. Stationary-Probe Diffraction Patterns of a-Si (a) and (b) that Were Taken Sequentially with 3.2 Sec Exposure Using the Probe with 2.4 nm Nominal Resolution and 10^6 Electrons/(nm^2×sec) Electron Flux, and Their Difference (c), Which Highlights Twinkling of the Diffraction Speckle on Observable Timescales. 59

17. Normalized Variance Plots Computed for Paracrystalline Silicon Model, Compared with Experimental Data Obtained by STFEM for 80 kV (Probe 5) and 200 kV (Probe 3) Electrons for (a) – a-C Film and (b) – a-Si Film. The Suppression of the Experimental Variance is Arising from Both Illumination Spatial Incoherence (to Increase Fluence Rate), and from Displacement Decoherence. The Spatial Coherence, the Fluence (9×10^8 Electrons/Nm^2) and the Probe Size (About 1.5 nm) are Approximately the Same at Each Voltage (9×10^8 Electrons/Nm^2). The Normalized Variance at 200 kV in Both Samples is Strongly Suppressed Relative to that at 80 kV. More Severe Suppression at Higher-*k* Values is Observed in All Cases. 61

18. HAADF Stem Image of the Stepped a-C Sample Prepared by Ga FIB Milling, Taken at 200 keV. Relative Thicknesses are Indicated in Each Area. 65

19. Normalized Variance Plots for the Stepped a-C Sample, Which Was Prepared by FIB, Obtained at 200 keV Using a Probe with 1.5 nm Resolution. Relative Thicknesses for Each of the Steps are Indicated in the Plot Legends. (a) – 2 sec. Exposure of Individual Diffraction Patterns. The Large Peak at About 2.8 nm May Be Associated with the Ga-Ion Fib

Preparation. The Carbon Peaks are Almost Entirely Buried Under the Variance Background Introduced by the Diffraction Central Spot Shift Correction Procedure; (b) – 3 sec. Exposure. The Ga Peak is Partly Cut by the Saturated Central Spot. A Small Hole Was Burned by the Electron Probe in the Thinnest Area. All Other Areas Showed Carbon Contamination After STFEM Scans Which Means that Thicknesses Were Altered. Most Probably this Accounts for the Unexpected Variance Behavior with Thickness for the Probed Areas. 66

20. (a) – TEM Image Illustrating the Carbon Contamination at the 10×10 Grid of Electron Probe Positions Where STFEM Data Was Acquired from the 30 nm Thick Amorphous Carbon Film at 200 keV. the Tilted Array Indicates that the Specimen Was Drifting. The Circled Region is a Typical CCD Camera Artefact, a Particle on the Camera's Scintillator Film Generated by Insertion/Retraction of the Camera. The Standard Gatan's Gain Normalization Procedure Was Unable to Correct for the Contrast from Some of the Large Particles. (b) – HAADF STEM Image of the a-C Sample Treated with Ga-Ion Beam. Bright Spots Indicate Ga Contamination. 67

21. Multi-Layer Sequence of Carbon Films Arranged in a Step-Like Structure. this Comprises a 30 nm Thick Carbon Film Supporting a Four-Layer Stack of Sheets Which are Fragments of the Same Support Film. (a) – STEM BF Image. (b) – HAADF Stem Image with t/λ Values Indicated on Each Step Representing an Increment in Thickness of 30 nm..... 69

Figure Page

22. Normalized Variance Plots for the Multi-Layered a-C Sample Obtained at 200 keV Using a Probe with 1.5 nm Resolution. Each Trace Corresponds to a Different Number of Identical 30 nm Thick Layers Traversed by the Electron Beam. Two Different Sets of Areas Were Sampled Producing Figures (a) and (b). Gaps Between the Layers Most Probably Account for the Unexpected Variance Behavior in Some of the Areas..... 70

23. Optical Microscope View of the Amorphous Carbon Film About 30 nm Thick on a 300 Mesh 3 mm Copper Grid Showing Large-Scale Wrinkling, with Its a Bit More Magnified Image on the Right..... 71

24. (a) – Diffraction Pattern from a Bilayer of Amorphous Carbon Taken at 200 keV Using a Probe with 1.5 nm Resolution. (b) – Same Pattern 'Unwrapped' So that the Diffraction Rings are Horizontal. Intensity is Rescaled. Wavy Fringes are Visible on the Rings..... 72

25. A Bilayer with a Gap *L* and Each Layer Having Thickness *t*..... 73

26. Ewald Sphere Construction for a Bilayer Crystal Film with Superimposed Reciprocal Lattice Points of a Single-Layer Crystal Film. It Shows that the Ewald Sphere for a Convergent Probe, Having an Effective Thickness of 2α, Samples More the Reciprocal Lattice Points Farther from the Origin. 74

27. Schematic Explaining Fringes in Diffraction Patterns from a Crystalline Bilayer Structure. The Ewald Sphere Crosses the Finely-Spaced Bilayer Reciprocal Lattice Disks Producing the Characteristic Fringe Pattern Inside

the Diffraction Disk. More Realistic Picture of the Reciprocal Space Modulations Explains the Smoothness of the Fringes. 75

28. Illustration of the Bilayer Fringe Analysis. (a) – Diffraction Pattern from a Bilayer Amorphous Silicon Taken at 200 keV Using a Probe with 1.5 nm Resolution. (b) – Plot of $1/\lambda\bar{k}\Delta k$ Vs $\bar{k}$ Data Collected from the Pattern in (a) and the Linear Fit to the Data. Error Bars are Computed Assuming an Error of One Pixel in Locating Fringe Maxima. The Fit Gives the Bilayer Separation Value of About 640 nm. 77

29. Unwrapped Diffraction Patterns for 20-nm Thick Amorphous Si Bilayer. As the Gap Increases from (a) to (f) the Fringes Become Finer. They are Broken and Wiggly Thought the Azimuth Crating a Picture of "Rivulets". 79

30. Set of Unwrapped Diffraction Patterns from Different Models of Bilayer a-Si with 300 nm Separation Computed by M. Treacy for 200 keV Electron Probe with 1.5 nm Resolution. (a) – Random Model. (b) –Polycrystalline Model. (c) – Paracrystalline Model. (d) – Continuous Random Network Model. (e) – Experimental Data, Which is a Fragment of Fig. 29 (d). Wiggly Fringes and "Rivulets" of Fringes Along *k* Appear in All Models and in the Data. Experimentally, Fringe Contrast Fades for $k > 7$ nm^{-1}. Fringe Separation for the Model with 300 nm Gap Matches Within the Error Bar with that for the Experimental Bilayer with About 350 nm Gap..... 80

31. Set of Unwrapped Diffraction Patterns of Bilayer a-Si. Only Small Fragments are Shown Corresponding to About 60 Degree Range of

Azimuthal Angle. The Gap Increases from Left to Write. The Horizontal Red Lines Show Approximate Boundaries Past Which the Fringes Fade. They Move to Lower *k* Values as the Gap Widens. The Region Numbers 3, 4, 6 and 9 Correspond to Those in Table 2, and Have Bilayer Separations 180 nm, 350 nm, 640 nm and 1100 nm, Respectively..... 81

32. Fringe Contrast in Diffraction Patterns from the Bilayer Amorphous Silicon. Four Regions of the Sample with Different Bilayer Separations are Presented. The Region Numbers 3, 4, 6 and 9 Correspond to Those in Table 2, and Have Bilayer Separations 180 nm, 350 nm, 640 nm and 1100 nm, Respectively. The Contrast Fades at Lower *k*-Values with Increasing Separation. The Peaks at Characteristic c-Si Wavevector Values Probably Arise Because the Displacement Decoherence Affects the Scattering from the Ordered Regions Less Than the Disordered Matrix. 82

33. The Mean Fringe Contrast Within the First Two Peaks (2.8 – 3.6 nm^{-1}, and 5.0 – 6.0 nm^{-1}) as a Function of Layer Separation. the Error Bars in Contrast Represent the Spread in Contrast Values About Each Mean Value. The Fit is to a Gaussian-Related Function, Returning a Standard Deviation (Effective Coherence Length) of 225 nm. The Constant Contrast Offset of About 0.05 May Be Arising Because Some of the Weak Fringes that We Measure are Illusory. (Courtesy of M. Treacy)..... 84

34. Dark-Field TEM Imaging of the UNCD Film. (a) – Low-Resolution BF TEM Image of the Cross-Sectional UNCD Sample. (b) – Area Select on the

UNCD Layer by a Selected Area Aperture. (c) – Selected Area Diffraction Pattern (SADP). The Red Arrow Shows the Reflection Selected Later to Form a Dark-Field Image. (d) – Dark-Field TEM Image of the Selected Area. Grain Sizes are Indicated in Red. 88

35. Aberration Corrected BF STEM Image of the Cross Section View of the UNCD Film Grown on a (100) Si Substrate, Taken at 200 keV (a) – Area Close to the Tip of the Wedge-Shaped Sample. Part of the Area Closer to the Tip (i.e. to the Left) Has Been Melted by the Fib Treatment. UNCD Layer is Polycrystalline. Thin Amorphous Layer of About 1.5 nm is Formed Between the Si and Uncd Layers. (b) – Magnified View of the Uncd Layer Showing the Grain Structure. (c) – Magnified View of the Si Substrate at [110] Zone Axis with Resolved 136 Pm Dumbbells. 89

36. Chemical Analysis of the Interlayer Between the Si Substrate and the UNCD Film. (a) – the EELS Linescan Area on a STEM BF Image (Not the Actual Survey Image for Linescan). The Scale Mark Has the Actual Scan Line Length. (b) – Line Profiles Obtained by a Probe of About 0.5 nm of C, Si and O. the Relative Quantification of the Corresponding Elements Gives About 69%, 26% and 5% Respectively. 90

37. (a) – Tem Image of the FIB-Liftout Sample Consisting of a 100 Si Substrate, UNCD Layer, AuPd Coating Layer and Pt Layer, Taken at 200 keV. White, Numbered Squares Show Approximately the Area Where FEM Data Was Collected. Dark Elongated Spots on Si and UNCD Layers are

Beam Contamination Spots. The Tip of the Sample is Partly Amorphized by the Focused Ga-Ion Beam During Preparation. (b) – Typical Diffraction Pattern from the Amorphized Tip Area. (c) – Typical Diffraction Pattern from a Thicker Area. 91

38. Normalized Variance Plots for the UNCD Film Obtained by 200 keV STFEM Using Condenser System Configuration that Gives a 1.5 nm Nominal Diffraction-Limited Resolution. Each Trace Corresponds to One of the Square Areas Indicated in Fig. 37 (a) Exposure Time Was Adjusted to 0.5 sec Resulting in About 1.22×10^{8} Electrons/nm^2 Fluence. Large Diamond Peaks are Observed in All Areas, Except at the Amorphized Tip (1 and 5). the Graphite 200 Peak is Observed at About 2.9 nm in the Area 1 Along with Two Diamond Peaks. 92

39. Normalized Variance Plot From the UNCD Sample. The STFEM Data Was Collected From An 8×8 Grid Of Probe Positions With 8 nm Step, Located At The Tip Of The Cross Sectional FIB-Liftout Sample, Which Was Amorphized By The FIB And Ar Plasma Thinning. Exposure Time Was Adjusted To 1 Sec Resulting In About 2.44×10^{8} Electrons/nm^2 Fluence. Both Cubic And Hexagonal Carbon Peaks Are Present. 93

40. (a) – High-Resolution Tem Image of the UNCD Layer at the Amorphized Tip After Additional Ar Plasma Thinning, Taken at 200 keV. the White Square Shows the Area in Which FEM Data Was Collected. (b) – Normalized Variance Plot Showing Both Cubic and Hexagonal Carbon

Peaks as Well as the Peak at 7.1 nm^{-1} Which is a Signature of the Curved Carbon Allotropes. STFEM Data Was Collected from a 5×5 Grid of Probe Positions with 8 nm Step. Exposure Time Was Adjusted to 0.2 sec Resulting in About 0.49×10^8 Electrons/nm^2 Fluence. 94

41. Experimental STFEM Normalized Variance Plots for About 60 nm Thick UNCD Film Area Obtained at 80 keV. the Probe 4 Configuration of the Condenser System Provided About 2 nm Resolution and 0.84×10^9 Electrons/(nm^2×sec). Strong Variance Peaks Arise at the Cubic Diamond Reflections, 111, 220, Etc. Variance Peaks are Suppressed More with Longer Exposure in Accordance with the Decoherence Argument. 95

42. Experimental STFEM Normalized Variance Plots for 50-nm Thick Amorphous Si_3N_4 Film Obtained at 200 keV. The Probe 3 Configuration of the Condenser System Provided About 1.5 nm Resolution and 2.44×10^8 Electrons/(nm^2×sec). Low Exposure Time Variance is Dominated by Shot Noise 96

CHAPTER 1

INTRODUCTION

1.1. Disordered Materials. Applications.

During the last four decades there has been growing interest in disordered materials. It is driven by both the successful applications of such materials in industry, and by promising future applications. Dramatic changes triggered by syntheses of new functional and structural disordered materials occurred in the field of energy conversion, data storage, electricity storage, pharmacology etc.

One advantage of disordered materials should be noted from the very beginning – they are usually easier to prepare in large area and desired shape in a cost-effective way compared to polycrystalline or crystalline materials. Hence their application in large electronic devices such as flat panel displays (FPDs), scanners, solar cells, position sensors etc. Oxide glasses, glassy polymers and ceramics are widely used in our everyday life, bottles and window glass being the most obvious examples. In the following I present a brief review of disordered materials and their applications.

One of the biggest inventions of the 20^{th} century, xerography, stemmed from amorphous-Se-based photoreceptors [1, 2] and became a multibillion dollar industry. Today chalcogenide-based photoconductors are still of much interest for various imaging applications, including digital medical X-ray imaging [3, 4]. In recent years another emerging technology based on phenomena discovered in the 20^{th} century, the electrical reversible memory switching phenomena [5], generated much interest in phase-change chalcogenide glasses [6]. Fast reversible amorphous-to-crystalline phase transformations, and differences in the optical and electrical properties of the two phases are key features

of chalcogenides that are utilized in optical memory devices. An example is the DVD-RW technology, as well as in phase-change memory technology, such as PRAM, which features high density, inherent stability and short switching time [7-10].

More recently researchers in the field of electricity storage have turned their attention to amorphous materials for battery cathodes. The so called disordered Li-excess materials appear to be promising candidates for significant improvement of battery cathode performance [11]. These are disordered transition metal oxides with increased concentration of Li atoms as compared to conventional crystalline cathodes of Li-ion batteries. While having a comparable overall performance to the crystalline materials, disordered cathodes have almost perfect dimensional stability opening a new direction in development of efficient electricity storage devices [11]. Another battery material is the amorphous Mg alloy as an electrode component for nickel-metal hydride (Ni-MH) rechargeable batteries [12, 13]. Ni-MH batteries were used for small portable electronic devices for almost three decades However, it is only recently, that it was realized that these materials may be used effectively in electric cars [13].

In the quest for alternative energy sources hydrogen emerged as a clean, eco-friendly candidate for energy applications. Unlike fossil fuels and oil, hydrogen combustion generates water as a by-product, so it doesn't contribute greenhouse gases to the environment. The key challenge here is the compact, and safe, storage of hydrogen. A significant improvement is achieved using amorphous metals as hydrogen absorbers. In particular, high-kinetics Mg-based alloys seem to be a promising candidate [12, 14]. Other associated energy and environmental applications include amorphous mesoporous

silica, silica-metal composite, ceramic and other amorphous materials for gas separation membranes [15-22].

Disordered pharmaceutical substances exhibit distinct physical and chemical properties compared to crystalline ones. This opens up an opportunity for improving the performance of the drugs by altering their microstructure to obtain a desired property, as well as by detecting and quantifying the amorphous state in order to avoid unwanted effects [23, 24]. For example, solubility, dissolution and delivery rate of a drug can be improved when in an amorphous state [25-29]. The study of amorphous-to-crystalline transitions of drug substances is also important for designing stable and safe pharmaceutical products [30, 31].

Nuclear waste management is the industry for which the development of new materials solutions seems to be the most challenging. Particularly, nuclear waste confinement and disposition has been an active research area for over 50 years with a focus on the glass-encapsulated waste forms [32, 33]. Predominantly amorphous borosilicates and phosphates are extensively used in the nuclear industry as a suitable glassy matrix for the immobilization of high-level nuclear wastes (HLWs), while cements containing crystalline and amorphous phases are used to encapsulate intermediate-level wastes (ILWs) [34]. In particular, disordered alkali borosilicate, aluminosilicate and aluminophosphate structures are employed on an industrial scale because they can incorporate rather a wide range of chemical elements/radioactive species and their vitreous waste forms are highly durable [34]. On the other hand, predominantly crystalline ceramics were proposed to target specific types of long-lived actinide nuclear waste, including zircon for weapons plutonium encapsulation [35]. Radiation damage

renders metamict zircon, which is a highly stable amorphous phase that does not leach plutonium. Geological samples of metamict zircons, dating over 2 billion years, can be rich in uranium and have been used for dating rock formations. These are among the oldest surviving rocks from the creation of the Earth, testifying to their stability. In recent years more attention has been paid to composite materials, especially to the glassy composite materials (GSMs) as hosts for problematic waste streams. GSMs are structurally intermediate to fully amorphous and perfectly crystalline phases, and are able to immobilize long-lived radionuclides in a durable crystalline phase which are in turn vitrified in a glassy matrix along with a wide variety of short-lived species [34, 36]. Other examples of applications of amorphous materials in the nuclear industry are various type of coatings which include but are not limited to glassy carbon coating for protection of graphite rods in molten salt Gen IV nuclear reactors, corrosion-resistant and neutron-absorbing amorphous metals [37]; and ceramic thermal spray coatings for drip shields, waste packages and other nuclear waste disposal and transportation applications [38].

Metallic glasses are one of the most actively studied materials ever since the formation of the first metallic glass was reported in 1960 [39]. The technology employed rapid cooling of liquid metals fast enough to form an amorphous solid structure. However, the high cooling rate necessary for "frustrating" the process of crystallization restricted the resulting products to thin films with limited applications [40, 41]. The cooling rate requirement became less stringent with the advent of certain alloys that provide additional "frustration" by inherent chemical disorder. Slower cooling opened the door for the development of broad classes of bulk metallic glasses (BMGs) [42] with

iron-based ones currently the focus of intense research because of the possibility of its cost-effective wide application [43, 44]. Combining some of the advantageous properties of conventional crystalline metals and the processability of conventional silicate glasses [45-47], BMGs are envisioned in numerous attractive industrial applications some of which have already been commercialized. For example, Zr-based BMGs with extraordinary glass forming ability (GFA) combine excellent static mechanical properties with relatively high impact fracture energy and low elastic energy absorption, which enabled their commercialization in golf clubs, tennis racquet frames and other sporting products requiring high strength properties [48]. Other current applications, some of which rely on the ability to achieve high quality edge and surface finish of BMGs [46, 49], include casing for cell phones and other small electronic devices; various medical devices such as surgical blades, fracture fixators, spinal implants; fine jewelry. Soft magnetic properties of Fe-based BMGs are utilized in distribution transformers, magnetic shielding plates, high wear resistance magnetic read heads etc. [50, 51]; the high corrosion resistance property is used in various anti-corrosion coatings. BMGs were also found useful in scientific applications such as high-geometrical-precision optical mirrors [51], not to mention the solar wind collector of the NASA's Genesis spacecraft [50]. Thermoplastic forming is another attractive property of BMGs, which, along with high strength, hardness, wear and corrosion resistance, offers an opportunity for MEMS fabrication [46] with small precision microstructures (gears etc.) [49], lightweight structural aircraft parts [51], spacecraft shielding [52]. Furthermore, the fine-scale molding ability is introduced as potential nano-molding technology [53]. Zr and Ti based BMGs, which combine large elastic strain limit and low Young's modulus complemented

by excellent fatigue and wear characteristics, are proposed for automobile valve springs as an approach to engine weight reduction, and consequent decrease in fuel consumption [51]. The self-sharpening effect of W-based BMGs was considered for military application as tank-armor penetrators in an attempt to replace the existing toxic depleted uranium ones, while W-based BMG armor and sub-munition is already in use in the defense industry [50, 51]. Metallic glass nanowire properties were found useful for catalysis in electrochemical devices [54]. Inspired by the superior strength, elasticity, wear and corrosion resistance of BMGs compared to conventional metallic materials used in the biomedical industry, a large number of novel BMG alloys were considered and tested for prosthesis and tooling applications [55-62]. The results of biocompatibility experiments, such as bio-corrosion studies [56], investigation of cytotoxicity [57] and in-vivo experiments [58], further motivate the development of biomedical technologies based on BMGs. Composite BMGs, reinforced by the addition of a second phase to the amorphous matrix, exhibit enhanced ductility – a property that was somewhat limiting BMGs' wide industrial applications [63]. Recent interest and development of such composites is likely to open new directions of industrial applications of viable metallic glasses.

The new century started with a rapid growth of fuel cell patent applications as a consequence of a strategic demand in sustainable energy. Great effort is currently put into development of low-cost, high efficiency and eco-friendly energy conversion devices. Fuel cell technology features, such as low-emission, relatively low operation temperature, low noise and simple, compact design, makes it attractive in a large variety of applications. Some of the applications that were already demonstrated, or are even in use

already, include various types of vehicles ranging from golf carts and utility vehicles to cars and buses, backup power generators, power for portable electronic devices, boats, submarines, airplanes and even satellites [64]. Although impressive, fuel cells are still facing further evolution aiming at zero-emission, higher conversion efficiency and lower cost for mass production, as well as smaller size and weight. One of the most important driving forces of this evolution is the research in novel materials for the components of fuel cells. Recent studies of amorphous materials for electrodes, electrolytes, and separators as well as alternative catalysts opened a new promising direction of fuel cell performance improvement. Surface activated amorphous metal alloy films were noted to be superior to conventional Pt particles in catalytic activity due to their ability to saturate an electrode homogeneously with desired catalytic elements for specific reactions [65]. Other properties like high strength, excellent corrosion resistance and formability are ideal for Proton Exchange Membrane Fuel Cells (PEMFC) bipolar plates [66-69], especially for design of the flow fields. Moreover, micro fuel cell design, that may be interesting for further development for compact, low-temperature applications, was reported based on BMGs' nano-scale thermoplastic forming [70]. Other amorphous-metal-based [71, 72], amorphous-metal-particle-based [73] and BMG-nanowire-based catalysts [54], electrolytes and amorphous non-metal materials for fuel cells were also reported [74-76].

Driven by dramatic price reductions in the solar cell industry during the last fifteen years, photovoltaics became the fastest growing source of power in the world by many parameters, particularly in rural electrification [77]. Grid parity was claimed recently for several locations and anticipated for many others around 2020 with fuel

parity being the next milestone of the solar cell power industry [77-80]. (One should be careful with the ”grid parity” claim, as different authors and solar energy companies have different interpretations of the term and tend to underestimate the grid parity cost of solar cells by disregarding certain associated expenses [81, 82].) Along with crystalline and polycrystalline solar cell technologies, the thin-film amorphous Si (hydrogenated a-Si or a-Si:H) technology, which relies on excellent tunable electronic properties of the Si enabled by alloying (raw tuning), and controlling hydrogen concentration (fine tuning), relative ease of large area preparation and doping, flexibility and stacking ability, as well as remarkably low silane (source of Si used in manufacturing) consumption and its efficient recycling, became the most developed thin-film technology for outdoor applications, and the most promising from a cost reduction standpoint [83-85]. Recent studies (considering inorganic materials) were mostly focused on its advancement, rather than development, of other amorphous material photovoltaics (with limited attention to C-based photovoltaics as a potentially low-cost solution [86-88]). Some research efforts towards higher cost-conversion efficiency of amorphous Si solar cells employ rare-earth ions’ upconversion property [89, 90]; window, electrode and “pin” layers’ design with suitable reflection, absorption and transparency properties for enhanced light trapping [91-98], and transparent conducting oxides (TCOs) for sandwiching the “pin” structure [99-102]; various silicon deposition and doping techniques enhancing the desired properties [103]; and “multijunctioning” for broadband photon harvesting and suppression of light-induced degradation (related to the so-called Staebler-Wronski effect) [104-106]. In particular, amorphous-crystalline Si heterojunction photovoltaics, which

are claimed to reach more than 20% conversion efficiency at industrial production levels, offer a promising future for solar power generation [104].

Another application field for amorphous TCOs (or transparent semiconducting oxides (TSOs)) is the flat panel display (FPD) industry where the extraordinary combination of high conductivity, high transparency and low temperature processing are the most desirable properties for its core - the thin film transistors (TFTs), especially for the cheap, large area, flexible FPDs. Amorphous Si TFTs are the most studied and it is the most mature technology in the industry [107, 108]. However, until recently, the indium tin oxide (ITO) with its superior conductivity and transparency characteristics was the industry standard for more advanced TFTs. Nevertheless, a large amount of research was dedicated to novel TCO materials to reduce or even eliminate the demand for the expensive and scarce indium [109, 110]. As a result of this extensive research in the last decade amorphous oxide semiconductors (AOS) are gaining strong ground in the TFT field [111]. So called AZO [112], IZOs [113, 114], ZTO [115], IGZOs [116], where A, I, Z, G, T and O stand for Al, In, Zn, Ga, Sn and O chemical elements respectively, are several examples of multicomponent AOS which feature good electronic and mechanical characteristics as well as low-temperature processing ability. In particular, IGZO, which combines high mobility and controllable carrier density with stability, mechanical durability and room-temperature processing, is getting much attention for application in organic light emitting diodes (OLEDs) FPDs and liquid crystal displays (LCDs) [116-118]. Although polycrystalline (as are most of the known TCOs) SnO, SnO_2, Cu_2O and $CuAlO_2$ oxides obtained by annealing of the sputtered amorphous phase are getting more

attention for their potential in the TFT based CMOS technology, amorphous tin oxide was reported in a number studies targeting p-type materials for CMOSs [119, 120].

A number of amorphous thin-film materials as well as amorphous quantum-effect nanostructures were reported for various components of light emitting diodes (LEDs) and OLEDs [121-126].

Other examples of amorphous materials' applications are the following: silica glass for fiber optics, windows, bottles etc., as well as for food industry applications and production of the most common type of cement - the Portland cement; high chemical stability and high dielectric constant amorphous thin-film gate oxides, alloy silicates and aluminates (Al_2O_3, ZrO_2, HfO_2, $ZrSiO_4$, $HfSiO_4$ etc.) to replace the conventional silicon dioxide in transistors [127-131].

1.2. Structural Characterization Techniques.

Structure strongly determines the properties of materials. Therefore, the effective structural characterization of disordered materials is an extremely important issue. Not only does it facilitate and guide the synthesis of new materials with properties superior to the currently used ones within a given application field, but it also makes possible the prediction of new properties that may be applicable in other fields. With growing number of industrial applications, structural characterization of amorphous materials becomes one of the biggest contemporary challenges in the materials science.

Unlike polycrystalline and crystalline solids, amorphous solids lack long range order (LRO), i.e. a correlated structural coordination of constituent atoms at large distances from a given atom. In fact they exhibit short- and medium-range order (SRO and MRO), that is, there is no structural correlation beyond a certain distance that is

loosely defined as ~0.5 nm for SRO and about 2 nm for MRO. Chemical bonding of atoms in disordered solids is nearly unchanged from crystals. Small, random variations in the angles between the bonds eliminate regular lattice structure. In other words, SRO describes the structure in the nearest neighbor coordination shell which represents a well-defined polyhedron (tetrahedron in Si, for instance), whereas the character of the connections between the polyhedra defines the MRO. SRO is described by 2-body (radial distribution function, RDF, or pair correlation function) and 3-body correlation functions, whereas MRO is best described by 4-body (pair-pair) and higher order ones.

This division into correlation distances, which classify the order in solids into SRO, MRO and LRO, is dictated mainly by structural characterization techniques. Indeed, different techniques exhibit different sensitivity to correlations at various length scales.

In single crystals, where each atom position is determined by translations of the unit cell with some basis of atomic species, all atom positions can be determined by diffraction (X-ray, neutron or electron) and high resolution transmission electron microscopy (HRTEM). Chemical characterization is available with energy-filtered HRTEM imaging enabled by either an in-column filter (Ω–filter) or post-column magnetic prism spectrometer (Gatan imaging filter). High-resolution elemental mapping is also carried out routinely now in aberration-corrected STEM instruments equipped with electron energy loss spectrometers (EELSs) and/or energy dispersive X-ray spectrometers (EDXSs) [132]. In addition more or less reliable atom by atom chemical mapping by high angle annular dark-field (HAADF) imaging in aberration corrected STEM instruments has been demonstrated [133].

Early attempts to detect MRO relied on high-resolution TEM imaging, which was expected to resolve nano-crystallites within the amorphous matrix. However, it was realized that fringy patches in TEM images from amorphous samples cannot be interpreted as ordered regions in view of the fact that both artificial randomization of phase in those images and application of a bandpass filter, produce qualitatively similar images [134, 135]. Rarely, signal from ordered regions may be strong enough to be reliably resolved in very thin samples and can be detected with subsequent statistical processing of the images. Cross-correlating square templates of 1 nm^2 in size from experimental high-resolution TEM images of Ge^+-implanted amorphous Si with an image from expected orientation of Si grains was found effective in detecting Si nanoclusters [136]. About 1.5 nm grains were directly observed in amorphous carbon by comparison of the original bright field micrograph with its artificially phase-randomized reconstruction, which showed qualitative changes and therefore confirmed the statistically significance of the observed fringes [134]. This statistical significance was proposed to be quantified by the comparison of the Shannon entropy of HRTEM images to that of a random sample in [137]. An excellent review of the difficulties associated with high-resolution electron microscopy of amorphous materials is given in [138]. It was noted there that the irregularity of the fringes observed in very thin films, even if they pass the test of statistical significance, suggests that they can't be interpreted as a crystalline structure.

On the other end, complementary techniques to probe SRO, with limited sensitivity to MRO for some of them, include: elastic X-ray scattering, core-electron-ionization-based techniques, such as X-ray absorption near edge structure (XANES),

extended X-ray absorption fine structure (EXAFS), energy loss near edge structure (ELNES) and extended energy loss fine structure (EXELFS); magic angle spinning nuclear magnetic resonance (MAS NMR); phonon-scattering techniques, such as Raman and infrared (IR) spectroscopies; energy-filtered selected area diffraction (SADP). Each of these techniques alone gives very scarce definitive structural and chemical information due to inherent limitations, elaborate data processing and interpretation. Therefore most advanced studies tend to analyze the eclectic set of data obtained by a combination of these techniques in order to infer as much structural information as possible. The following is a brief overview of the techniques mentioned above.

XANES and EXAFS are closely related techniques of X-ray absorption in the sample which in most cases is implemented using monochromated, very intense synchrotron radiation. Much less expensive and more accessible electron versions, ELNES and EXELFS employ an electron microscope equipped with an EELS spectrometer. The key physical process in all cases is the ejection of a core electron by the incident beam. The latter is then scattered by the first few nearest neighbors, either in a single event or in plural events resulting in intensity modulations in the absorption (X-ray beam) or EELS spectrum near the ionization edge onset. The single scattering nature of the fine extended structure renders it useful for determining only pair correlations, i.e. RDFs. Well established experimental data processing procedures, including background subtraction, isolation of the modulations, and the Fourier transform that yields the RDF are described in detail in [139, 140]. On the other hand the plural scattering, which gives the near edge structure of the spectrum, offers the opportunity to extract nearest neighbor coordination and bonding information. In practice, however, it is only possible through

matching of the near edge data to the calculated spectrum from a model as interpretation is complicated due to the absence of simple analytical description (as opposed to extended fine structure) [141, 142]. For this reason most of the studies employ the extended fine structure, especially EXAFS with its intense synchrotron source. SRO in BMGs was studied by both EXAFS and EXELFS in [143], in which the nearest neighbor configuration was determined for all constituents multicomponent BMGs. It is interesting to note that extended fine structure is argued to be sensitive also to MRO, i.e. to higher order correlations. The RDF peak at about 0.5 nm is asserted to be a signature of MRO in a-Si:H by some authors [144] and was shown to depend on the thermal history of the sample [145]. Others suggested that it may be an artifact of the complicated data processing.

Energy filtered SADPs offer another method capable of obtaining the RDF in the TEM. It is implemented by scanning the SADP across the entrance aperture of the EELS spectrometer to filter out inelastically scattered electrons. The RDF can be extracted from the resulting line profile of the energy filtered diffraction pattern [146].

X-ray scattering with its simple experimental setup (unless a synchrotron source is used) is perhaps employed most frequently for characterization of disordered materials and is claimed to be sensitive to MRO. Indeed, the pre-peak in the wide angle X-ray scattering (WAXS) intensity is argued to be an indication of MRO with its half-width being a rough estimation of the correlation length and position being a measure of its periodicity [147-150]. The correlation length in inhomogeneous materials is also obtained by SAXS (or its neutron beam counterpart, SANS) by its intensity fitting to the Guinier law [151, 152]. It is argued in that SAXS can detect the material's density fluctuations at

the nanometer scale, and has been used to assess the degree of hyperuniformity in amorphous Si [153].

MAS NMR is a powerful technique for exploring structural order in amorphous materials, both at short- and medium-range, as it is capable of extracting information about both the building blocks of the structure as well as the connectivity among them. It is based on the sensitivity of radio frequency electromagnetic radiation pulse absorption by NMR-active nuclei on the local electronic environment which manifests itself in the so-called chemical shifts of the NMR frequency. For instance, a large amount of MAS NMR experiments report on bond angle distributions (BADs) in amorphous silica [154]: average values of the Si-O-Si angle are derived from its assumed correlation to the NMR chemical shift [155, 156]. With regards to MRO, BAD can give information about ring speciation as it constrains the permissible ring sizes. MAS NMR may also resolve signals from distinct structural tetrahedral groups with different degree of depolymerization providing insight into the polymerization speciation of some binary glasses [157]. More sophisticated MAS NMR techniques exploit through-bond (*J*-coupling) and trough-space (dipolar) interactions in order to explore pairwise connectivity between tetrahedral groups. Signals from various chemically/structurally distinct species are enhanced by employing complicated pulse sequences. The so-called cross polarization MAS (CPMAS) and other heteronuclear techniques, are carried out for probing connectivity among distinct nuclei species [158].

Probes of vibrational properties, such as Raman, IR and neutron spectroscopies, are also used extensively to infer the structural order in materials. Their sensitivity to changes in vibrational band structure caused by modification of materials microstructure

is the key feature. In particular, it is argued in [159] that the r.m.s bond distortion angle in amorphous silicon (tetrahedral bonding) depends linearly on the width of the TO phonon line. MRO is classified qualitatively by the ratio of the TO and TA line intensities in a number of Raman spectroscopy studies [160-162]. Another study demonstrated correlation between the X-ray scattering pre-peak mentioned above, which is argued to be an indication of MRO in glasses, with the so-called Boson peak (low frequency vibrational feature absent in crystals) in Raman spectra [163-165]. The Boson peak position in the spectrum is actually considered a measure of the MRO size in the same study, and in [166]. The frequencies of TA and TO phonons are also considered order parameters for they become closer as the local order decreases [167].

As the reader can see, despite the complexity of the experimental data analysis, the techniques above can provide rather reliable structural information at the short range and some glimpses of MRO. Today, most structural studies of disordered materials trace the output signal behavior on modification of the sample's characteristics. For example, a large number of experiments concentrate on studies of amorphous silicon and metallic glasses that examine signal dependence on temperature, preparation procedures, hydrogen content, network modifier's content etc. Other studies aim to retrieve the structure through matching of the particular experimental signal to the computed values for a model. The problem with the latter is the variety of structures giving indistinguishable signals; hence the persistent controversy over the structural origin of detected MRO in various materials [147]. Unfortunately, all of the techniques above have limited sensitivity to 4-body correlations. Diffraction techniques are inherently attuned to 2-body correlations, they mainly access the RDF, which appears to be featureless beyond

about 1 nm at best in amorphous silicon and carbon. The weak coherent diffraction signal from MRO gets lost in the background signal. Successful imaging, on the other hand, is only limited to the case of very thin samples, and therefore is impractical. This is the reason why MRO is notoriously hard to probe and characterize in amorphous solids. The issue is addressed by a relatively new technique developed by Treacy and Gibson called Fluctuation Electron Microscopy (FEM).

1.3. Overview of Fluctuation Electron Microscopy

FEM is a hybrid diffraction-imaging technique that examines the scattering statistics from small volumes of thin amorphous materials to detect the presence of MRO [168, 169, 135, 170, 171]. It is the spatial fluctuation of coherent scattering that the word "Fluctuation" refers to. By now it has been thoroughly demonstrated, by modeling and simulations, that FEM is extraordinarily sensitive to MRO, much more than high-resolution diffraction and high-resolution imaging. It should be mentioned that there are some examples of sensitivity of direct electron microscopy imaging or diffraction techniques, which are rare examples of strong signal to background conditions. These methods rely on the availability of thin samples with thicknesses not exceeding several characteristic crystallite sizes to be detected, as well as appropriate image or diffraction pattern processing techniques [134, 136, 172]. Unlike these methods, the statistical approach of FEM, which will be described later on in this chapter, provides a general means of disentangling the MRO signal from the background, even if those strict and rarely achievable sample thickness requirements are not met. Experiments have confirmed this sensitivity of FEM to MRO [168, 172-175, 170, 176], which enabled a number of important studies that are summarized below.

Among other applications, FEM has been used to study amorphous semiconductor materials. Given the conjecture that its structure is a continuous random network (CRN), it was found that the CRN is more stable thermodynamically evidenced by a diminished MRO in annealed Ge compared to the as-deposited material [170]. The Staebler-Wronski degradation effect of solar cells based on amorphous hydrogenated silicon was concluded to be a consequence of the material's structural change induced by light absorption. The study of these structure changes by FEM suggested that structures close to the CRN should be less vulnerable to the degradation effect [173]. Absence of an abrupt phase change from polycrystalline to amorphous Si with deposition temperature has been concluded in an FEM study of silicon deposition. It was based on the observation of a continuous change of the FEM signal which can be explained by paracrystalline grain size growth and density changes [176]. FEM was applied to infer structure details in metallic [177-180] and oxide glasses [178, 181] and amorphous carbons [182-185]. In particular, it was found that MRO decreases with increasing annealing temperature in amorphous $Al_{92}Sm_8$ alloys [177]. An interesting observation was reported in [183] – contrary to previously observed diminished MRO in amorphous silicon and germanium, increased MRO in tetrahedraly-coordinated amorphous carbon was detected with annealing to 600 °C. However, further annealing to 1000 °C was observed to decrease tetrahedrally-coordinated building blocks of MRO with increasing graphitic ones. Variation of the extent of ordering with different sample growth conditions and TEM preparation techniques were also reported [186, 180]. A number of studies attempted to relate the extent of MRO to the mechanical properties of the sample [180, 185, 181].

FEM has been found useful in resolving a long-standing debate about paracrystalline versus pure CRN (or other random tetrahedral network) structure of silicon. The presence of paracrystallites, which are highly strained crystalline regions with length scale of about 0.5-3 nm, has been confirmed in amorphous silicon by correlograph analysis of electron diffraction patterns [172] and in germanium ion implanted amorphous silicon by autocorrelation function analysis of TEM images [136]. An experimentally constrained reverse Monte Carlo simulation study which used experimental FEM data as inputs has confirmed paracrystallites as a minority phase in CRN [187]. Parcrystallites were also found in as-deposited amorphous Si and Ge and which were observed to transform towards a CRN-like structure after annealing [175]. On the other hand RDFs obtained by x-ray and neutron scattering suggest there is no evidence of paracrystallites. Another study suggested voids in the Si CRN instead of paracrystallites [188]. It should be noted that the insensitivity of RDFs to MRO, especially when MRO is a minority phase is most probably the reason for the x-ray and neutron scattering results mentioned above.

There are two key contributing factors to the sensitivity of FEM to MRO. First, FEM examines the *variance* of the scattering statistics, which is proportional to the second moment of the intensity distribution. Essentially, FEM examines the speckliness of the diffraction data, its *fluctuations* across the sample. These fluctuations are visualized when the variance is plotted as a function of the scattering vector. In practice we rather plot the normalized variance,

$$V(\boldsymbol{k}) = \frac{\left\langle I^2(\boldsymbol{k},\boldsymbol{r})\right\rangle_{\boldsymbol{r}}}{\left\langle I(\boldsymbol{k},\boldsymbol{r})\right\rangle_{\boldsymbol{r}}^2} - 1, \tag{1.1}$$

where averaging is implied over the spatial coordinates of the sampled area, and $\boldsymbol{k}$ is the scattering vector magnitude. Kinematical scattering theory for the case of diffraction-limited imaging and a specimen consisting of identical atoms gives the following expression for the mean intensity and the mean of the intensity squared [168]

$$\left\langle I(\boldsymbol{k},\boldsymbol{r})\right\rangle_{\boldsymbol{r}} = \frac{\lambda^2 f^2(k)}{a}\sum_{j,l} A_{jl}F_{jl} \text{ , and} \tag{1.2}$$

$$\left\langle I^2(\boldsymbol{k},\boldsymbol{r})\right\rangle_{\boldsymbol{r}} = \frac{\lambda^2 f^2(k)}{a}\sum_{j,l} A_{jn}A_{nl}A_{mn}F_{jl}F_{mn} \text{ ,} \tag{1.3}$$

where the summation is over all atoms with position vectors $\boldsymbol{r}_j$, λ is the electron wavelength, $f(k)$ is the atomic scattering factor, and a is the sampling area. Terms $A(r_{jl}) = 2J_1(K_{ap}r_{jl})/K_{ap}r_{jl}$, which are Airy disk amplitude functions, with J_1 being the first-order Bessel function of the first kind, are controlled by the point spread function of the imaging optics with objective aperture radius K_{ap}. Terms $F_{jl} = \exp(-i\boldsymbol{k}\boldsymbol{r}_{\boldsymbol{jl}})$, with $\boldsymbol{r}_{\boldsymbol{jl}} = \boldsymbol{r}_{\boldsymbol{l}} - \boldsymbol{r}_{\boldsymbol{j}}$, are the phase shifts between atoms j and l, and therefore characterize coherence of the interference between them; or, in other words, the coherence volume around each atom. They are controlled by the illumination optics. It is readily seen that the mean of the square intensity contains 4-body terms unlike the mean intensity, which depends only on 2-body terms. Inserting (1.2) and (1.3) in (1.1) gives

$$V = N_0 \frac{\sum_{j,l,m,n} A_{jn}A_{nl}A_{mn}F_{jl}F_{mn}}{\sum_{p,q,r,s} A_{pq}A_{rs}F_{pq}F_{rs}} - 1, \tag{1.4}$$

where $N_0 = a\pi K_{ap}^2$. The sensitivity to MRO stems from the fact that the variance examines 4-body correlations, whereas diffraction alone examines the first moment of

intensity, i.e. pair-correlations. The four-body terms are much more sensitive to medium-range correlations.

The second key factor, which in this era of aberration-corrected microscopy may come as a surprise, is that it is a *low-resolution technique*. The sensitivity of FEM to MRO is maximized when the resolution is comparable to the length scale of the MRO. The so-called variable resolution FEM (VRFEM) exploits this fact to infer the size of structural ordering.

FEM data is usually obtained in one of two modes: tilted dark-field (TDF) and scanning transmission modes of FEM. TDF FEM data is obtained by collecting a tilt-series of low-resolution tilted dark-field (TDF) images in a transmission electron microscope (TEM). A narrow range of scattering vectors is selected by the finite width of the objective aperture (Fig. 1). Variance plots are then obtained by plotting the normalized image intensity variance, calculated using (1), against the tilt vector magnitude. It should be mentioned that the earliest version of FEM, termed *Variable Coherence Microscopy*, was done in the hollow cone illumination dark-field TEM mode which allowed variation of the coherence volume through variation of the cone width [189, 168]. As compared to TDF FEM, the hollow cone mode enables tuning of the coherence volume into a narrow area along the optical axis (smaller than several atoms aligned in the column). This in turn enhances the FEM signal from small ordered regions fitting within this coherence volume by suppressing contributions from random alignments of atoms outside the coherence volume. The latter usually renders experimental variance values that are about two orders of magnitude less than that in case of TDF FEM.

In the alternative scanning transmission electron microscope (STEM) mode, a set of micro-diffraction patterns are collected at each probe position while the latter is scanned over the sample area (Fig. 2). It is termed scanning transmission fluctuation electron microscopy (STFEM). Variance plots are then obtained by applying the procedure described in Fig. 3.

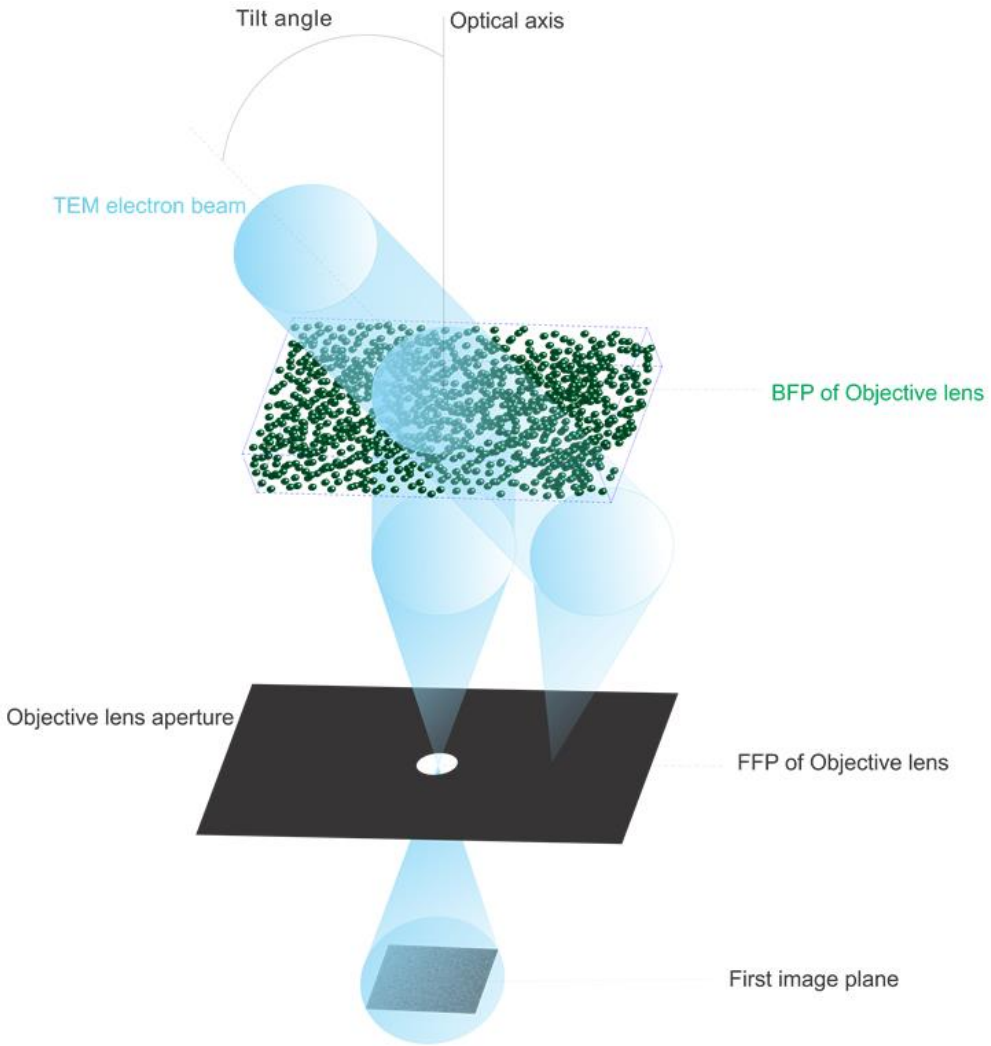

Fig. 1. Schematic of the FEM experiment in the tilted dark-field TEM mode. The specimen is illuminated by a tilted, plane-wave electron beam. The objective aperture is aligned with the optical axis of the microscope in order to select only diffracted beams and block the unscattered beam. The scattered electrons entering the objective aperture contribute to the tilted dark-field image formed further down the column. The tilt angle is varied and images are collected at each tilt angle.

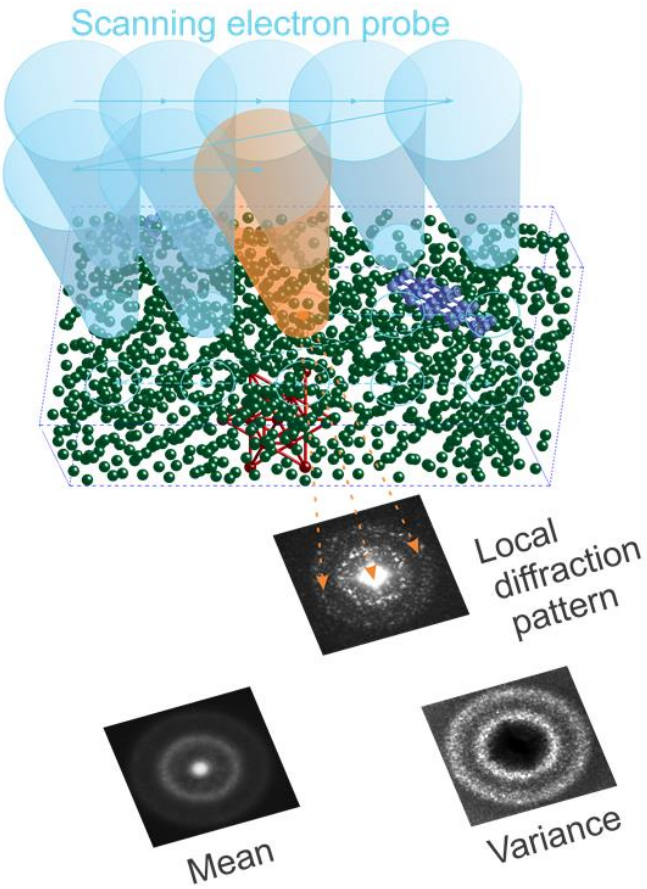

Fig. 2. Schematic of the FEM experiment in the STEM mode (STFEM). The specimen is illuminated by a small-convergence, focused electron probe that is scanned over a grid of positions on the sample. Diffraction patterns are collected at each position of the electron probe.

Both modes collect a 4-dimensional dataset $I(x, y, k_x, k_y)$ which should not be surprising in the light of the reciprocity principle. However, experimentally, the first has higher sampling density in the real space, whereas, the second has a higher reciprocal space sampling density.

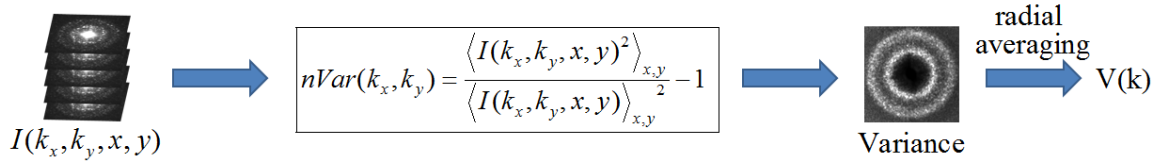

Fig. 3. Schematic of the experimental STFEM data processing. The stack of diffraction patterns, which in its entirety is nothing less than $I(x, y, k_x, k_y)$ data, is used to calculate the normalized variance. The resulting variance map is radially averaged to give a plot of normalized variance versus the scattering vector amplitude $V(k)$.

Although FEM is successful as a qualitative technique – it can disclose unambiguously and sensitively the signature of MRO in a sample – it is not yet truly quantitative. There are two main reasons for this state of affairs. We do not know how to invert analytically four-body diffraction data. There has been significant progress in bypassing this issue by use of the experimentally constrained reverse Monte Carlo method [190, 191, 179, 188]. This method shows great promise, but it has revealed a huge discrepancy between simulated variance and experimental variance: the experimental variance is usually a factor of 10–100 less than the calculated values and it is suppressed much more severely at scattering vector values exceeding 10 nm^{-1}.

This discrepancy between experimental variance and computed variance was loosely attributed to illumination incoherence in early FEM studies. A phenomenological model of such incoherence was developed [192] and adopted in [193], where it was assumed that if there were *m* incoherent sources, and a uniform thickness sample, then the intensity probability distribution in a tilted dark-field image would follow the Gamma distribution

$$P(I) = \frac{m^m}{(m-1)!}\frac{I^{m-1}}{\langle I \rangle^m}\exp\left(-m\frac{I}{\langle I \rangle}\right). \qquad (1.5)$$

In the next chapter of the present work series of TDF TEM images of amorphous carbon are analyzed in order to explore how well the model of incoherence fits to the amorphous carbon FEM data. The results of this analysis together with the reality of a coherent field emission gun electron source used for acquiring the TDF FEM data, pointed me towards the idea that it may be electron-beam-sample interactions that generate the impression of illumination incoherence. That is, decoherence is the culprit,

instead of illumination incoherence. Consequently, as a next step, I present the results of STFEM experiments on amorphous silicon and carbon samples targeting the FEM variance dependence on electron-beam-specific (Chapter 4), and sample-specific (Chapter 5), parameters. In particular, the experimental variance is compared with the theoretical kinematical variance computed for a number of heuristic decoherence models in Chapter 4. The next chapter presents the results of experiments aiming to confirm the validity of the expression proposed in [194] by Treacy for variance dependence on sample thickness. As a sidetrack of one of these experiments, Chapter 5 also describes an interferometric diffraction experiment on bilayer amorphous carbon and silicon films confirming the role of decoherence as the primary cause of variance suppression. Chapter 6 contains the results of an electron microscopy characterization of ultra nano-crystalline diamond (UNCD) films that was conducted during the course of these investigations.

.

CHAPTER 2

EXPERIMENTAL PROCEDURES AND DATA PROCESSING

2.1. Experimental

The TDF FEM experiment was carried out by G. Zhao using the ASU JEOL2010F TEM operated at 200kV, equipped with a Gatan MSC 794 CCD camera which has acceptable low-noise characteristics. Tilted dark-field TEM images with about 1 nm resolution (10 micron objective aperture) were acquired in the tilt range of 2 to 10 nm^{-1} using a Digital Micrograph^{TM} script that controlled the X and Y beam deflectors.

The STFEM studies were carried out using the ASU JEOL ARM200F instrument equipped with a Schottky field-emission gun operated at both 80 and 200 kV. Formation of nanometer-sized probes turned out to be problematic in the STEM mode, so the NBD-S (nano beam diffraction–small) condenser configuration mode was employed. Probe positioning and data acquisition was enabled by the Digital Micrograph^{TM} script mentioned above. The script needed to be modified to conform to the updated commands of a newer ARM200F instrument and the newer CCD camera. Diffraction patterns were collected on a Gatan 833 Orius SC200D CCD retractable camera with low-noise characteristics. The new 833 damage-resistant scintillator allowed acquisition of diffraction patterns with a saturated central area of the detector, necessary for acceptable signal levels far from diffraction central spot; there was no beam-blanking capability. The JEOL ARM200F has preset spot sizes ranging nominally from 0.5 nm to 2.4 nm in NBD-S mode with aberration the corrector off. These are nominal values and correspond to a range of excitations of the first condenser lens (CL1) – the actual probe sizes also depend on the actual condenser aperture, and so are different from nominal sizes. For example,

the 2.4 nm spot ensured a low convergence (~ 2 mrad) diffraction limited electron probe of about 1.5 nm resolution when using a 20-μm condenser lens (CL) aperture at 200 kV, and about 1.3 nm with 30-μm aperture at 80 kV. The 0.5 nm spot provided about 2.4 nm resolution probe when using a 10-μm aperture at 200 keV. Note that CL1 is the source demagnification lens in the employed condenser system configuration. The source is demagnified the most in the "spot 0.5 nm" setting where the CL1 is highly excited, therefore providing the highest spatial coherence level of illumination. The opposite is true for the "spot 2.4 nm". The following table provides rough estimates of probe currents and fluence rates for each probe described above. These values were obtained by fitting the probe image-intensity profiles to Gaussian functions and integrating analytically the resulting fits.

Table1

STFEM probe characteristics

<table>
<tr><th></th><th>Energy (keV)</th><th>JEOL spot</th><th>CL aperture (μm)</th><th>Probe size* (nm)</th><th>Probe current (pA)</th><th>Probe Flux (el./(nm^2×sec))</th></tr>
<tr><td>Probe 1</td><td rowspan="3">200</td><td>spot 0.5 nm (high coherence)</td><td rowspan="2">10</td><td rowspan="2">2.4</td><td>3</td><td>10^6</td></tr>
<tr><td>Probe 2</td><td rowspan="4">spot 2.4 nm (low coherence)</td><td>65</td><td>0.23×10^8</td></tr>
<tr><td>Probe 3</td><td rowspan="2">20</td><td>1.5</td><td>275</td><td>2.44×10^8</td></tr>
<tr><td>Probe 4</td><td rowspan="2">80</td><td>2.0</td><td>425**</td><td>0.84×10^9 **</td></tr>
<tr><td>Probe 5</td><td>30</td><td>1.3</td><td>955***</td><td>1.12×10^9 ***</td></tr>
<tr><td colspan="7">* The probe size, defined here as diffraction-limited resolution, was obtained from crystalline silicon diffraction pattern measurements.
** The value is not measured but rather estimated by calculation using the Probe 5 current and the ratio of physical aperture areas.
*** The value is not measured but rather estimated by calculation using the Probe 3 current value and the fact that diffraction intensity profiles for probes 3 and 5 were approximately matched by 3.7 sec and 0.8 sec exposures, respectively.</td></tr>
</table>

Most data were collected from a 10×10 grid of points separated by about 7 nm on the sample resulting in a stack of 100 diffraction patterns. Exposure times were adjusted

for each condenser lens configuration and sample (ranging from 0.01 sec to 3.7 sec) in order to minimize the shot noise contribution to the FEM data at higher diffraction vector, *k*. The camera length was adjusted to collect data in the range -14 $nm^{-1} < k < 14\ nm^{-1}$.

The TEM imaging was carried out using the JEOL2010F TEM at 200kV. The aberration corrected annular dark field (ADF) and bright field (BF) STEM imaging has been carried out using the JEOL ARM200F at 200kV, with the CEOS CESCOR hexapole aberration corrector activated. Some EELS spectroscopy results have been obtained using the ASU Nion UltraSTEM^{TM} 100 equipped with a cold field emission gun operated at 60 kV, with a beam monochromator and the Gatan Enfina EELS. The probe forming optics were configured to deliver a probe convergence semi-angle of 30 mrad, while the EELS collection semi-angle was calibrated at 45 mrad (5 mm entrance aperture).

Relative thickness measurements were carried out by obtaining low-dispersion EELS spectra or dark-field images from the areas under consideration by means of the Gatan Enfinium EELS or ADF1 detector of JEOL ARM200F operated at 200 keV, respectively. Camera length (8 cm) was adjusted to set the collection range of the ADF detector to ~90-370 mrad range. The detector has been calibrated at a chosen gain and black-level by using a sample with five quantized thicknesses (see the sample description later). The "quantum" step in thickness was measured by sideways view TEM image of a curled region of the sample. ADF intensities (minus hole counts) from the five known thicknesses were fitted to a simple approximation of the high-angle ADF (HAADF) intensity thickness dependence [189]

$$I(t) = (at + bt^2 + ct^3)\exp(-dt), \tag{2.1}$$

and parameters $a=1.312\times10^{-2}$, $b=1.712\times10^{-4}$, $c=6.516\times10^{-10}$ and $d=2.397\times10^{-3}$ were obtained for future thickness measurements. Fig. 4 shows the fit. The data points are in an essentially linear, validating single scattering approximation, far below the characteristic sample thickness beyond which the intensity scattered into the annulus starts decaying.

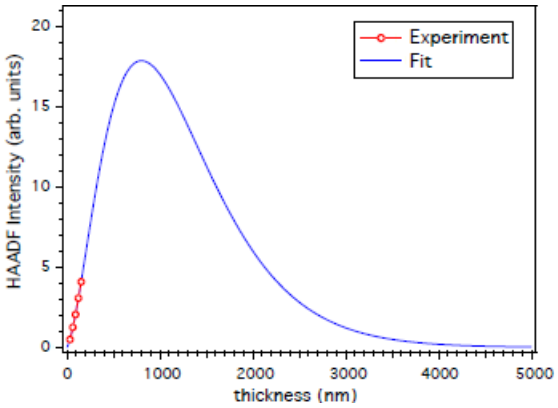

Fig. 4. HAADF intensity from five quantized-thickness areas with a 30 nm quantum step of an amorphous carbon film, fitted to the curve giving a simple approximation of HAADF intensity thickness dependence. The fit shows that the data points are in the linear dependence region.

Dark-field TEM imaging was carried out using the JEOL ARM200F in the TEM-L mode operated at 200kV. First selected area (SA) diffraction was obtained using a 20 mm SA aperture, then a 5 mm high-contrast (HC) aperture was used to select desired reflections. This procedure required refocusing of the diffraction pattern using the last condenser lens because it would become defocused after the focusing step on the HC aperture by the first intermediate lens (IL1 or diff. focus).

2.2. Samples' Descriptions and Preparation Procedures

Approximately 30 nm thick amorphous carbon film was sputtered onto mica from graphitized rods of carbon in a standard sputterer. The film was floated off the mica on the surface of distilled water and picked up on a 300-mesh 3 mm copper grid. This sample was used for TDF STEM experiments.

STFEM experiments were carried out using amorphous carbon and silicon samples, which form predominantly tetrahedral networks, as well as with ultra-nanocrystalline diamond (UNCD) carbon.

(1) A commercial, `ultra-stable,' amorphous carbon film made by GloEMT^{TM} Co, supported on a 200-mesh 3-mm Cu grid. Its thickness, measured directly from a curled-up region, was about 30 nm (see Fig. 5).

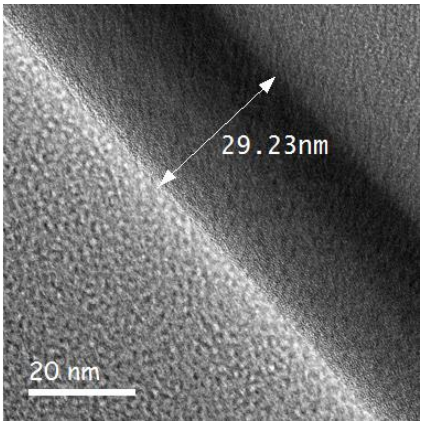

Fig. 5. BF TEM image of a curled-up region of a-C film. The curled-up fragment is lying on the a-C film support film.

(2) A freestanding amorphous silicon sample, ~20-nm thick, was prepared by sputtering Si at 200°C onto an amorphous carbon film. The sample was argon plasma-cleaned to remove the carbon support film before observation. This sample was kindly provided by B. S. Lee of the University of Illinois, Urbana-Champaign.

The amorphous silicon film (1) was used to obtain a bilayer sample. The commercial amorphous carbon support film (2) was utilized to obtain multiple-thickness samples, referred here as the *multi-step* carbon and the *multi-layer* carbon films.

The multi-step sample was fabricated by Ga ion milling of approximately 1 μm by 1 μm adjacent square areas on the 30-nm thick a-C sample during multiple time intervals using the FEI Nova 200 NanoLab^{TM} FIB instrument.

The multi-layer carbon film was prepared in the same instrument using the Omniprobe^{TM} Pt needle (the ion column was not put to use). The support film within one of the copper grid cells was torn by the Pt needle, after which it was pushed from the cut end in order to roll it up. The needle was then inserted into the rolled-up cone or cylinder and pulled to cut the cone loose from the film. The separated cone was then transferred to a fresh area and pushed against its surface, so the cone clung to the film and the needle was retracted. Finally, the needle was pushed against the rolled-up piece to crack it, and then stroked along the crack to obtain a flat multi-layered film. The procedure is outlined in Fig. 6, which shows snapshots from a recorded movie of the preparation process. The resulting multi-layered film had quantized-thickness structure, which images will be presented later.

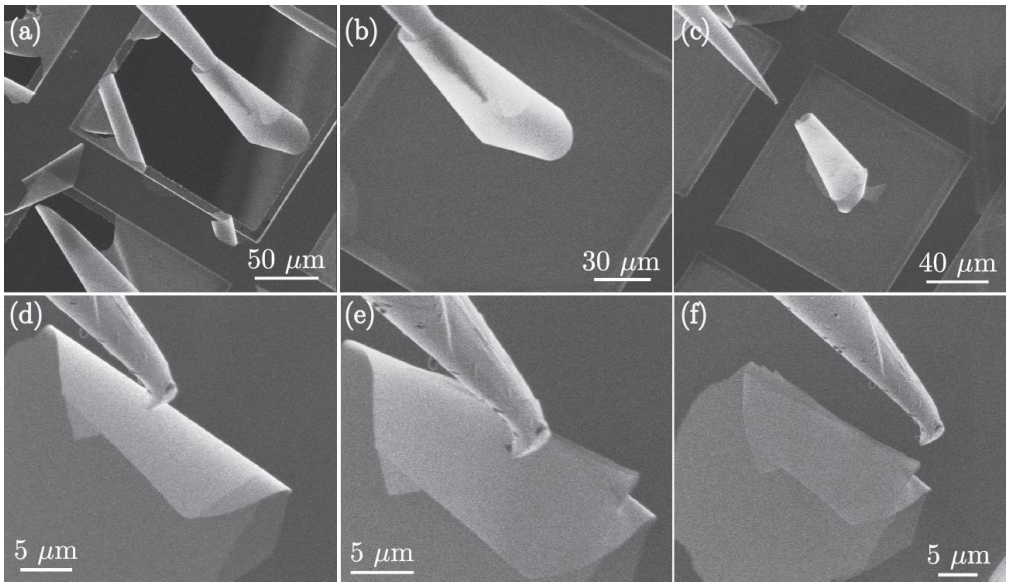

Fig. 6. Secondary-electron SEM images showing the multi-layer carbon films preparation process. (a) – The existing 30-nm carbon support film is torn from the Cu grid by the Omniprobe^{TM} Pt needle and rolled into a conical or cylindrical shape. (b) – The assembly is moved to a clean area of carbon film by inserting and moving the needle, and dropped on a fresh, unaffected support film area. (c) – The Omniprobe^{TM} needle is withdrawn. (d) – The needle applies pressure to the exterior curved carbon walls. (e) – The rolled film starts to crack. (f) – The needle is "stroked" along the cracks to complete the flattening process to produce a layered structure.

The amorphous silicon film appeared to be much more fragile than the a-C sample, so it was difficult to produce a multi-layered structure. The bilayer structure was eventually obtained by breaking the film in one region, attaching the resulting fragment to the Omniprobe needle, caring it to another region and finally attaching one end of the fragment to the intact region of the film. Fig. 7 shows an SEM image of the created hollow wedge-shaped bilayer structure.

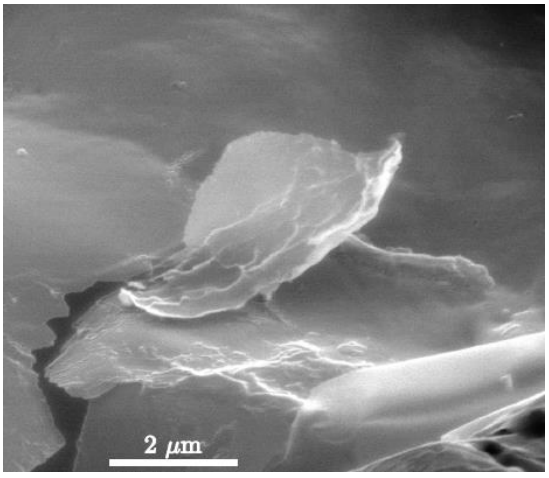

Fig. 7. SEM image of a fragment of a-Si attached, presumably through van der Waals force, to the film from one end and loose from the other, providing a bilayer structure with variety of gap values.

The UNCD film was synthesized by F. Koeck (at ASU) by plasma-assisted chemical vapor deposition onto a 100-oriented single-crystal Si substrate or a polycrystalline Mo substrate. The procedures consist of; (i) seeding by ultrasonication of the substrate in a nano-diamond slurry and rinsing; (ii) vapor deposition of the nitrogen incorporated UNCD layer in microwave plasma while maintaining the temperature of the substrate; (iii) changing the vapor and plasma parameters for N-doped diamond layer deposition and exposing the surface to the hydrogen plasma to obtain the NEA characteristic of the emitter. A number of films with thicknesses ranging from about 200 to 500 nm were grown.

The cross section UNCD TEM samples have been prepared by the focused ion beam lift-out technique, using an FEI Nova 200 NanoLab^{TM} instrument with an Omniprobe^{TM} tip. The final Ga ion-beam thinning was done with 30 kV (accelerating voltage) and 10 pA (beam current) ion column settings, and a ~1-degree scan rotation relative to the lifted-out sample, resulting in a wedge-shaped TEM sample with a ~ 2-degree nominal wedge angle. Initially, conventional polishing, dimpling and Ar ion milling was tried, however, difficulties were encountered. Namely, it turned out that sawing the Mo substrates leaves burrs that extend beyond the edge of the cut piece, so that the surface is not flat – leaving a bump along the cut edge. These bumps preclude gluing of the two UNCD surfaces during cross sectional sample preparation. There's no such issue with Si substrates but the well-known bridging effect because of the differential thinning (of hard UNCD and soft Si in this case) appeared to be impossible to eliminate completely either by shifting the beam a bit off from the interface or by decreasing/increasing the grazing angle of PIPS ion milling instrument. Only occasionally were very small, thin areas attained. Although, these areas never contained both the bottom and top regions of the film (since the films were about 200-600 nm), so the preference was given to FIB sample preparation. TEM imaging of samples that were prepared by the conventional method is omitted from the scope of this work.

2.3. Data Processing and Modeling

MATLAB^{TM} scripts were developed for STFEM experimental data processing. A Digital Micrograph^{TM} script available from an open source was used to convert the experimental stack of diffraction patterns from the Digital Micrograph^{TM} file format (.dm3) to that of MATLAB^{TM} (.mat). Processing procedures of the MATLAB^{TM} script

include filtering out X-ray counts from diffraction patterns by a 3×3 pixel mask, calculating the normalized variance map image from the filtered stack of diffraction patterns and azimuthal averaging of the map using bi-linear interpolation to produce variance plots. Another version of this script also corrected for relative shifts between diffraction pattern centers during the FEM scan. The shift is due to inadequate tilt-shift compensation capabilities in the NBD mode of JEOL ARM200F. Those are caused by several factors which can be summarized in one sentence – the aberration-corrected ARM200F was optimized for the purpose of using it as a STEM, sacrificing flexibility of the TEM mode tuning, especially in the nano beam (NBD) mode. Note that the increased column height to include the CEOS corrector makes the tilt-shift compensation even more challenging as compared to the 2010F model which is the corrector-free version of ARM200F.

MATLAB^{TM} scripts were also developed for diffraction pattern fringe contrast and separation analysis from the bilayer samples. They allowed easy pixel information retrieval on multiple mouse clicks, easy input of experimental parameters and other information needed for the analysis thorough automated pop-up dialogs, subsequent processing of the obtained data and outputting the results and plots with desired formatting.

A model for atomic-displacement-induced diffuse scattering was proposed and decoherence in a STFEM experiment based on that model was simulated by M. Treacy. The simulation assumed kinematical scattering of a fully coherent electron wave. Three distinct periodic models of disordered silicon were used. Those are; a random model, with no bond length or angle constrains; a CRN model with a fixed bond distance,

approximately tetrahedral coordination and dihedral angle variation; and the paracrystalline model – regions with 1.2-1.6 nm diamond cubic grains, which are packed together at the expense of large strains, embedded in a CRN matrix. Both the random and the CRN models had a period represented by a cubic cell of a 4.524 nm edge containing 4096 Si atoms. The paracrystalline model had a triclinic cell, which can be closely approximated by a cubic cell with edge length of about 2.67 nm.

Kinematical intensities were computed for 1000 orientations of the single cell for a 100 keV Gaussian probe of 1 nm resolution. Periodicity was avoided in order to avoid artefacts such as Bragg reflections from the supercell. The intensities were obtained from explicit calculation of the wave function contributions from each atom in the cell on a 512×512 grid of k_x and k_y diffraction vector component values both spanning the interval [-12.8, 12.8] nm. Each atom in the cell was randomly displaced along the Cartesian x, y and z axes according to a Gaussian distribution with root-mean-square (r.m.s.) displacement in the range 0.0 to 0.15 nm. A set of 100 such displacement patterns were generated for each cell orientation and the scattering was averaged over the set. The origin of the cell was also shifted randomly relative to the probe to ensure uniform sampling.

CHAPTER 3

TILTED DARK-FIELD TEM MODE FLUCTUATION ELECTRON MICROSCOPY STUDIES OF AMORPHOUS CARBON

3.1. Information Theory Aspects of Tilted Dark-Field TEM images

Intuitively, coherent scattering from perfectly random samples should not carry any information other than the total scattered intensity. In particular, one would expect tilted dark-field TEM images from very thin, perfectly amorphous samples to contain information only on the intensity scattered into the objective aperture or, in other words, the mean intensity in the image. A naive statement about the image intensity would sound like it should be constant throughout the image since the sample is perfectly random (uniform intensity distribution). In reality TDF TEM images are speckly. They look much like the laser speckle, or the screen of an old cathode ray tube TV set when it is on but not tuned to any channel. Naturally a question arises: "Is it a shot-noise?" On the first look the intensity distribution from a TDF TEM image actually does look like shot-noise statistics. However, as the reader will see below, it turns out that both the shot noise and uniform intensity contain more information than just the mean intensity.

Information theory developed by C.E. Shannon gives answers to the question about information stored in an image. It proposes an "entropy" as a measure of information

$$S = -k\int P\ln(P)dI\,, \tag{3.1}$$

where P stands for the probability of having intensity I. The scaling parameter k is a positive constant which accounts for the choice of a unit of measure [195]. For instance, it is equal to ln2 if binary bits are chosen. Generally, entropy is a measure of disorder.

Taking the constant equal to the Boltzmann constant renders the quantity in (3.1) as a measure of "disorder" in thermodynamic systems, with thermal equilibrium being the most likely state – usually the most "disordered" state. According to the second law of thermodynamics this state is reached when the entropy is maximized. There's a similar principle in information theory – the principle of maximum entropy (POME). According to POME the minimally prejudiced assignment of probabilities is that which maximizes the informational entropy. It can be shown that it is the negative exponential distribution, which maximizes entropy when information about the mean only is available

$$P(I) = \frac{1}{\langle I \rangle} \exp\left(-\frac{I}{\langle I \rangle} \right) \ . \tag{3.2}$$

It is derived readily using the usual Lagrange multiplier method to maximize (3.1) subject to the only constraint on $\langle I \rangle$, but I leave it out from the scope of this work. I will remark however, that it is the identical result obtained for the Boltzmann distribution when the mean energy is constrained. In that instance, we replace $\langle I \rangle$ with $k_{\mathrm{B}}T$ where $k_{\mathrm{B}}$is the Boltzmann constant, and T is the absolute temperature in Kelvin. Note that the method described gives a unique solution.

The negative exponential distribution is also explained phenomenologically in [196], where it is derived as a result of the assumption that the scattered wave function amplitude at any point is a complex number with its real and imaginary parts being Gaussian-distributed with the same standard deviation.

Getting back to TDF images, let me point out that neither the intuitive uniform distribution nor the normal distribution, which closely resembles actual TDF image

statistics, maximize entropy subject to just one constraint on the mean. On the other hand negative exponential distribution does not fit the intensity distribution of experimental images. Note that an image exhibiting a characteristic negative exponential intensity distribution would be dominated by dark speckle, which is contrary to experimental observations. It is clear, therefore, that experimental images contain more information than just $\langle I \rangle$ being fixed.

It was noted earlier, with regards to laser speckle, that if one adds intensities from a number images with different versions of spatial intensity distribution with the same negative exponential statistics, then the resulting image statistics are in fact described by the Gamma distribution. Note that addition of different versions of the negative exponential distribution, which arises from coherent scattering, is equivalent to incoherent superposition. Experimentally, it corresponds to imaging with an incoherent source that can be viewed as a superposition of a set of uncorrelated sources (say *m* sources). Indeed, the Gamma distribution may be obtained simply by accumulating contributions from each of the *m* sources. If $P(I_1)dI_1$ and $P(I_2)dI_2$ are probabilities of intensity contributions at the same image pixel from sources 1 and 2, respectively then the probability of this intensity combination at that pixel is their product, i.e. $P(I_1)P(I_2)dI_1dI_2$. Assuming expression (3.2) for either of the sources with the same mean $\langle I_0 \rangle$, $P(I_1)P(I_2)dI_1dI_2 = \frac{1}{\langle I_0 \rangle^2} \exp\left(-\frac{I_1 + I_2}{\langle I_0 \rangle}\right) dI_1dI_2$ is obtained. In order to obtain the probability $P(I)dI$ of having intensity I it should be noted that $P(I)dI \neq P(I_1)P(I_2)dI_1dI_2$ since I_1 and I_2 are interdependent through the constraint on

the total pixel intensity, i.e. $I = I_1 + I_2$. This means that $P(I)dI$ can be obtained by integrating out one of the interdependent variables, which turns out to be equivalent to performing a self-convolution

$$P(I)dI = \int_0^I P(I - I_1)P(I_1)dI_1 dI = P \otimes P(I)dI \,, \tag{3.3}$$

where I_2 is relabeled as I for convenience and the integration range [0, *I*] is the range of possible values of I_1. Inserting (3.2) in (3.3) gives

$$P(I) = \frac{1}{\langle I_0 \rangle^2} I \exp\left(-\frac{I}{\langle I_0 \rangle}\right). \tag{3.4}$$

Further, $\langle I_0 \rangle$ (the mean of each contributing image) is obtained from $\langle I \rangle = \int_0^\infty I \; P(I)dI$ to be $\langle I \rangle$ /2, as anticipated. This modifies (3.4) so that $P(I) = \frac{2^2}{\langle I \rangle^2} I \exp\left(-\frac{2I}{\langle I \rangle}\right)$ or $P(I) = \frac{2^2}{(2-1)!\langle I \rangle^2} I^{(2-1)} \exp\left(-2\frac{I}{\langle I \rangle}\right)$. One can already recognize the Gamma distribution (see (1.5)). Repeating this convolution *m* times, for *m* incoherent sources, yields its general form. As expected, *m* = 1 of one renders the equation (3.2).

This interesting result suggests that experimental TDF TEM images obtained with partially coherent electron source may have Gamma distribution intensity statistics. In the light of the described illumination incoherence theory the parameter *m* of the Gamma distribution is interpreted as the number of incoherent components of the illumination. Apparently, this parameter must also pop out from the information theory and must be related to the additional information about the amount of incoherence in the source.

Indeed, POME suggests another means of arriving at the Gamma distribution. Moreover, it doesn't require *m* to be an integer, which turns out to be convenient as the reader will see later. Therefore, let us first express the Gamma distribution in the general form in order to account for non-integer inputs

$$P(I) = \frac{1}{a\Gamma(b)}\left(\frac{I}{a}\right)^{b-1} \exp\left(-\frac{I}{a}\right). \tag{3.5}$$

Note that the Gamma function $\Gamma(m)= (m-1)!$ for positive integer *m*, so both expressions, (3.5) and (1.5) are valid.

According to POME, there is a unique probability distribution $P(I)$ of the variable I subject to certain constraints which maximizes the entropy (3.1). The constraints can be expressed as

$$c_i = \int g_i(I)P(I)dI \,. \tag{3.6}$$

with i=1,2,…,n, where g_i are some functions, c_i are constant and n is the number of constraints. Using the Lagrange multiplier method one can show that the Gamma distribution (3.5) maximizes the entropy subject to the constraints $c_1 = \int_0^\infty I\, P(I)dI$ and $c_2 = \int_0^\infty \ln I\, P(I)dI$. In other words the entropy is maximized by the Gamma distribution when the mean intensity $\langle I \rangle$ and the mean of the intensity logarithm $\langle \ln I \rangle$ are fixed, since

$$\int_0^\infty I\, P(I)dI = \langle I \rangle, \text{ and} \tag{3.7}$$

$$\int_0^\infty \ln I \; P(I)dI = \langle \ln I \rangle . \tag{3.8}$$

Indeed, according to the Lagrange multiplier method, the variation of the functional

$$F[P] = \underbrace{S[P]}_{\text{entropy}} - \sum_{i=1}^{n} \underbrace{\lambda_i}_{\text{Lagrange multipliers}} \times \underbrace{\left[\int g_i(I)P(I)dI - c_i \right]}_{\text{constraint equation}}$$

must vanish subject to the constraints (3.6) to maximize the entropy, i.e.

$\delta F[P] = -\int \left[1 + \ln P(I) + \sum_{i=1}^{n} \lambda_i g_i(I) \right] \delta P(I)dI = 0$, so

$$P(I) = \exp\left[-1 - \sum_{i=1}^{n} \lambda_i g_i(I) \right]. \tag{3.9}$$

On the other hand, applying the logarithm, multiplying by $P(I)$ and integrating the both sides of (3.5) and (3.9) separately yields

$$-\int_0^\infty P(I) \ln P(I)dI =$$

$$[\ln(a\Gamma(b)) + (b-1)\ln a] - (b-1)\int_0^\infty \ln I \; P(I)dI + \frac{1}{a}\int_0^\infty I \; P(I)dI , \tag{3.10}$$

where the normalization requirement $\int_0^\infty P(I)dI = 1$ was used, and

$$-\int_0^\infty P(I) \ln P(I)dI = 1 + \sum_{i=1}^{n} \lambda_i c_i . \tag{3.11}$$

Comparing (3.10) with (3.11) yields the constraint expressions $c_1 = \int_0^\infty I\ P(I)dI$ and

$c_2 = \int_0^\infty \ln I\ P(I)dI$, QED.

This comparison also gives expressions that relate Lagrange multipliers to the parameters *a* and *b* of the Gamma distribution (3.5). However, expressions that relate the Gamma distribution parameters to the constraints, i.e. to $\langle I \rangle$ and $\langle \ln I \rangle$ are to be derived. Here I present the only the outcome of the derivation, which can be found in the Appendix,

$$ab = \langle I \rangle . \tag{3.12}$$

$$\psi(b) - \ln b = \langle \ln I \rangle - \ln \langle I \rangle , \tag{3.13}$$

where ψ is the Digamma function defined as $\psi(x) = \frac{1}{\Gamma(x)} \frac{\partial}{\partial x} \Gamma(x)$. Now, using the beginning of the asymptotic series $\psi(x) = \ln x - \frac{1}{2x} + \sum_{n=1}^{\infty} \frac{\zeta(1+2n)}{x^{2n}} \approx \ln x - \frac{1}{2x}$ for large values of the argument, (3.13) can be rewritten as $\ln b - \frac{1}{2b} - \ln(b) = \langle \ln I \rangle - \ln \langle I \rangle$ which yields

$$b = \left[2\left(\ln \langle I \rangle - \langle \ln I \rangle \right) \right]^{-1} . \tag{3.14}$$

Inserting (3.12) and (3.14) in (3.5), and relabeling *b* = *m* the Gamma distribution can be written in the form.

$$P(I) = \frac{m^m}{\Gamma(m)} \frac{I^{m-1}}{\langle I \rangle^m} \exp\left(-m \frac{I}{\langle I \rangle} \right), \tag{3.15}$$

with

$$m = \left[2\left(\ln\langle I \rangle - \langle \ln I \rangle \right) \right]^{-1}, \text{ and} \tag{3.16}$$

The parameter *m* in (3.16) can also be written in terms of the arithmetical mean and the geometrical mean $\langle x \rangle_G \equiv \left(\prod_{i=1}^{n} x_i \right)^{1/n}$, i.e.

$$m = \left[2 \ln \frac{\langle I \rangle}{\langle I \rangle_G} \right]^{-1}, \tag{3.17}$$

since $\langle \ln I \rangle = \ln \langle I \rangle_G$.

It is worth noticing that the variance of the distribution (3.15) is equal to $\langle I \rangle^2 / m$ and, consequently, the normalized variance is 1/*m*, or using (3.17)

$$V = 2 \ln \frac{\langle I \rangle}{\langle I \rangle_G}. \tag{3.18}$$

Obviously the constraints (3.7) and (3.8) are actually equivalent to the constraint on the mean and the variance.

Here I summarize the above derivation with the following statement. If the statistics of the variable I is constrained only by information on the mean and the variance (or, with equivalent outcome, its geometric mean), then it is described by a Gamma distribution (3.15) with the parameter *m* defined by (3.17).

It is now time to see if the theoretically-predicted Gamma distribution is obeyed by the experimental data.

3.2. Results and Discussion.

Fig. 8 is the plot of the normalized variance obtained by calculating (1.1) for each image of the series of experimental TDF images from amorphous carbon, each recorded at a particular tilt of illumination.

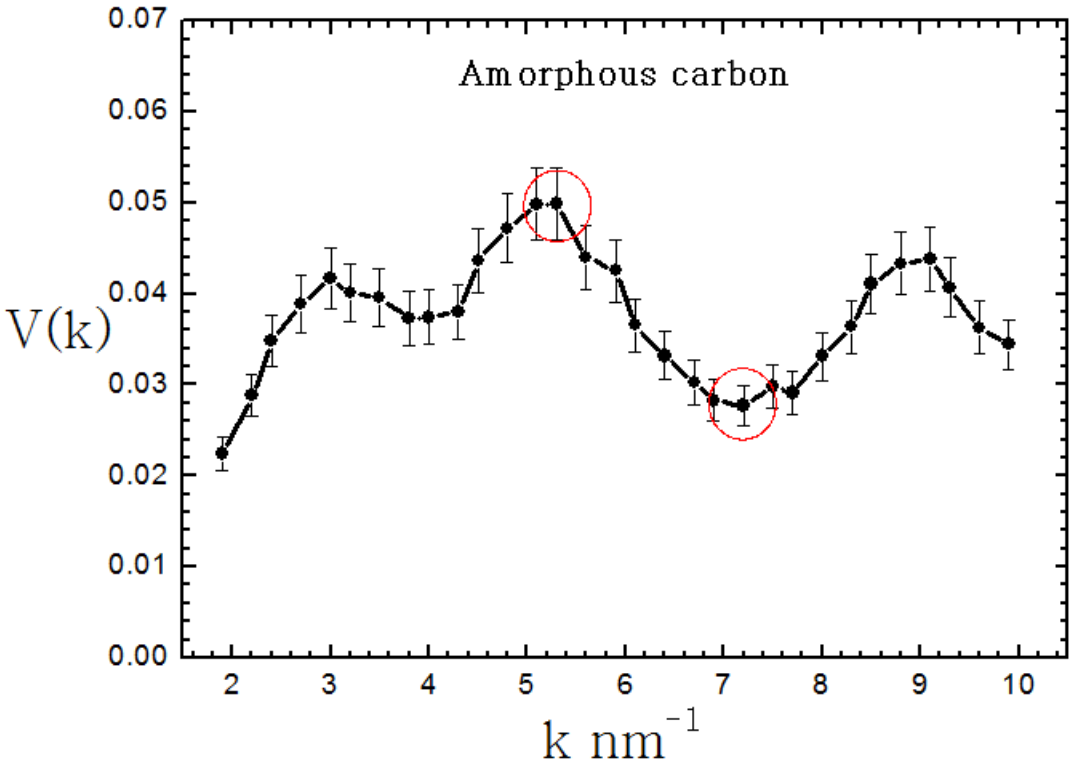

Fig. 8. Normalized variance versus scattering vector for a set of tilted dark-field images of amorphous carbon taken for 30 different tilts at 200 keV. Peaks of variance indicate MRO. The peak near 3 nm^{-1} may be due to graphitic (002) planes, the other two peaks at about 5 nm^{-1} and 9 nm^{-1} are most probably due to the diamond (111) and (220), (311), (222) reflections combined, respectively.

Fig. 9 and Fig. 10 show two of the 30 images of the TDF FEM data with corresponding normalized histograms. A naive interpretation would infer that the bright and dark speckle in these TDF images arise from constructive and destructive interferences from tiny ordered regions. However, random arrangements of atoms throughout the thickness of the sample can also generate bright/dark speckle [197, 198]. So a statistical treatment is needed to distinguish between those occurrences.

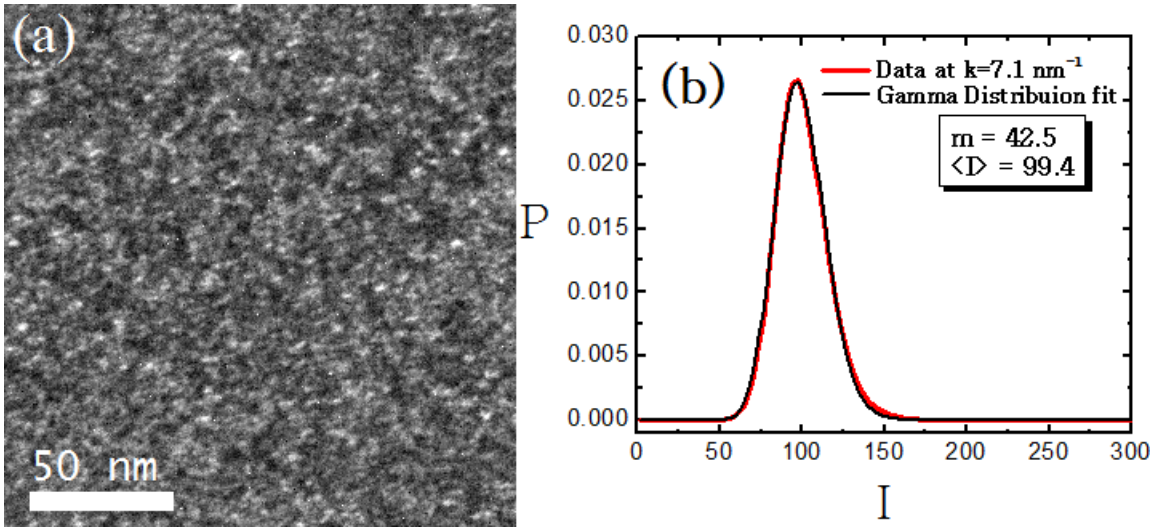

Fig. 9. (a) – Tilted dark-field image of the amorphous carbon sample at the tilt corresponding to the dip at 7.1 nm^{-1} of the normalized variance plot above. (b) – The intensity histogram of this image, and the fit to a gamma distribution with $m \approx 42$, $\langle I \rangle \approx 100$.

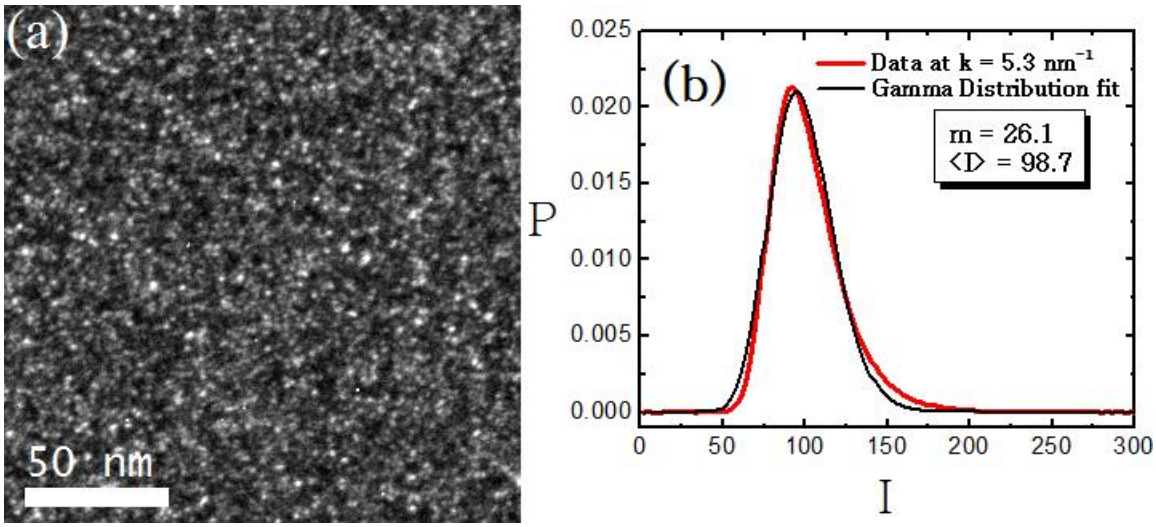

Fig. 10. (a) – *Tilted* dark-field image of the amorphous carbon sample at the tilt corresponding to the peak at about 5 nm^{-1} of the normalized variance plot above. (b) – The intensity histogram of this image, and the fit to a gamma distribution with $m \approx 26$, $\langle I \rangle \approx 100$.

The histograms are fitted to a Gamma distribution function (3.31). Strikingly, the fit is near perfect in Fig. 9 which corresponds to a data point from the very bottom of the second dip (circled) in the normalized variance plot of Fig. 8 obtained by calculating (1.1) for each TDF image corresponding to a particular tilt. It appears that the Gamma

distribution formula is obeyed remarkably well in experimental variance dips as opposed to the peaks where there are small differences between the fit and the data. This slight misfit, which is illustrated in Fig. 10 corresponding to a data point from the very top of second peak of Fig. 8 (circled), indicates that there is more information present than just m and $\langle I \rangle$. Obviously, a perfectly random sample seen from different angles has the same appearance statistically. This suggests that the scattering from such a sample should not differ between different tilts of the incident illumination, so the variance plot should be flat and not show any dependence on scattering vector, k. It is these subtle differences that signal the presence of MRO. For example, the reflection at 7.1 nm^{-1} is forbidden in all carbons except for its tightly-curved allotropes (C_{60} fullerene, for instance). It arises due to high concentrations of 5-rings (or 7-rings). It is therefore a signature of curved carbon allotropes. Of course this reflection in diffraction from such molecules embedded in an amorphous matrix will be at a noise level. However, one would expect it to appear in FEM data as a variance peak at the corresponding scattering vector. Indeed, curved carbons were detected in shungite in [184] but they are actually absent in our sample as a dip is observed instead.

One could argue that these slight deviations from Gamma distribution statistics of tilted dark field images may be caused by shot-noise inherent to the experiment. In order to ensure that the variance profile signals the presence of MRO, and not the shot noise, the following simulation was carried out. Shot noise was properly added to the model images that were initially constructed to have Gamma distribution statistics with parameters matching the experimental values, i.e. m_0 = 30, $\langle I \rangle_0$ = 100. The resulting

"noisy" images were constructed to differ in $\langle I \rangle$, which was varied from 1 to 1000 throughout the set. Their histograms were then all fitted to Gamma distribution to see how shot noise altered them. It appeared that only when $\langle I \rangle$ fell as below 10 does the shot noise start to dominate the image statistics, causing them to deviate significantly from the original Gamma distribution (Fig. 11 (a)). The fit is rather good for the case of $\langle I \rangle$ = 100 (Fig. 11 (b)). It is then safe to say that there is no significant shot noise influence on the statistics at high signal-to-noise ratios, in particular, at about experimental 100 counts per pixel. It is further corroborated by the plot in Fig. 12 (a) which shows that the noise starts affecting the mean at about $\langle I \rangle = 50$ as the signal to noise ratio drops. Interestingly, the shot noise suppresses the value of the parameter *m* as evidenced by Fig. 12 (b).

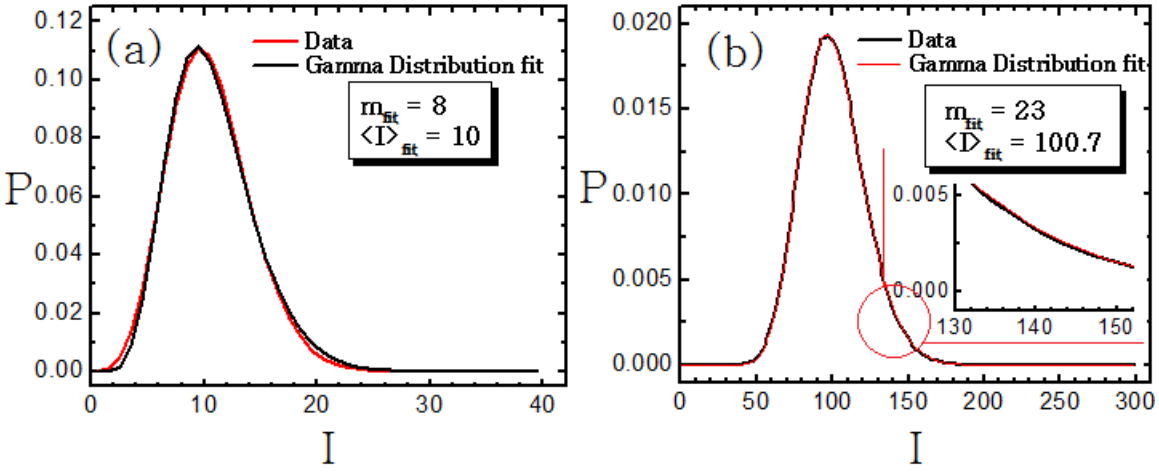

Fig. 11. Histogram of intensity of "noisy" images obtained by adding shot noise to the original image for which the intensity histogram is a Gamma distribution, with parameters m_0 = 30 and $\langle I \rangle_0$ = 100. (a) $\langle I \rangle$ = 10, the fit deviates slightly from the "noisy" image statistics as a result of a poor signal to noise ratio. (b) $\langle I \rangle$ = 100, noise does not introduce any significant deviation from the noise-free Gamma distribution.

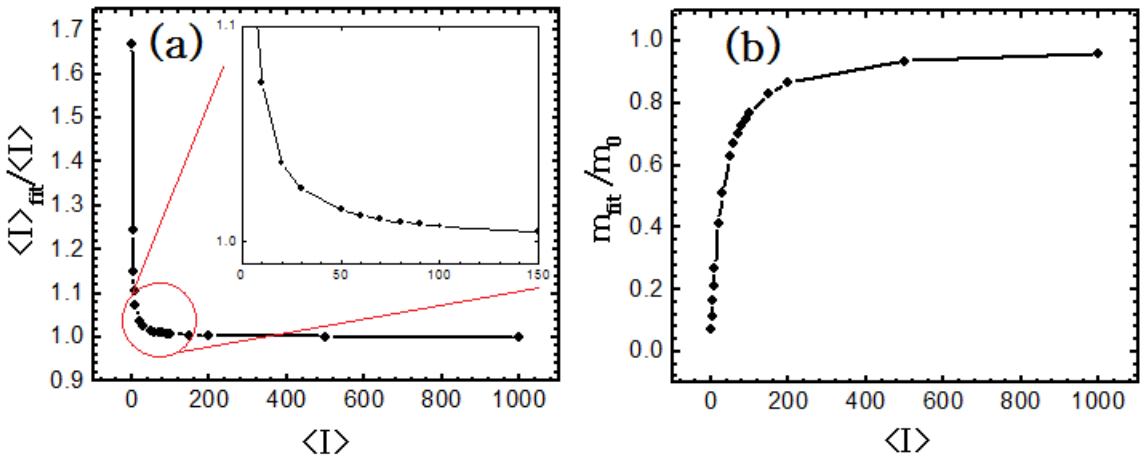

Fig. 12. (a) – Ratio of the parameter $\langle I \rangle_{fit}$ of the Gamma distribution fit to the simulated $\langle I \rangle$ versus $\langle I \rangle$. As the signal to noise ratio drops the noise starts affecting the mean at about $\langle I \rangle = 50$. Eventually, the ratio soars to the point where the noise clearly dominates the signal. (b) – Ratio of the parameter m_{fit} of the Gamma distribution fit to the original $m_0 = 30$ versus $\langle I \rangle$. As the signal to noise ratio drops the fitted parameter m_{fit} plummets.

Note also that when the data deviates from the Gamma distribution in Fig. 11 (a) it does so in a different manner if compared to that observed experimentally, which presumably arises from the presence of MRO in Fig. 10 (b). Namely, the fit goes below the data at the onset of the right shoulder of the peak in case of noise and above in case of the MRO. The opposite is true for the left shoulder.

It can be herein asserted that the equation (1.5) is obeyed remarkably well for data obtained from tilted dark-field TEM images of amorphous carbon. However, there is a significant inconsistency with the claim that the parameter *m* in (1.5) is indeed the number of incoherent sources which comprise the experimental illumination: fits to data give $m \approx 25\text{-}45$, yet we know experimentally that the illumination has potentially high spatial coherence in field emission guns. This suggests that we should have been nearer $m \approx 1$, if *m* is indeed arising from spatial incoherence in the illumination. This surprise result indicates that we have been misinterpreting the meaning of the parameter *m*.

Note that the derivation of the Gamma distribution from the POME is more general, in the sense that it is done without any definite assumptions about the illumination source or the sample. Moreover, the parameter *m* is not restricted to integer numbers. This enables one to propose an alternative source for *m* in the light of the surprising inconsistency of the incoherence model with the experimental results, which was discovered earlier above. It is possible that we have been underestimating the effects of the interaction of the sample with the beam, such as structural changes in samples caused by the electron beam impact, and, it is likely that the large value of *m* observed in the TDF FEM experiment on amorphous carbon is due to decoherence of scattering within the sample which occurs during the exposure time required to acquire the data. The parameter *m* now naturally becomes the measure of decoherence or, more likely, both coherence and decoherence. Moreover, the normalized variance of a perfectly amorphous sample itself becomes a measure of decoherence, since $V = 1/m$. It gets suppressed with increasing decoherence (or *m*) which explains the discrepancy between the kinematical and experimental variances as the former doesn't account for decoherence (i.e. $m = 1$). However, as it was pointed out earlier, one should keep in mind that in the case of a sample that is not ideally amorphous, there is more information available then just the mean and the variance. Consequently, the distribution is no longer a pure Gamma distribution (as observed in (Fig. 10) and its normalized variance is not exactly constant and is not equal to the inverse of *m* (as observed in Fig. 8). Nevertheless, the suppression of variance and its measured value can give a ballpark figure for *m* which then will give some general idea about coherence/decoherence in the experiment. In

particular, the number of $m \approx 25\text{-}45$ observed in the TDF FEM experiments suggests a significant decoherence that occurs during the exposure time.

In the following chapters, the decoherence is studied experimentally in the STFEM mode by examining amorphous carbon and silicon samples, as well as an ultra nano-crystalline diamond sample. Possible underlying mechanisms of decoherence are discussed as well.

CHAPTER 4

DECOHERENCE IN SCANNING TRANSMISSION FLUCTUATION ELECTRON MICROSCOPY OF AMORPHOUS CARBON AND AMORPHOUS SILICON. BEAM ENERGY DEPENDENCE.

4.1. Probe Coherence and Scattering Decoherence Effects.

Although sufficiently high illumination spatial coherence at high brightness of the source is attainable in modern TEMs equipped with field-emission guns, coherence is an important factor that should not be overlooked in FEM experiments. In particular, one should be careful to have similar coherence conditions for comparability of different FEM experiment results [199], otherwise speckle contrast may vary significantly.

Fig. 13 shows examples of a-Si diffraction patterns (a and d), probe images (b and e), as well as saturated probe images obtained with the 10 μm CL aperture for the two cases of JEOL's preset spot sizes of the NBD-S condenser lens configuration providing high and low demagnification of the source image. Those are probes 1 and 2 of Table 1 with nominal diffraction limited resolution of 2.4 nm and probe flux of 10^6 electrons/(nm^2×sec) and 0.23×10^8 electrons/(nm^2×sec), respectively. The experimental full-width half-maxima (FWHM) for these spots were measured directly from their images to be 2.3 nm and 3.2 nm, which corresponds to about 2.6 nm and 3.6 nm effective resolutions, respectively (Fig. 13 (e) and (b) insets). The difference in spatial coherence is illustrated by the rings in the Airy pattern in Fig. 13 (f) and their absence in Fig. 13 (c). The resulting speckle contrast differences are seen in Fig. 13 (a) and (d).

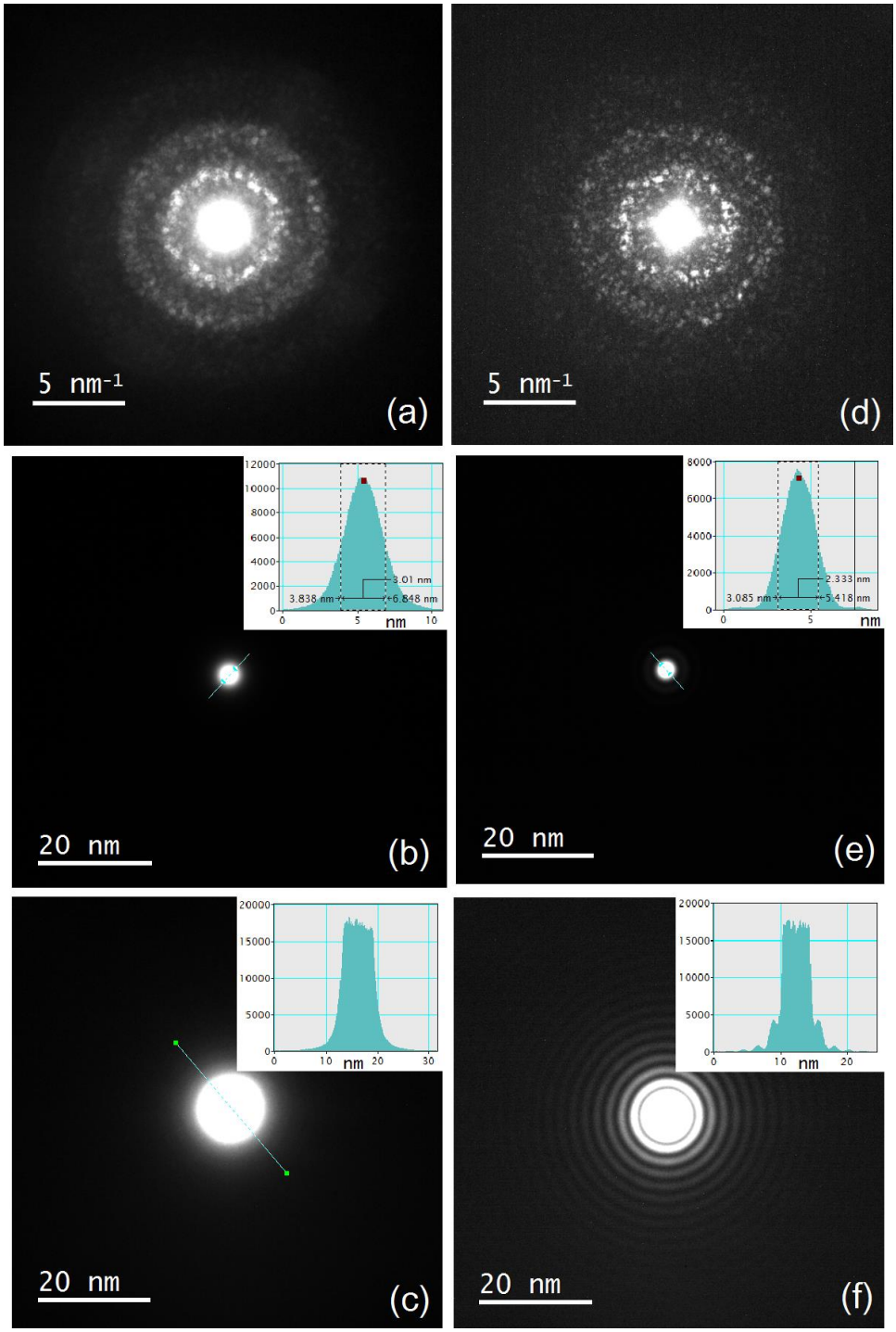

Fig. 13. Illustration of electron probe parameters, in a JEOL ARM200F instrument operated at 200 keV in the NBD-S mode of the condenser system with 10 μm probe-forming aperture. Diffraction speckle from a-Si, unsaturated and saturated probe images with profile insets are presented for two different probes, both having nominal diffraction limited resolution of about 2.4 nm. (a), (b) and (c) – low spatial coherence (Probe2). (d), (e) and (f) – high spatial coherence (Probe 1).

Fig. 14 compares the experimental STFEM data for the two condenser system settings. It illustrates the effect of spatial incoherence on the normalized variance, which was also discussed recently with regards to STFEM in [199]. Results for two different exposure times are shown for each condenser setting. It should be mentioned that the case of high coherence requires longer exposure times because the high demagnification of the source image reduces the beam fluence, rendering the FEM data more prone to noise effects. In the case of 0.8 sec exposure of the Probe 1, the shot noise dominates the variance at high k, which causes $V(k)$ to rise with increasing k. The shot-noise introduces an additional term to the variance expression (1.1) that is inversely proportional to the mean scattered intensity, which falls as k increases [135]. Higher fluence at 1.6 sec exposure suppresses the noise term at high k because of stronger signal. However, the higher fluence also results in larger decoherence which suppresses the variance signal slightly.

In essence, decoherence is a type of diffuse scattering, but as will become apparent later, it is caused mainly by beam-induced atomic displacements in the sample, which subtly alter the underlying structure being probed during the exposure of the diffraction patterns. In turn, this causes the speckle intensity to fade when the speckle is time-averaged over several seconds needed to record the data. Multiple scattering and energy-loss processes may be another reason for variance suppression in thicker samples. Ironically, because FEM is so sensitive to speckle intensity fluctuations, it is therefore much more strongly affected by decoherence than are simple diffraction and imaging.

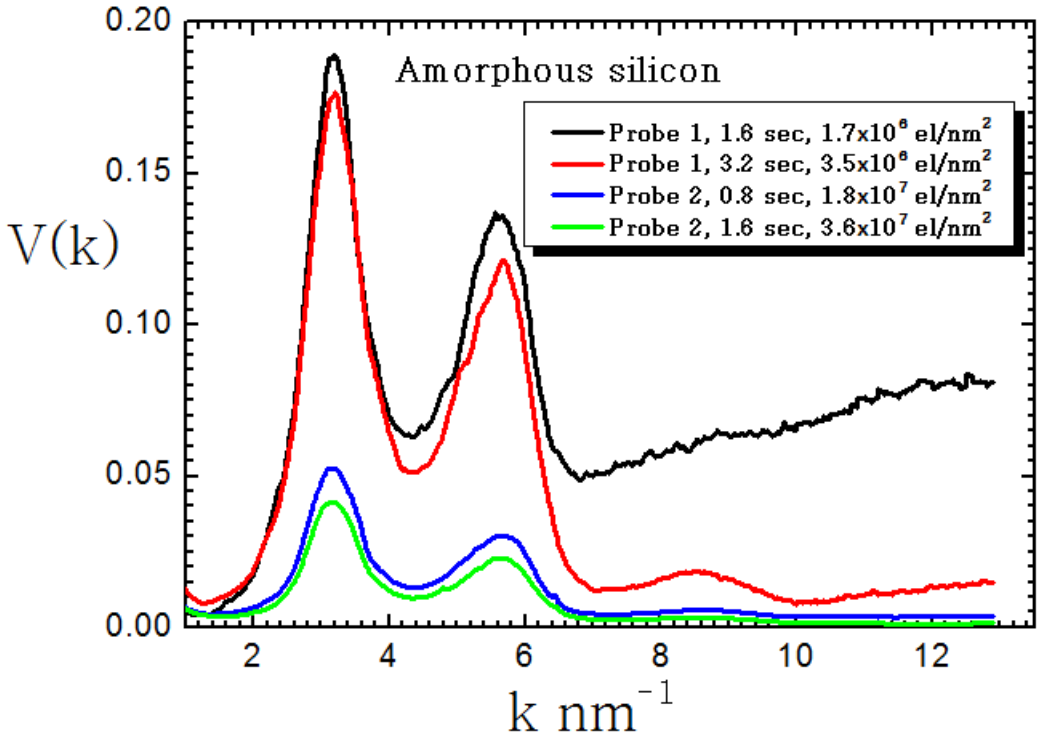

Fig. 14. Experimental 200 keV STFEM data from a-Si showing the influence of spatial incoherence on the normalized variance. All plots were obtained with a nominal, diffraction-limited, probe resolution of 2.4 nm. Exposure times along with electron fluence values for each case are given in the legend. There is about factor of four difference in peak variance between high (Probe1) and low (Probe 2) spatial coherence cases.

The peak variance is about 0.18 at $k \approx 3.1$ nm^{-1} in the case of the high-coherence, red plot of Fig. 14. The background variance, however, as estimated from the dip between the first two peaks of the 3.2-sec exposure, is closer to 0.05, indicating suppression by a factor of 20 relative to the coherent kinematical value of 1, despite the high spatial coherence. The variance is suppressed even more in the case of the lower spatial coherence of Probe 2 relative to Probe 1, although it should be admitted that a part of it comes from increased decoherence due to the difference in fluence (which is a factor of five between the cases of red and blue curves). However, it is safe to say that there is at least a factor of two difference coming solely from the illumination incoherence

because doubling the exposure of either Probe 1 or 2, which increases decoherence at a fixed illumination incoherence, does not make much difference as seen from comparison of black and red, or blue and green traces of Fig. 14.

Several mechanisms of decoherence were explored in [200] through simulation of kinematical scattering in random, CRN and paracrystalline models of silicon (with topologically cubic grains, 1.2-1.6 nm in diameter). Although there is a pronounced difference in the normalized variance between these models, they are all essentially diffraction-amorphous. Fig. 15 taken from [200], and shows the computed variance for the case of the diffuse scattering from beam-induced large r.m.s. amplitude atomic displacements. Surprisingly, low-*k* variance peaks arise in the CRN model (Fig. 15 (a)) at the same values as from the paracrystalline model Fig. 15 (c). Unlike the CRN peaks, the presence of peaks from the paracrystalline model, and their absence from the random model, were indeed expected. Suppose there was a small concentration of tiny ordered regions (grains) in the CRN, then the diffraction signal from them would be lost in the background signal from the disordered matrix. Indeed, there are no peaks appearing at an r.m.s. displacement amplitude of 0.0 (Fig. 15). However, the peaks would arise if decoherence was "turned on". This is because the coherence volume around each scatterer effectively shrinks. In the ideal case of the coherence volume matching the size of the grains, the signal from random arrangements outside the coherence volume, which comprise most of the background, would be suppressed and the signal from ordered grains would emerge out of the background. This interesting result suggests that there is probably more order in the CRN than was thought before.

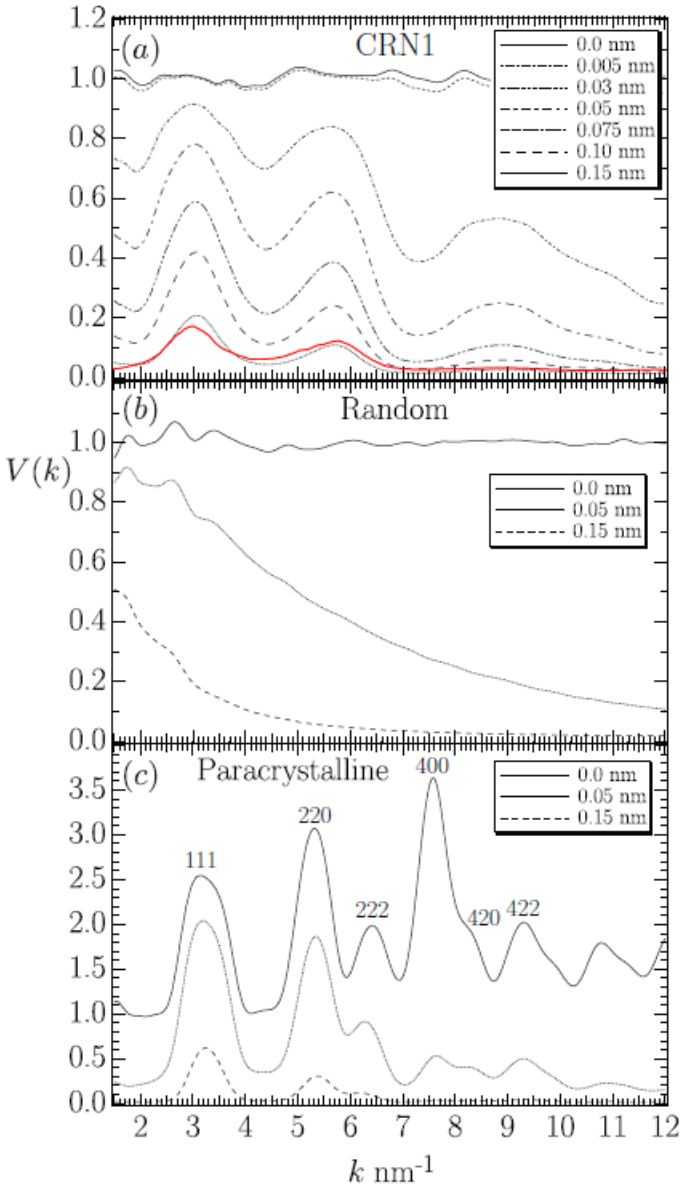

Fig. 15. Normalized variance computed by Treacy, for two models of amorphous silicon, assuming randomized and uncorrelated atomic displacements that are induced by interactions with the electron beam. Displacement root-mean square amplitudes, between 0.0 and 0.15 nm are presented. (a) – CRN model, (b) – Random model, (c) – Paracrystalline model. Variance is strongly suppressed with increasing r.m.s. displacement amplitude, especially at high *k*. Peaks that match qualitatively the experimental data emerge in the CRN model as opposed to the random model. The red trace in (a) is the high spatial coherence experimental data from Fig. 14.

Another important result emerged from the comparison of the simulation in Fig. 15 with the experimental, high-coherence variance in Fig. 14. It turned out that the

variance profile at large atomic displacements in the CRN model resembles strongly the red trace of the high illumination coherence experimental data obtained from amorphous silicon (superimposed in Fig. 15). It should be mentioned, that, although other mechanisms, including inelastic scattering events and electron beam spatial incoherence, indeed suppress the variance, the resulting profiles differ from the experimental one [200]. The partial spatial incoherence of the illumination results in variance suppression at all k values rather than in stronger suppression at larger k. Inelastic scattering also results in uniform suppression but only the peaks are affected. The primary effect of inelastic scattering is randomization of the phase of the scattered wave. This results in suppression of peaks above the baseline normalized variance, $V(k)=1$, in the paracrystalline model, and its absence in the CRN and random models.

It is the variation in scattering from regions with small systematic spacings that is responsible for the high-k signal. Random atomic displacements, R, disrupt the phase of the scattered wave, $\exp(i(kr_i+kR))$. Obviously, for a fixed r.m.s. displacement the additional random term kR in the phase is enhanced for large k values, hence the severe decoherence at high-k values. Simply stated, the structure with smaller systematic spacing's is more easily randomized by the atomic displacements of the order of those spacings.

Although the simulations suggest that the atomic displacements are the primary cause of decoherence, since they emulate experimental variance suppression (albeit qualitatively), the actual picture the displacements is probably far more complicated than the simple model described here. Furthermore, it is clear, that all of the mentioned mechanisms along with the multiple scattering contribute to speckle variance

suppression. Multiple scattering further decoheres the propagating wave in thick samples if it is already partially coherent when entering the sample. Multiple scattering alone can not decohere the beam, but it can further degrade the wave that is already partially coherent. Similar to the case of illumination incoherence, the variance is suppressed equally at all *k* values [200].

Note also, that the simulated large-amplitude "diffuse scattering" is not thermal in nature, unlike the one discussed in [201]. This is a non-equilibrium process triggered by electron beam impact. Some of the electron scattering events will transfer a large momentum to the atom according to the high-*k* tail of the atomic differential scattering cross section. Some of these occurrences will damage the structure by breaking bonds. The sample will then rearrange its structure because of the strain fields introduced by the damage. It is likely that these constant rearrangements of structure during the exposure time comprise the actual atomic displacement events that suppress the diffraction speckle in our STFEM experiments.

This structural dynamic was earlier hinted at by the static probe diffraction from amorphous materials; when the probe is fixed at a certain location on the sample diffraction patterns are observed to twinkle. Strong speckle from ordered atomic arrangements appear and disappear at observable time scales of the order of a second. Fig. 16 (a) and (b) are two consecutive diffraction patterns from the same region of amorphous silicon, each obtained by 3.2 second exposure of the amorphous silicon film. Such long exposures were dictated by the low current in the Probe 1 (see Table 1). The pattern (c) in Fig. 16 is pattern (a) minus pattern (b), it highlights the twinkling as the black and white spots indicate that speckle appeared or disappeared in the consecutive

exposure. Obviously, each of these patterns themselves exhibit time-averaged speckle relating to structural fluctuations on shorter time scale. This time-averaging lowers speckle sharpness in the recorded diffraction patterns, hence the suppression of the variance of FEM data.

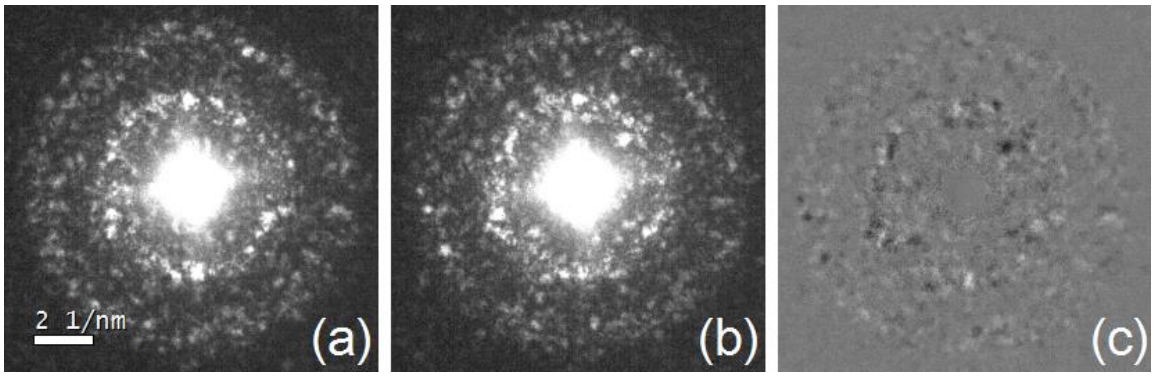

Fig. 16. Stationary-probe diffraction patterns of a-Si (a) and (b) that were taken sequentially with 3.2 sec exposure using the probe with 2.4 nm nominal resolution and 10^6 electrons/(nm^2×sec) electron flux, and their difference (c), which highlights twinkling of the diffraction speckle on observable timescales.

The twinkling is not merely an illumination or readout noise issue, since specific Bragg reflections appear and disappear. The probe motion due to microscope instabilities was observed to be negligible, so probe instability is not a source of the twinkling either. Such time-averaged probe motions are closely related to spatial incoherence. Optical back-projection of the moving probe at the sample plane, back to the source, makes it analogous to a source whose instantaneous emissions deviate slightly from the optic axis – in effect introducing an angular width to the source when time-averaged.

The twinkling cannot be attributed to phonons either, since the observable timescale of the twinkling ranges from tens of milliseconds to seconds. It is clear that the electron beam interaction with the amorphous sample is modifying, or damaging, its structure at slow, human-observable time scales. The sample can be imagined as a layer

of self-regenerating popcorn under a scanning blowtorch flame; it does not stay still under the beam.

4.2. Decoherence. Beam Energy Effect.

In the present study, the extent of decoherence was varied by changing both the incident electron beam- and sample-specific parameters. Here we present the results from an experiment where the beam energy was varied. Fig. 17 shows experimental STFEM normalized variance from a-C, (a), and a-Si, (b), samples, at 80 and 200 kV obtained using the Probes 5 (1.3 nm resolution, 1.12×10^{9} electrons/($nm^2\times sec$) electron flux) and 3 (1.5 nm resolution, 0.23×10^{8} electrons/($nm^2\times sec$) electron flux), respectively. The probes had similar (but partial) spatial coherence due to identical demagnification of the source in both cases. The coherence was sacrificed for a larger electron fluence in order to achieve acceptable signal-to-noise from the scattering with high momentum transfer, which would otherwise dominate the tail of the variance plot (see the black trace of Fig. 14 for an example). The fluence was held approximately constant, 9×10^{8} electrons/nm^2, for each experiment by adjusting the exposure times appropriately; 0.8 sec at 80 keV versus 3.7 sec at 200 keV. Probe sizes were also approximately matched with about 1.3 nm versus 1.5 nm nominal resolution respectively.

The computed variance from the paracrystalline model is also plotted in each graph. Note that the baseline normalized variance is equal to 1 in models, as expected for the fully coherent kinematical case, and the peaks rise above this baseline value because the model structure was not random.

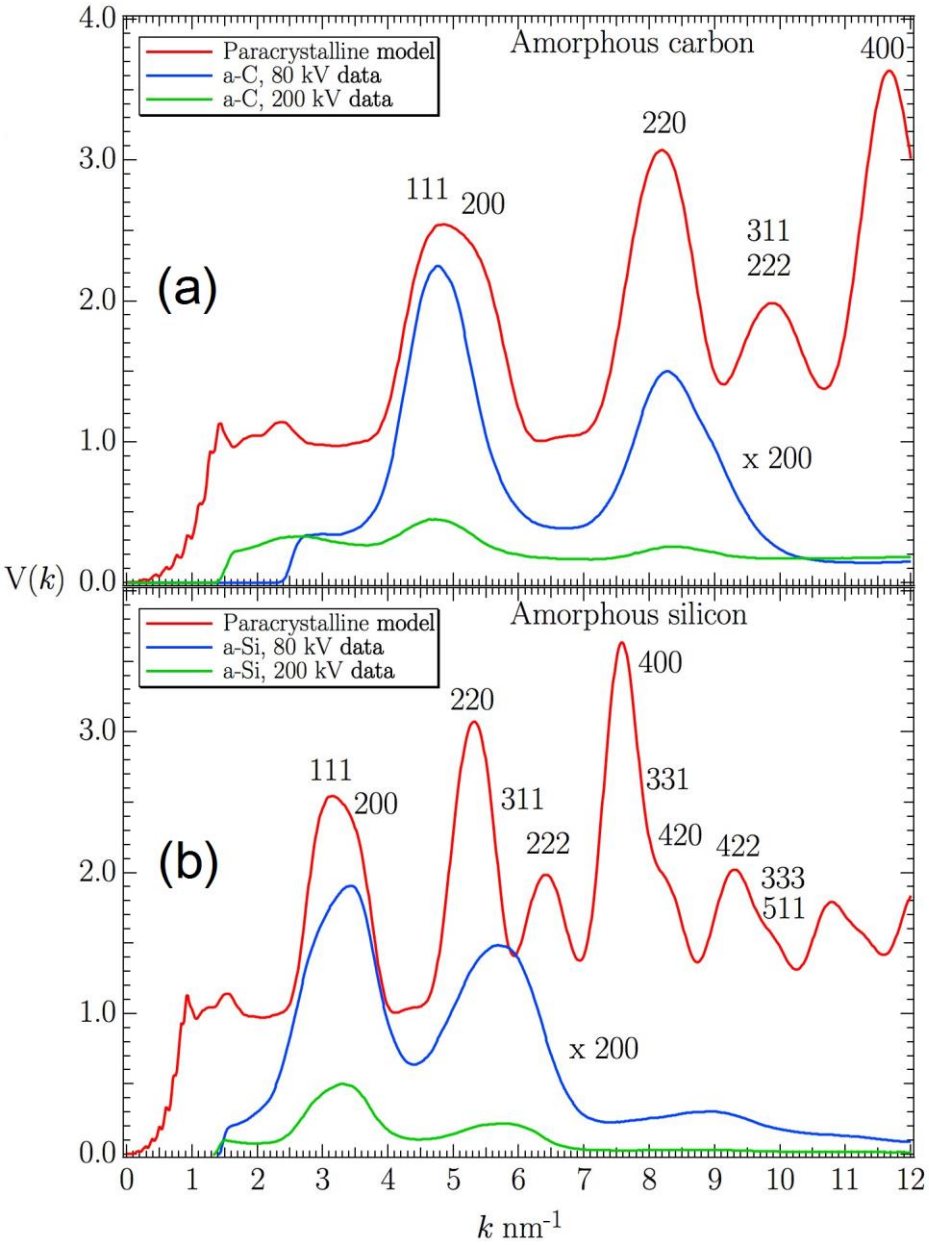

Fig. 17. Normalized variance plots computed for paracrystalline silicon model, compared with experimental data obtained by STFEM for 80 kV (Probe 5) and 200 kV (Probe 3) electrons for (a) – a-C film and (b) – a-Si film. The suppression of the experimental variance is arising from both illumination spatial incoherence (to increase fluence rate), and from displacement decoherence. The spatial coherence, the fluence (9×10^8 electrons/nm^2) and the probe size (about 1.5 nm) are approximately the same at each voltage (9×10^8 electrons/nm^2). The normalized variance at 200 kV in both samples is strongly suppressed relative to that at 80 kV. More severe suppression at higher-*k* values is observed in all cases.

Both materials exhibit similar variance plots, with two pronounced peaks and a weaker third peak, because they are both tetrahedrally coordinated materials based on the cubic diamond structure. As it is seen from Fig. 17 (b), the experimental baseline variance is about 10^{-3}, suggesting $m \approx 1000$, which in this case results from the combined incoherence due to spatial incoherence of the source and decoherence. The latter follows from the observation that higher voltage suppresses the variance, despite the fact that the illumination spatial coherence is unchanged. By kinematical scattering theory there should be almost no difference in the normalized variance as a function of voltage, yet the reader can see about a factor of four difference between the 80 keV and 200 keV experimental variance from the amorphous silicon. Moreover, the variance at 200 kV is increasingly suppressed for higher k values relative to that at 80 kV, as the phase disruption by the displacement decoherence is of course enhanced for a higher voltage.

In summary; decoherence was proposed to explain the discrepancy between the experimental and theoretical, kinematical variance. The experimental data from thin amorphous films obtained at high spatial illumination coherence condition was compared to the kinematical variance computed for several models of disordered silicon. A simple model of atomic displacements emulated the experimental data well. However, more realistic models of sample motion in response to the stress introduced by the electron beam impact are needed. In addition, the possibility for the CRN model to contain more ordering than was thought before was noticed when analyzing the variance behavior with the increasing displacement decoherence. The suppression of the variance because of increasing electron beam impact was confirmed through STEFEM experiments where the beam energy was varied, strengthening the decoherence argument.

CHAPTER 5

DECOHERENCE IN STFEM OF AMORPHOUS CARBON AND AMORPHOUS SILICON. SAMPLE THICKNESS DEPENDENCE. INTERFEROMETRIC BILAYER DIFFRACTION.

5.1. Sample Thickness Dependence of Variance

Recently, Treacy proposed an empirical expression for the sample thickness dependence of the kinematical normalized variance [194]

$$\big(V(k)-1\big)t = c\,, \tag{5.1}$$

where V is the normalized variance, t is the sample thickness in the beam direction and c is a constant. Through additional conjecture $V_m(k) = V_1(k)/m$, where $V_1(k)$ is the coherent kinematic variance with m = 1, they arrived at the modified version for the case of illumination incoherence

$$\big(mV_m(k)-1\big)t = c\,, \tag{5.2}$$

$$\text{or } V_m(k) = \frac{1}{m}\left[\frac{t_0}{t}\big(V_1(k,t_0)-1\big)+1\right]. \tag{5.3}$$

As before, m is the parameter associated with incoherence, V_m indicates the variance dependence on m, and t_0 is a known thickness. The equation (5.1) was investigated through simulations of kinematical scattering in models with various degrees of crystallinity, and was proved to become inaccurate only at about 99% crystalline volume fraction [194].

This chapter reports on attempts to examine the expression (5.2) experimentally. At the time when the experiment was conceived, it had already been clear that the

expression (5.2) did not hold for experimental conditions because of decoherence, which is inherent to the experiment. In particular, a deviation from the dependence of the variance on the inverse of thickness was expected to be observed. This is because the parameter m is no longer fixed for all k values unlike the kinematical scattering case considered in [194]; m possibly becomes $m(k)$.

It should be mentioned that a set of amorphous samples with known relative thicknesses were required for this study. In order to hold other experimental parameters constant, one sample with quantized thickness areas in the field of view of the microscope would be ideal. This would also eliminate any slight modifications of the microscope parameters which are otherwise possible when swapping samples.

5.2. FEM of FIB-Prepared Multi-Step Amorphous Carbon

An attempt to carry out the study described above was made using the multi-step amorphous carbon film which was described in Chapter 2. Its ADF STEM image is shown in Fig. 18. Adverse experimental effects such as contamination and the diffraction pattern center shift (described in Chapter 2) during the STFEM scan hampered the collection of acceptable quality FEM, so any meaningful variance plots were not attainable. Fig. 19 is an example of such a plot, which was obtained with the probe 3 configuration for the STFEM experiment providing 1.5 nm nominal diffraction-limited resolution and electron flux of 2.44×10^{8} electrons/(nm$^2\times$sec). The central spot shift correction procedure, which was used for shifting diffraction patterns relative to each other in order to align central spots throughout the stack, was found to introduce additional background to the true variance (see Fig. 19 (a)) because of the relative shift of the CCD image features that were uncorrectable through gain normalization (large

particles on camera's scintillator film). This is a known issue for the retractable Gatan cameras. Each retraction/insertion of the CCD camera is capable of producing new particles and/or moving the existing ones on the scintillator film effectively undermining the gain normalization. Another adverse circumstance is the contamination that created an array of humps at the data collection positions in each of the probed areas (Fig. 20 (a)). It is possible that this introduced large additional thickness variance on top of the true variance (Fig. 19 (b)).

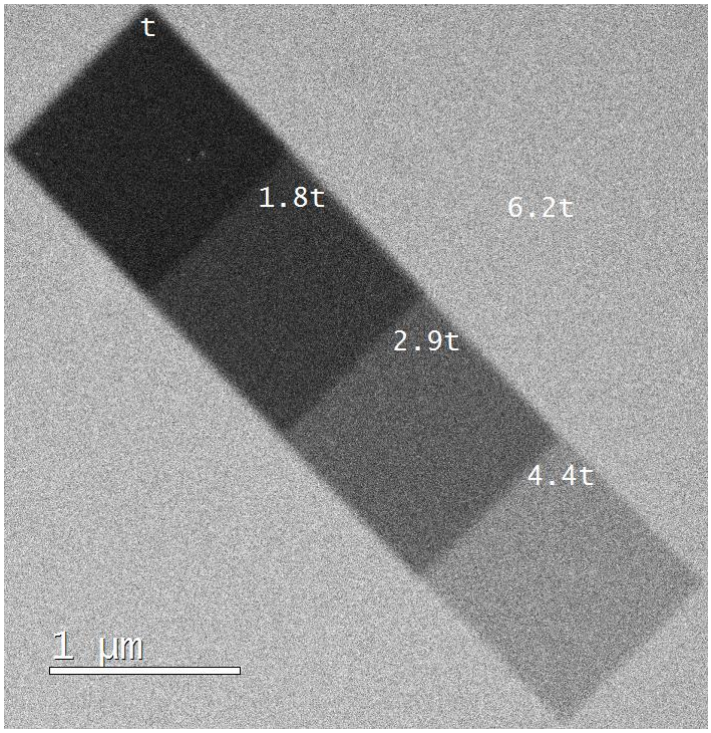

Fig. 18. HAADF STEM image of the stepped a-C sample prepared by Ga FIB milling, taken at 200 keV. Relative thicknesses are indicated in each area.

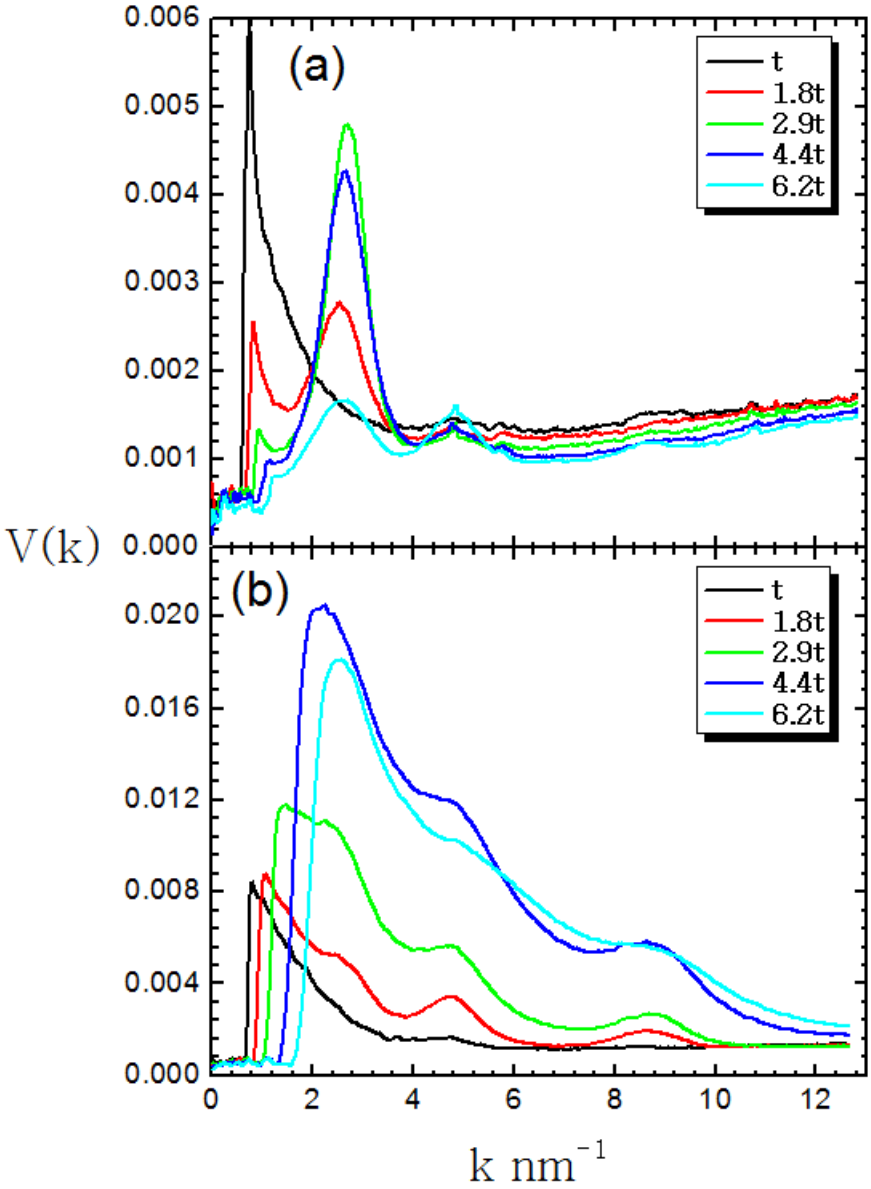

Fig. 19. Normalized variance plots for the stepped a-C sample, which was prepared by FIB, obtained at 200 keV using a probe with 1.5 nm resolution. Relative thicknesses for each of the steps are indicated in the plot legends. (a) – 2 sec. exposure of individual diffraction patterns. The large peak at about 2.8 nm may be associated with the Ga-ion FIB preparation. The carbon peaks are almost entirely buried under the variance background introduced by the diffraction central spot shift correction procedure; (b) – 3 sec. exposure. The Ga peak is partly cut by the saturated central spot. A small hole was burned by the electron probe in the thinnest area. All other areas showed carbon contamination after STFEM scans which means that thicknesses were altered. Most probably this accounts for the unexpected variance behavior with thickness for the probed areas.

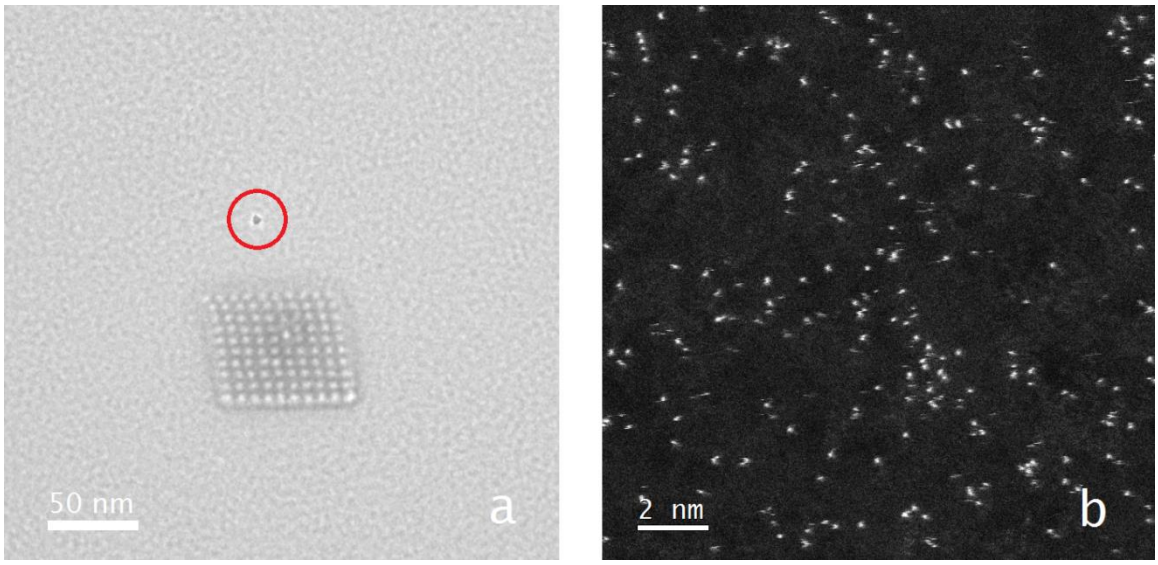

Fig. 20. (a) – TEM image illustrating the carbon contamination at the 10×10 grid of electron probe positions where STFEM data was acquired from the 30 nm thick amorphous carbon film at 200 keV. The tilted array indicates that the specimen was drifting. The circled region is a typical CCD camera artefact, a particle on the camera's scintillator film generated by insertion/retraction of the camera. The standard Gatan's gain normalization procedure was unable to correct for the contrast from some of the large particles. (b) – HAADF STEM image of the a-C sample treated with Ga-ion beam. Bright spots indicate Ga contamination.

The large variance peak at about 2.8 nm^{-1} in Fig. 20 (a) may result from Ga contamination. The other two peaks at about 5 nm^{-1} and 9 nm^{-1} are the carbon peaks. The HAADF STEM image in Fig. 20 (b) attests to the well-known Ga implantation issue in FIB-prepared samples. Further investigation of the variance dependence on thickness with the multi-step a-C sample was canceled due to this alleged Ga contamination. The reader will see in the next chapter that there is also the possibility that the 2.8 nm^{-1} variance peak results from presence of graphitic carbon.

Preceding the fabrication of the multi-step sample the thickness dependence experiment was done on the ultra-nanocrystalline diamond (UNCD) sample which offered variable thickness due to its wedge shape. However, this too failed because of the uneven variance contributions arising from the lack of ordering uniformity between areas

of different thickness that masked the thickness dependence (more in Chapter 6). Moreover, after dismissing the multi-step sample, a set of commercial PELCO SiO_2 and Si_3N_4 amorphous support films with known thicknesses (reported by TedPella Inc.) were explored. Unfortunately, the central spot shift issue was exacerbated with the SiO_2 samples (because of sample charging, probably) hampering the implementation of the experiment. The Si_3N_4 films were found to have considerable thickness variations. Moreover, the thinnest film turned out to be holey.

Although minor to the inadequate tilt-shift compensation and gain normalization issues described above, there were additional practical difficulties imposed by the CCD camera dynamic range. Exposure times that ensure acceptable signal to noise levels in the collected diffraction patterns vary broadly from the thinnest sample to the thickest one. The thinnest SiO_2 and Si_3N_4 films, for example, are about 8 nm thick which requires more than 3 sec. exposure for individual diffraction patterns. On the other hand this same exposure time saturates a larger area in the central part of the pattern for the thicker 50 nm sample. Another issue is the damaging of the thinnest films during the contamination cleaning process and/or the experiment.

5.3. FEM of Multi-Layer Amorphous Carbon

In another attempt to explore the FEM signal as a function of thickness, I fabricated the multi-layer amorphous carbon sample that was made from layers of equal thickness (Fig. 6). The area that was eventually selected for FEM experiments is shown in Fig. 21. The ratios of the film thickness to the plasmon mean free path value (t/λ) obtained from low-dispersion EELS spectra that confirm the obtained quantized-thickness structure are shown on each of steps.

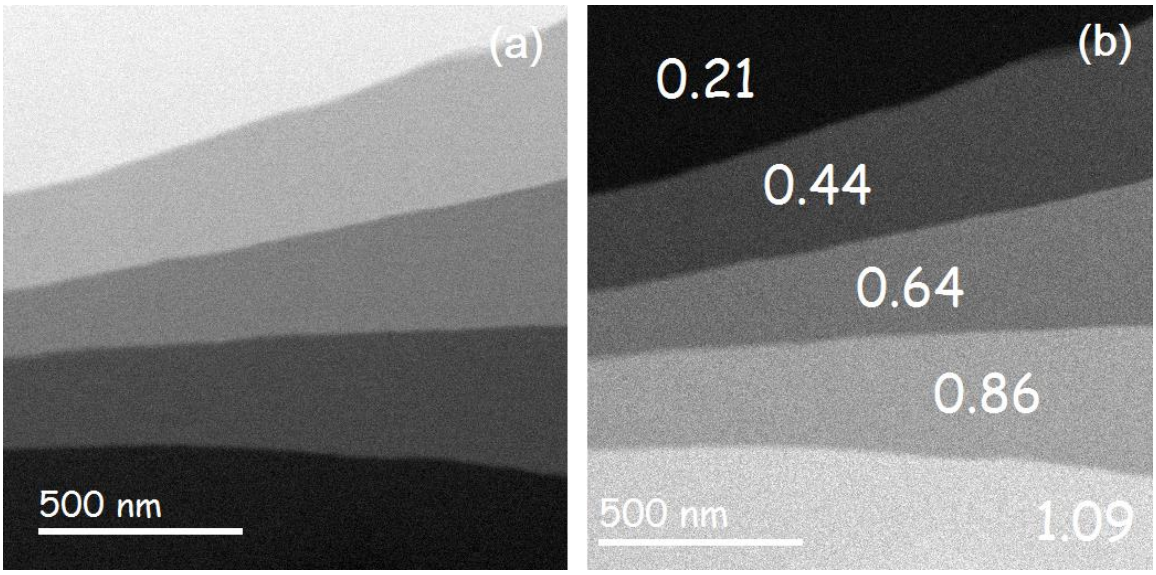

Fig. 21. Multi-layer sequence of carbon films arranged in a step-like structure. This comprises a 30 nm thick carbon film supporting a four-layer stack of sheets which are fragments of the same support film. (a) – STEM BF image. (b) – HAADF STEM image with t/λ values indicated on each step representing an increment in thickness of 30 nm.

Two STFEM datasets were collected at a pair of distant areas of the sample; one comprising a 4-step region, and the other comprising a 5-step region. Each datum from the datasets was acquired from the steps shown in Fig. 21 using the probe 3 configuration (see Table 1). Each individual diffraction pattern was recorded with a 0.8 sec exposure. Although equation (5.2) does not hold for the experimental data, as discussed above, some sort of inverse relationship between the variance and the sample thickness should still be observed experimentally. Curiously, the variance plots in Fig. 22 (a) and (b) do not attest to that. In fact the 111 peak for the single layer is always lower than that for the 2- and 3-layer samples, though it decreases with increasing thickness for areas other than the single layer area. Furthermore, the variance behavior at the 220 peak differs from area to area as seen from Fig. 22. This puzzling behavior was later observed in other areas of the sample (not shown here). It was suspected that this can be an experimental artifact but even carefully controlled experiments did not eliminate this issue.

Scrupulous examination of the diffraction pattern sets revealed the reason behind this mystery. It transpired that some of the diffraction patterns, except the ones from the single layer areas, have fringy 111 and 220 diffraction rings (see Section 5.4 of this chapter). For example, the diffraction data corresponding to the blue plot contains fringy diffraction patterns in both cases of Fig. 22. The cyan plot in the Fig. 22 (b) also contains considerable numbers of those patterns. In all of the mentioned cases the variance plots misbehave considerably (most clearly observed at the 220 peak of the Fig. 22 (b)).

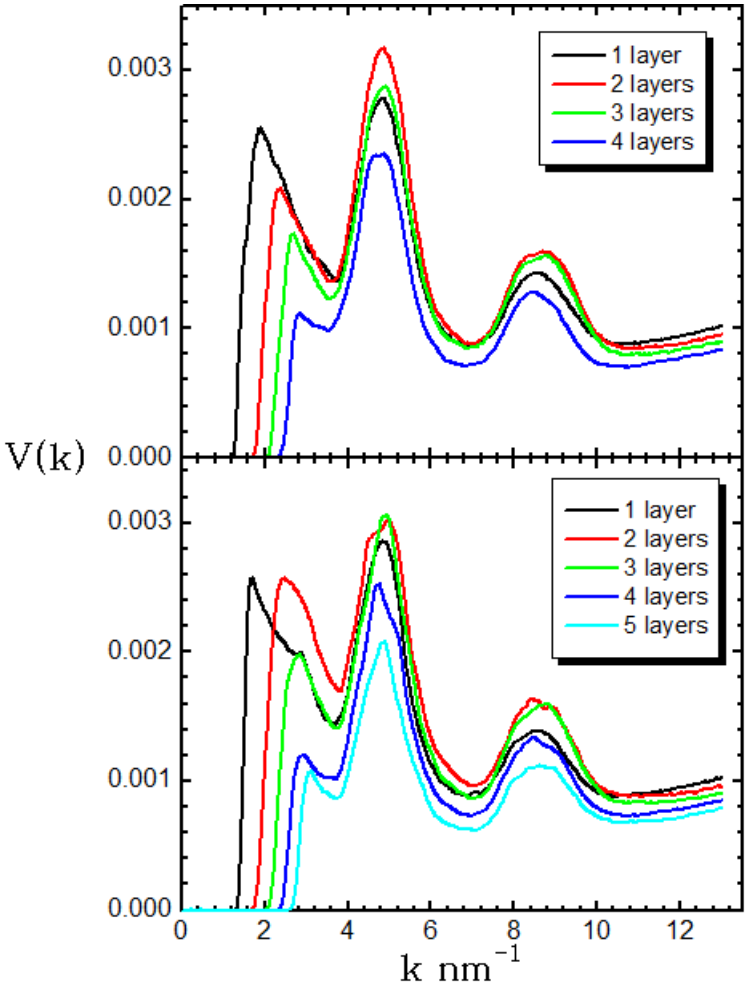

Fig. 22. Normalized variance plots for the multi-layered a-C sample obtained at 200keV using a probe with 1.5 nm resolution. Each trace corresponds to a different number of identical 30 nm thick layers traversed by the electron beam. Two different sets of areas were sampled producing figures (a) and (b). Gaps between the layers most probably account for the unexpected variance behavior in some of the areas.

As discussed in the next section of this chapter, the fringy diffraction patterns appear when the layers did not lie in perfect contact with each other. They probably rest on each other in a manner similar to the way cling-film attaches to itself, with many gaps and wrinkles. This is corroborated by the wrinkling (although of much larger scale) of the as-prepared single layer film siting on the copper grid (Fig. 23).

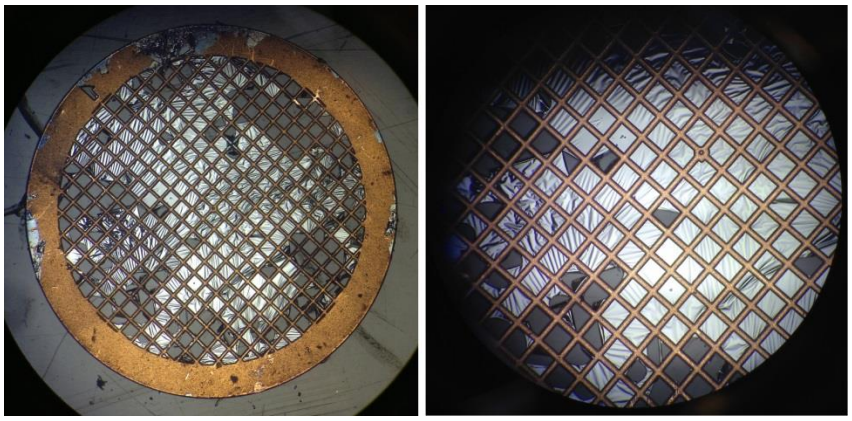

Fig. 23. Optical microscope view of the amorphous carbon film about 30 nm thick on a 300 mesh 3 mm copper grid showing large-scale wrinkling, with its a bit more magnified image on the right.

Unfortunately, it is concluded that none of the used samples were good enough for studies of the variance dependence on sample thickness.

5.4. Interferometric Diffraction in Bilayer Amorphous Carbon Sample

The unfortunate multi-layer a-C experiment enabled an opportunity to carry out a fine interferometric experiment. It was noticed that some of the diffraction patterns from the FEM stack had concentric fringes (Fig. 24 (a)). These were clearest for the bilayer regions. Three features of the fringy patterns should be noticed immediately (these will be discussed later in detail); (1) the fringes are broken and wavy; (2) they are finer (closer together) far from the center, and; (3) their contrast is enhanced at the diffraction rings but, overall, it decreases far from the pattern center where they finally fade.

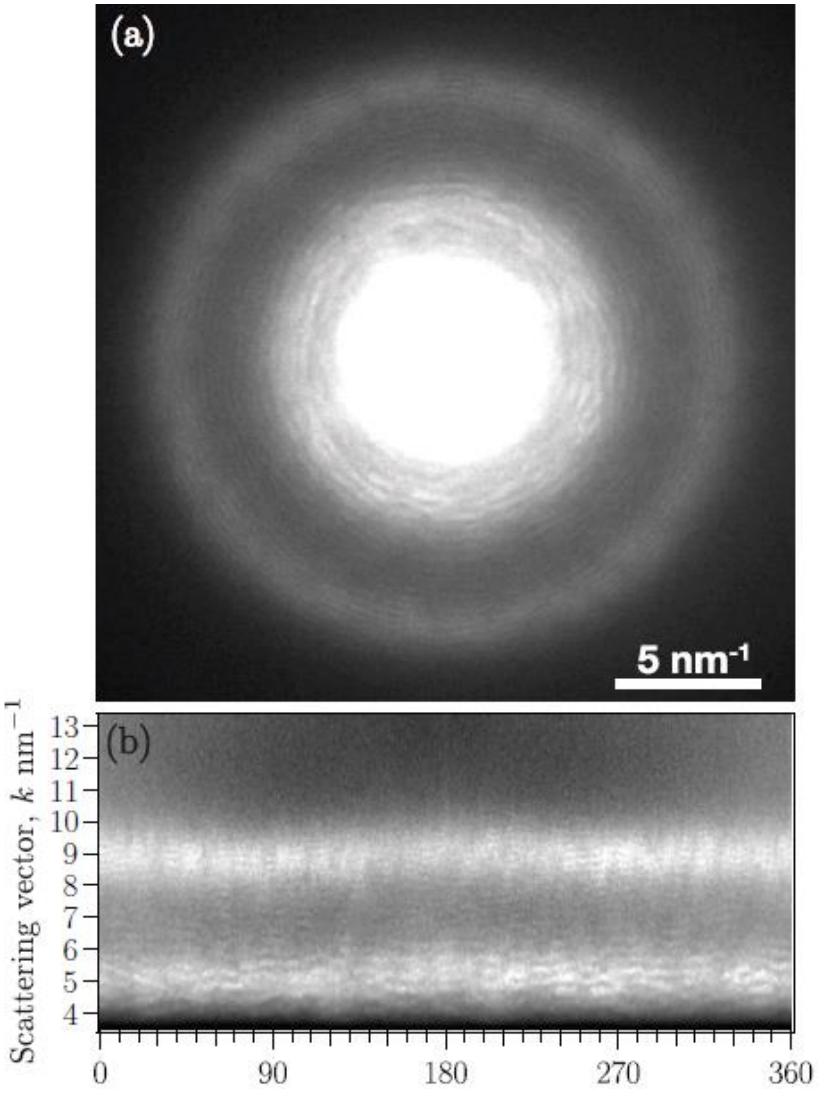

Fig. 24. (a) – Diffraction pattern from a bilayer of amorphous carbon taken at 200keV using a probe with 1.5 nm resolution. (b) – Same pattern 'unwrapped' so that the diffraction rings are horizontal. Intensity is rescaled. Wavy fringes are visible on the rings.

On closer examination fringy diffraction patterns appeared to be most pronounced in double-thickness areas and none were observed in single-thickness areas. It turned out that instead of an amorphous layer of thickness 2*t*, we obtained a bilayer with a gap *L* between layers along the beam direction, as depicted in Fig. 25, and the fringes arise because of interference between electron waves scattered from each of the layers. In essence, the fringes are reciprocal space modulations in the beam direction sampled by

the Ewald sphere with an effective width corresponding to the probe angle of convergence. These modulations are introduced by the bilayer shape factor of the sample and its frequency is proportional to the separation of the two layers $L+t$. The modulation envelope is nothing less than the so-called "relrod" structure (with frequency proportional to t) introduced by the single layer shape factor. The situation is analogous to double slit diffraction where the single slit intensity is modulated by fine fringes perpendicular to the line connecting the centers of the slits.

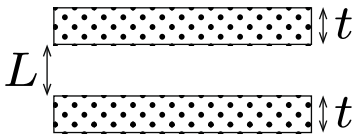

Fig. 25. A bilayer with a gap L and each layer having thickness t.

As was already noted, the fringes are finer farther from the center of the diffraction pattern (see Fig. 24). In order to explain this observation, it is instructive to consider a bilayer with identical crystalline layers that are identically oriented. The resulting diffraction pattern is then described in terms of the intercepts of the composite bilayer's reciprocal lattice with the Ewald sphere. The second layer that is separated from the first layer by the distance L along the optical axis introduces additional, large interlayer lattice spacings in the same direction, i.e. lower-frequency periodicity in real space, which makes the reciprocal lattice denser along the optical axis (Fig. 26). This density increases with L. Further, in the case of the convergent probe the Ewald sphere, having an effective angular width of 2α, samples more reciprocal lattice points farther from the origin (pointed out in Fig. 26 by vertical blue arrows). As explained later, this produces fringes inside the diffraction disks of angular width 2α that are finer in high-index disks.

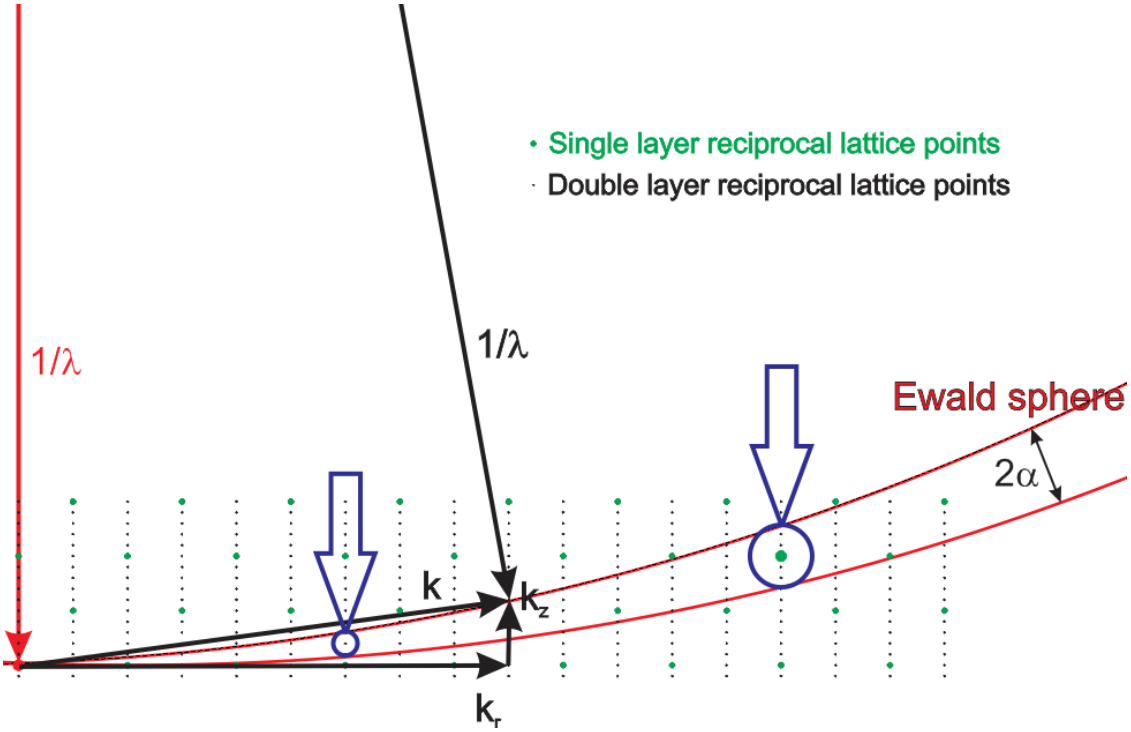

Fig. 26. Ewald sphere construction for a bilayer crystal film with superimposed reciprocal lattice points of a single-layer crystal film. It shows that the Ewald sphere for a convergent probe, having an effective thickness of 2α, samples more the reciprocal lattice points farther from the origin.

Actually, the fringes become finer even within distinct diffraction disks. In case of the convergent probe illumination and finite thickness of the layers the reciprocal lattice points can effectively be presented as finite thickness disks (Fig. 27), and the Ewald sphere crosses the bilayer reciprocal lattice disks. Because of its curvature the thickness of an intercept is smaller in projection further from the origin. It can be seen in Fig. 27 that this produces the characteristic fringe pattern inside the diffraction disk; fringes are perpendicular to the diffraction vector, and become finer in the direction of the vector. The more realistic picture of the reciprocal space modulations, explains the smoothness of the fringes. Obviously, in the case of the amorphous bilayer samples the described mechanism produces circular fringes centered at the zero-order beam that get finer farther from the center.

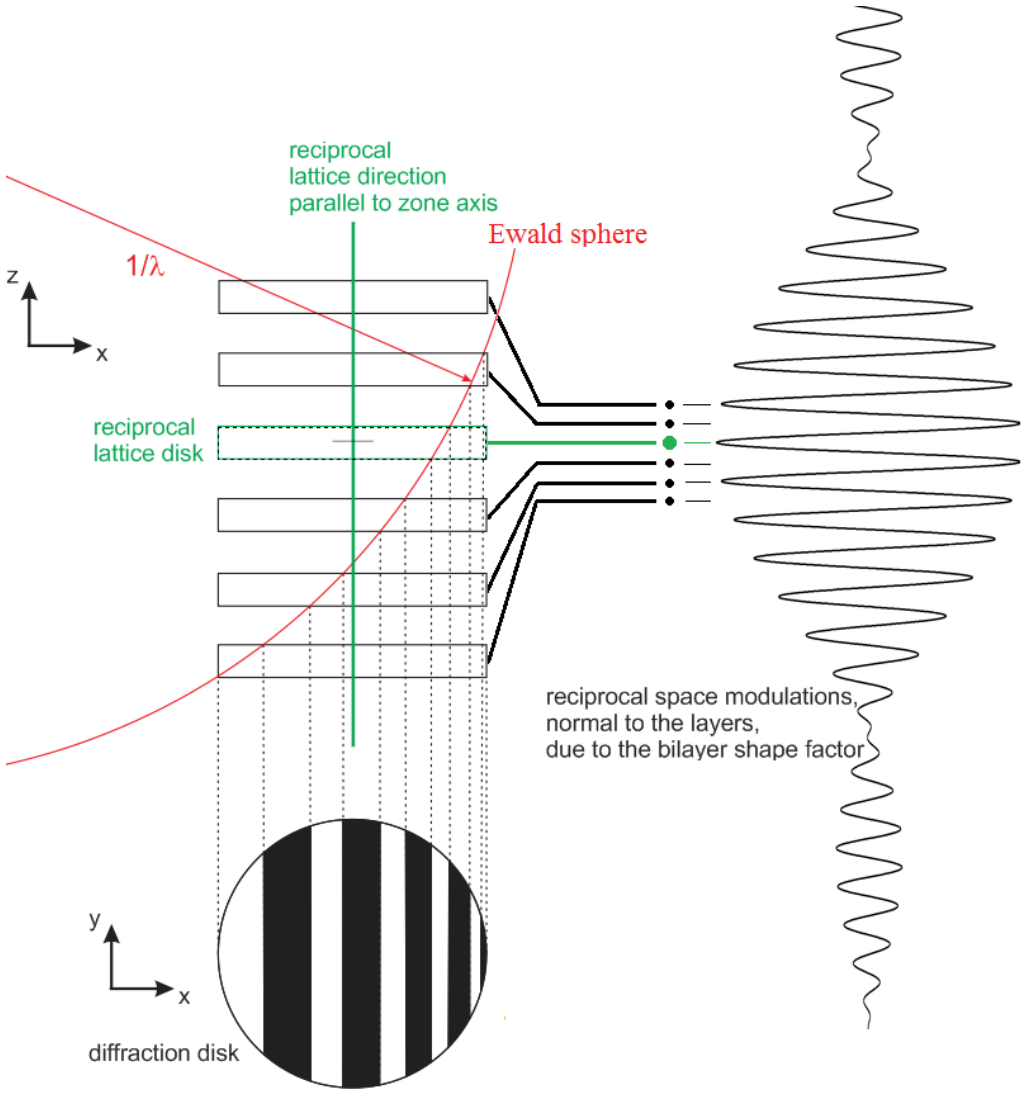

Fig. 27. Schematic explaining fringes in diffraction patterns from a crystalline bilayer structure. The Ewald sphere crosses the finely-spaced bilayer reciprocal lattice disks producing the characteristic fringe pattern inside the diffraction disk. More realistic picture of the reciprocal space modulations explains the smoothness of the fringes.

The irregularities of the fringes observed in experimental diffraction patterns (Fig. 24 (a)) are likely to be a consequence of structural irregularities within the probed volume of the sample; the random overlaps of the disks produced by the amorphous microstructure of the layers cause the observed fringe wiggling. Note that the thickness variation within the probed volume (1.5 nm probe, 30 nm thick film) is negligible compared to the thickness needed to cause a phase change that would shift the fringe.

Indeed, a simple calculation using the sample's mean inner potential (9.09 V for a-C [202]) shows that a thicknesses variation of about 24 nm is needed in an amorphous carbon sample probed by 200 keV electrons for the wave to incur a π/2 phase change; the phase change introduced by the material was estimated using

$$\Delta\varphi = \frac{2\pi}{\lambda}\frac{(E_0 + E)}{E(E_0 + E)} eU_o t\,, \tag{5.4}$$

where U_0 is the mean inner potential, E and E_0 are the kinetic and rest mass energies, respectively, and t is the material's thickness [203].

It can be inferred from the Fig. 26, which is the Ewald sphere construction for a bilayer crystal oriented at the exact zone axis, that for a reciprocal lattice point crossed by the Ewald sphere

$$\left(\frac{1}{\lambda} - k_z\right)^2 + {k_r}^2 = \left(\frac{1}{\lambda}\right)^2, \tag{5.5}$$

with $k_r = \sqrt{{k_x}^2 + {k_y}^2}$, where k_x, k_y, *and* k_z are the coordinates of the point in the reciprocal space. The equation (5.5) can be rearranged into

$$k_z = \frac{\lambda k^2}{2}, \tag{5.6}$$

where $k = \sqrt{{k_r}^2 + {k_z}^2}$. Approximating $k = \sqrt{{k_r}^2 + {k_z}^2} \approx k_r$ since k_z is small the equation (5.6) can be rewritten adding a subscript "*r*" to the k^2 in the numerator. However, I will relabel $k_r \to k$ in order to be consistent with the previous diffraction vector notation

$$k_z \approx \frac{\lambda k^2}{2}. \tag{5.7}$$

For two consecutive planes equation (5.7) gives

$$k_z^{(2)} - k_z^{(1)} \approx \frac{\lambda(k_2^{\,2} - k_1^{\,2})}{2} \approx \lambda \bar{k} \Delta k\,, \tag{5.8}$$

with $\bar{k} = (k_1 + k_2)/2$ and $\Delta k = k_2 - k_1$. Note that $k_z^{(2)} - k_z^{(1)} = 1/(L+t)$, where $L+t$ is the bilayer separation between, so (5.8) can be rewritten as

$$L + t \approx \frac{1}{\lambda \bar{k} \Delta k}\,. \tag{5.9}$$

Experimentally, the separation can be inferred from the fringe spacing Δk via (5.9). Indeed, in Fig. 28 (b) $1/\lambda \bar{k} \Delta k$ values are plotted for each pair of fringes at $\bar{k}$ in the diffraction pattern of Fig. 28 (a) and the resulting scatter plot is fitted to a straight line. The slight decline of the fitted line at high k is probably caused by both the approximation and the measurement error. The value of the separation, 640±100, was inferred from the fit value at 3.2 nm^{-1} (c-Si k_{111}).

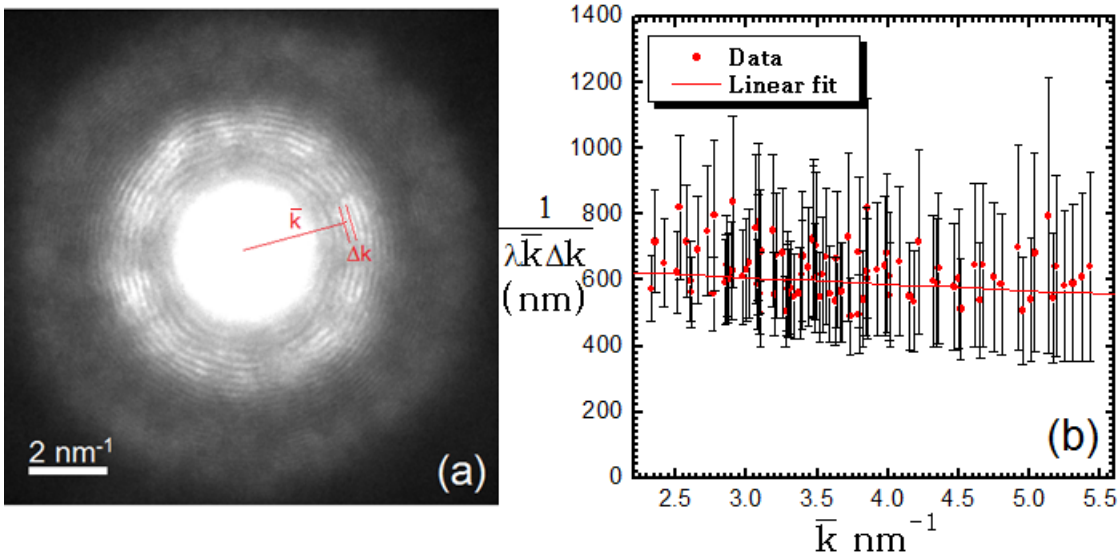

Fig. 28. Illustration of the bilayer fringe analysis. (a) – Diffraction pattern from a bilayer amorphous silicon taken at 200 keV using a probe with 1.5 nm resolution. (b) – Plot of $1/\lambda \bar{k} \Delta k$ vs $\bar{k}$ data collected from the pattern in (a) and the linear fit to the data. Error bars are computed assuming an error of one pixel in locating fringe maxima. The fit gives the bilayer separation value of about 640 nm.

The bilayer interferometric experiment was repeated with a-Si films in order to reproduce the experiment with another sample of different material. In fact, Fig. 28, which was chosen to illustrate the separation measurement method described above, shows an example of the data obtained from the bilayer a-Si sample. The latter was prepared as described in Chapter 2 (see Fig. 7). More experimental diffraction patterns were obtained at several positions of the electron probe along the bilayer region. This ensured distinct separation values for each pattern since the bilayer had a form of a hollow wedge, so the gap opens wider away from the tip (Fig. 7). Fig. 29 shows some of the unwrapped versions of these patterns. As expected the fringes are present and they get finer with increasing separation (at a fixed *k*). Graphs similar to the one in Fig. 28 (not shown), were plotted for these patterns and three other patterns that are not shown in Fig. 29. They were analyzed to give separation values listed in Table 2.

Table 2

List of a-Si bilayer separation values obtained by the fringe analysis

Bilayer region		$L+t=1/\lambda k\Delta k$ (nm)
2	Fig. 29 (b)	160±40
3	Fig. 29 (c)	180±30
4		350±60
5	Fig. 29 (d)	450±60
6	Fig. 29 (e)	640±100
7		600±150
8		850±150
9	Fig. 29 (f)	1100±200

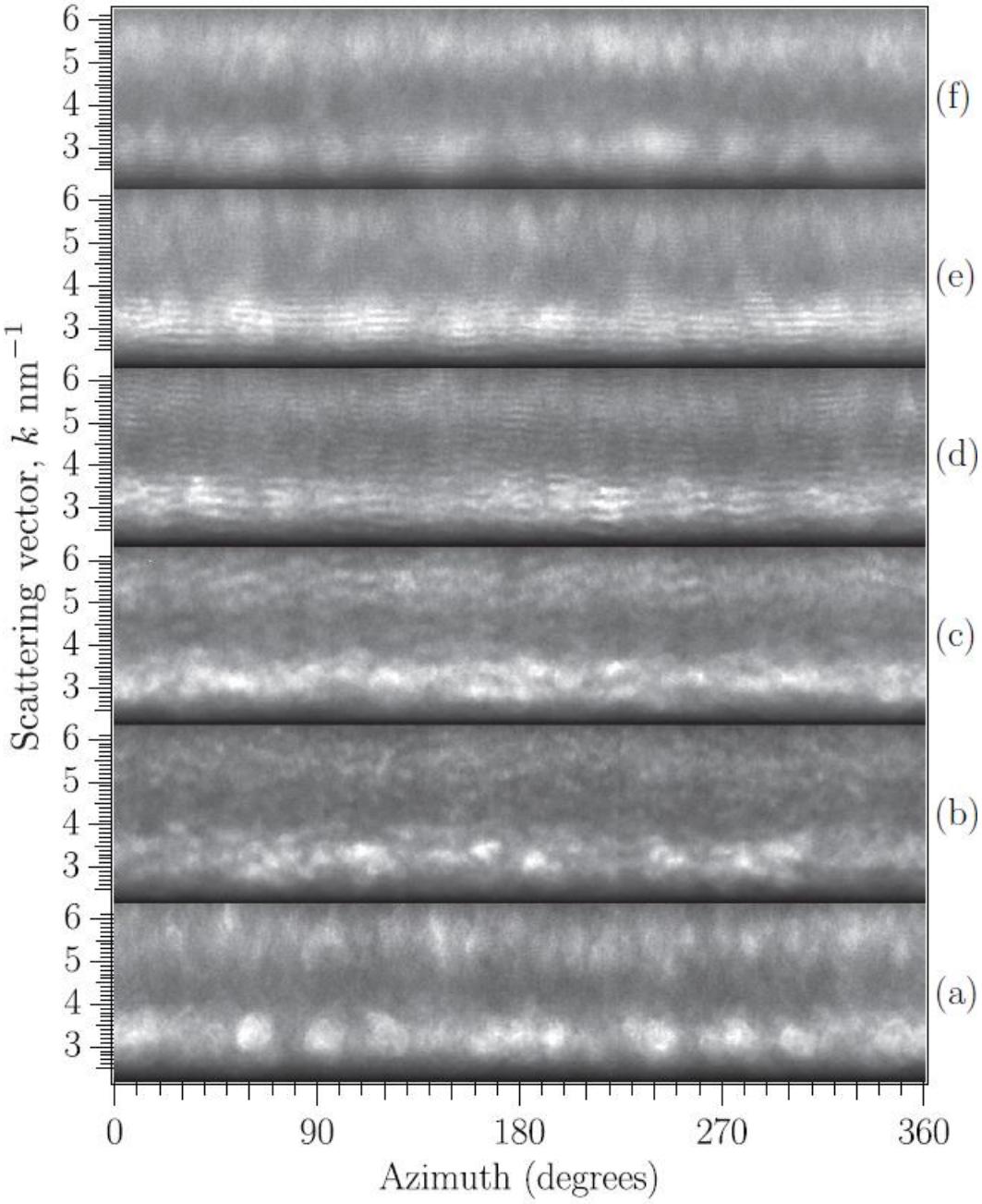

Fig. 29. Unwrapped diffraction patterns for 20-nm thick amorphous Si bilayer. As the gap increases from (a) to (f) the fringes become finer. They are broken and wiggly thought the azimuth crating a picture of "rivulets".

Diffraction patterns for a random, polycrystalline, paracrystalline and CRN models with 300 nm separation were computed, unwrapped and compared to the experimental pattern unwraps of Fig. 29. Fig. 30 illustrates this comparison where the

rightmost is the experimental pattern which visually matched closest the computed set. Its separation, 350 nm, appeared to match the separation of the models within the uncertainty coming both from the accuracy of method to obtain the experimental separation and the subjective matching error. Note that the computed patterns reproduce all features of the experimental pattern, i.e. they show irregular, wavy and broken fringe structure, except they fade and disappear at high *k*.

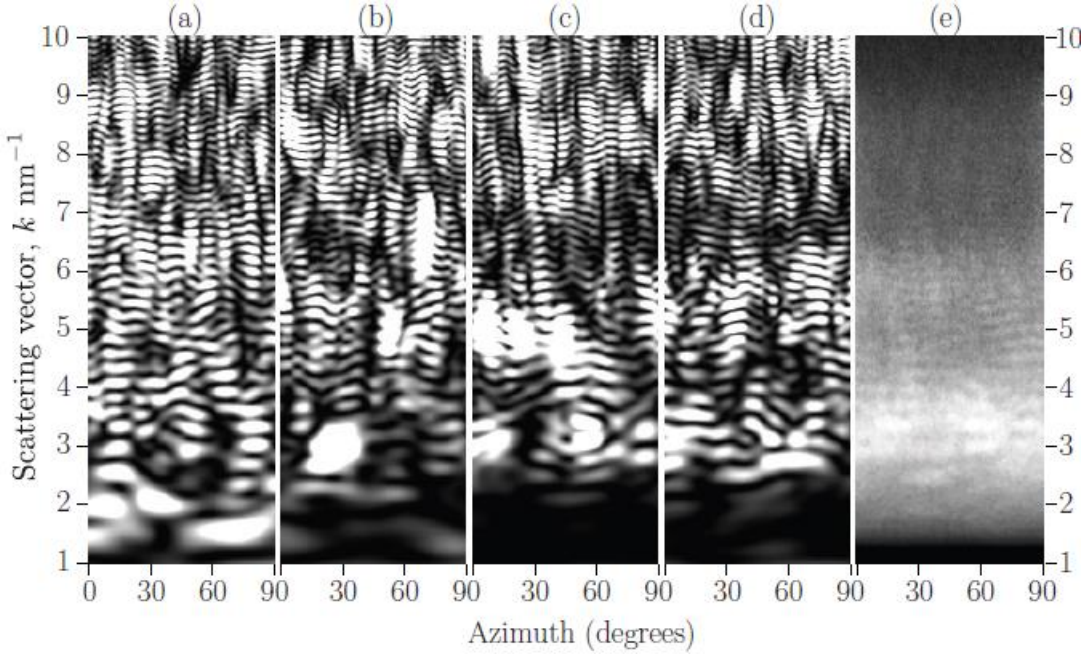

Fig. 30. Set of unwrapped diffraction patterns from different models of bilayer a-Si with 300 nm separation computed by M. Treacy for 200 keV electron probe with 1.5 nm resolution. (a) – Random model. (b) –Polycrystalline model. (c) – Paracrystalline model. (d) – Continuous random network model. (e) – Experimental data, which is a fragment of Fig. 29 (d). Wiggly fringes and "rivulets" of fringes along *k* appear in all models and in the data. Experimentally, fringe contrast fades for $k > 7$ nm^{-1}. Fringe separation for the model with 300 nm gap matches within the error bar with that for the experimental bilayer with about 350 nm gap.

Fig. 31 shows a set of unwrapped a-Si diffraction patterns from the bilayer with increasing gap. The regions 3, 4, 6 and 9 from the Table 2 are sampled. Visually, the fringe contrast within each pattern fades rapidly as wavevector *k* increases. It can be seen that there is a cut-off *k* value (approximately indicated by red lines) beyond which no

fringes are visible. The red lines move towards lower k as the separation increases. Kinematically, the fringe spacing Δk for a given pattern should decrease as k increases while the fringe contrast should remain constant.

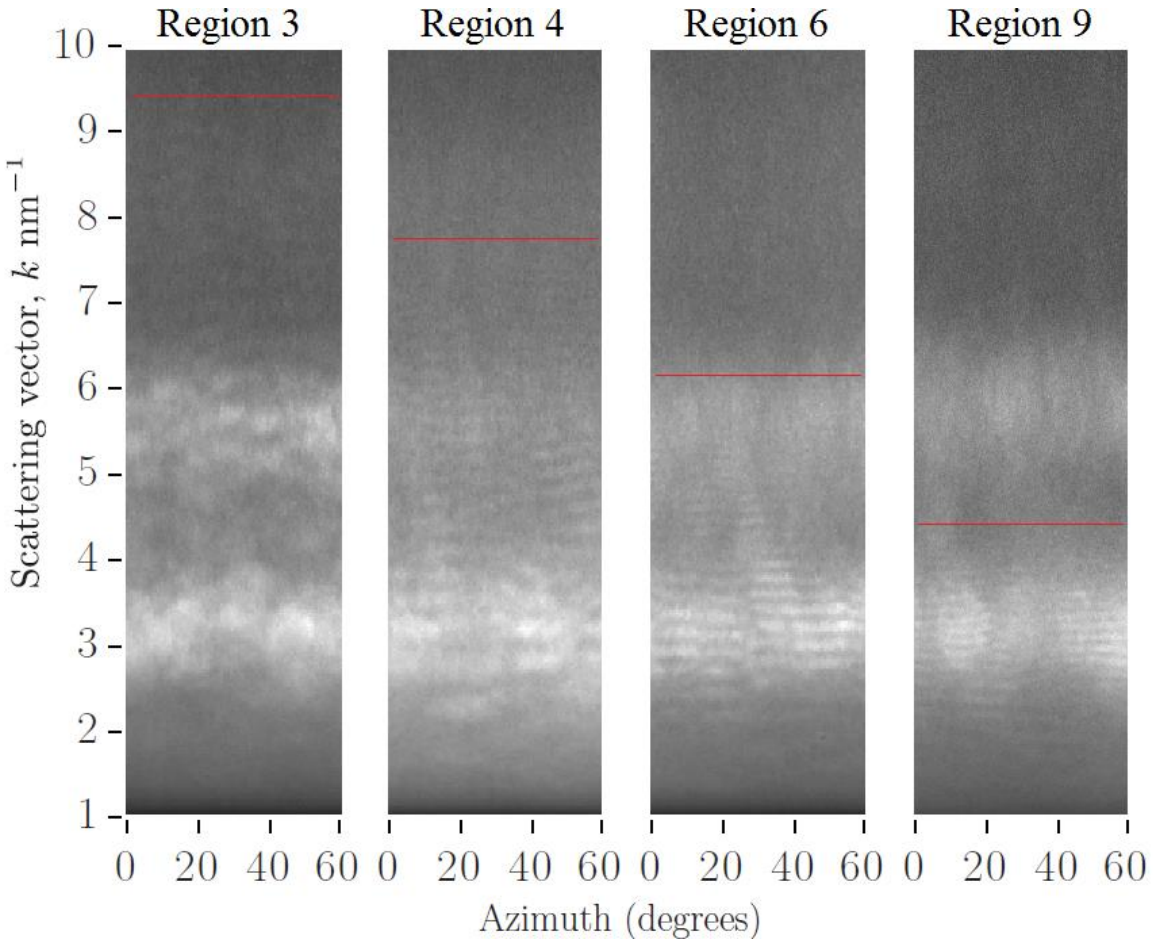

Fig. 31. Set of unwrapped diffraction patterns of bilayer a-Si. Only small fragments are shown corresponding to about 60 degree range of azimuthal angle. The gap increases from left to write. The horizontal red lines show approximate boundaries past which the fringes fade. They move to lower k values as the gap widens. The region numbers 3, 4, 6 and 9 correspond to those in Table 2, and have bilayer separations 180 nm, 350 nm, 640 nm and 1100 nm, respectively.

Fig. 32 shows scatter-plots of the fringe contrast, C,

$$C = \frac{I_{\max} - I_{\min}}{I_{\max} + I_{\min}}, \tag{5.10}$$

versus the scattering vector for the same bilayer regions. Indeed, the contrast decreases both with k and bilayer separation. The latter is seen from the comparison of the plots at about k = 3.2 nm^{-1}, which corresponds to the c-Si 111 reflection. This contrast dependence on the bilayer separation indicates that the waves become mutually incoherent with increasing path difference, which is a consequence of partial temporal coherence.

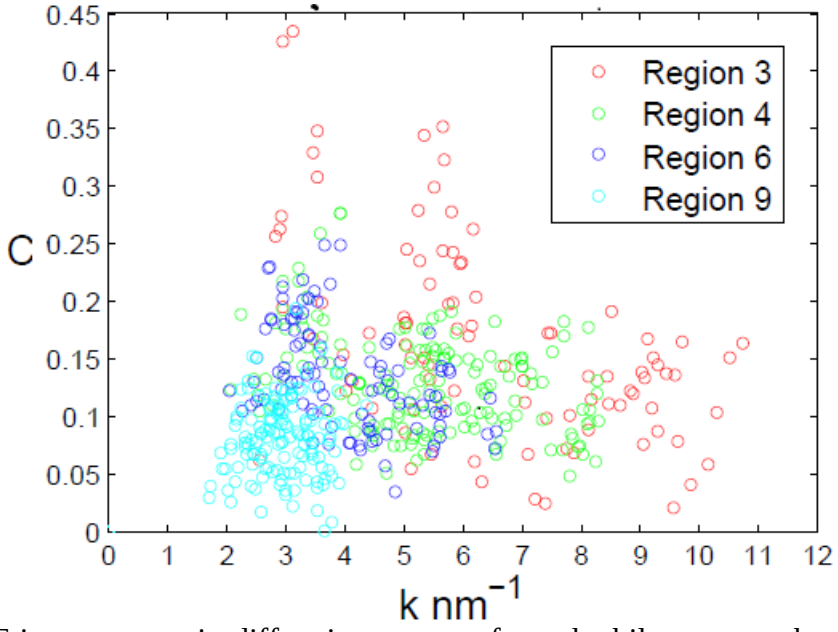

Fig. 32. Fringe contrast in diffraction patterns from the bilayer amorphous silicon. Four regions of the sample with different bilayer separations are presented. The region numbers 3, 4, 6 and 9 correspond to those in Table 2, and have bilayer separations 180 nm, 350 nm, 640 nm and 1100 nm, respectively. The contrast fades at lower k-values with increasing separation. The peaks at characteristic c-Si wavevector values probably arise because the displacement decoherence affects the scattering from the ordered regions less than the disordered matrix.

The temporal coherence length may be estimated most easily for the case of a Gaussian wave, which is a good approximation of the experimental electron probe. For this special case the uncertainty relation looks like $\Delta E \Delta t = \hbar/2$, where ΔE, Δt and $\hbar$ are the energy spread, the time interval and the reduced Plank constant, respectively. There is

a factor of $\sqrt{2}$ difference between the standard deviation of the Gaussian wavefunction and that of the corresponding intensity, so the uncertainty relation turns into $\sigma_E\sigma_t = \hbar$ for wavefunction standard deviations. Inserting $\sigma_t = \sigma_L/v$ and rearranging one gets an estimate of the temporal coherence length $\sigma_L = \hbar v/\sigma_E$, where the wave's group velocity. For 200 keV electrons with 0.85 eV zero-loss peak FWHM spread (Schottky FEG of ASU's the JEOL ARM200F) ΔE = 0.85 eV/2.35=0.36 eV. So $\sigma_E = \Delta E\sqrt{2} = 0.51\,\text{eV}$, σ_L ≈ 270 nm. The effective σ_L, which may further be shortened by inelastic scattering within the sample, can be obtained from the experimental contrast plot (Fig. 32). $\sigma_L \approx 225$ nm was obtained in [204] by fitting the contrast values at k_{111} and k_{220} from $C(k)$ plots corresponding to different bilayer separations L to a Gaussian-related function (see Fig. 33). The fitting function was chosen as result of the following consideration. In the case of full coherence the interference of the reference wave ($\psi_0 = 1$) with the phase-shifted wave ($\psi = \exp(i\varphi)$) gives intensity $I = |1+ \exp(i\varphi)|^2 = 2\cos^2(\varphi/2)$. For partial coherence with attenuation parameter

$$\alpha(L) = \exp\left(-\frac{L^2}{2\sigma_L}\right), \tag{5.11}$$

one gets $I = |1+ \alpha \exp(i\varphi)|^2 = 1 + \alpha^2 + 2\cos^2(\varphi/2)$ instead. Here L is the path difference in the propagation direction, i.e. the bilayer separation. The contrast as a function of the separation is then obtained using (5.10)

$$C(L) = \frac{2\alpha}{1+\alpha^2} \approx 2\alpha\,. \tag{5.12}$$

This is the aforementioned Gaussian-related fitting function with α given by (5.11).

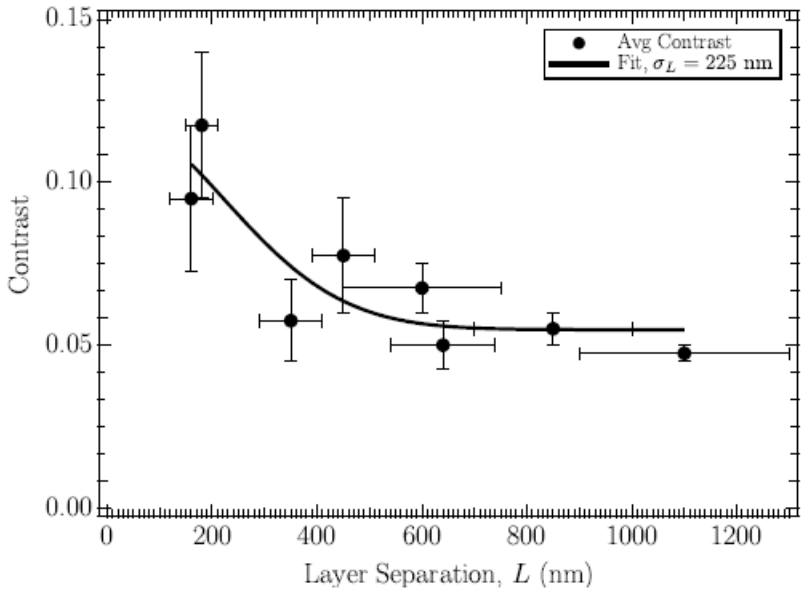

Fig. 33. The mean fringe contrast within the first two peaks (2.8 – 3.6 nm^{-1}, and 5.0 – 6.0 nm^{-1}) as a function of layer separation. The error bars in contrast represent the spread in contrast values about each mean value. The fit is to a Gaussian-related function, returning a standard deviation (effective coherence length) of 225 nm. The constant contrast offset of about 0.05 may be arising because some of the weak fringes that we measure are illusory. (Courtesy of M. Treacy.)

The obtained effective experimental value of the temporal coherence length is close to the value that results from the initial beam energy spread. This allows one to infer that no significant decoherence due to energy-loss events occurred in the sample, and the temporal coherence is mainly limited by the gun energy spread.

On the other hand, the rapid fading of the fringe contrast with *k* within a given pattern evidenced by Fig. 32 indicates that the two interfering waves from each layer become increasingly mutually incoherent as *k* increases. This is not a simple Debye-Waller attenuation as the contrast fades away too rapidly. Clearly, the displacement decoherence, which is significantly stronger than the diffuse scattering, is likely responsible for this.

It can be concluded that the picture observed in Fig. 31 is caused by the combined effect of decoherence and partial temporal coherence. The former is dominated by the

displacement decoherence, while the latter is caused mainly by the source energy spread and may be enhanced in thicker samples by energy-loss processes.

In summary; several attempts were made to study the variance dependence on the sample thickness, each employing a different sample preparation technique. Ostensibly straightforward, the experiment turned out to be impossible to carry out because of adverse experimental conditions and sample preparation artifacts. Unexpectedly, intensity fringes concentric with the diffraction pattern center were noticed in diffraction from the multi-layer amorphous carbon films prepared initially for the variance thickness dependence experiment. The interference phenomena and the fringe features were explained in detail. The separation in the bilayer regions of the sample was estimated from experimental fringe spacings. Finally, the fringes were noticed to fade away rapidly far from the diffraction pattern center, so a fringe contrast analysis was carried out which supported the decoherence argument of Chapter 4.

CHAPTER 6

FLUCTUATION ELECTRON MICROSCOPY OF NITROGEN-DOPED ULTRA NANO-CRYSTALLINE DIAMOND FILMS

6.1. Brief Overview of Ultra Nano-Crystalline Diamond

Diamond films that have been doped with nitrogen are proving to be promising materials for energy conversion applications. The high electric and thermal conductivity and negative electron affinity (NEA) of the hydrogen-terminated nitrogen-doped diamond enables high efficiency in thermionic emission and photoemission [205-208], field emission [209] and secondary electron emission [210]. The use of H-terminated N-doped diamond films enables conversion at temperatures less than 1000K [205]. The H-termination results in NEA of the surface layer [208], i.e. the vacuum level being below the conduction band minimum (CBM). The n-type doping creates donor levels in the diamond's band gap close to the CBM, which considerably lowers the work function. As a result less than 1.5 eV effective work function is obtained and thermionic emission below 600K is reported in a "non-cesiated" convertor [207].

Clearly, the thermionic emission and photoemission characteristics are closely related to the emitter's microstructure. For instance, sp^2 bonds present in UNCD grains are believed to mitigate the upward band bending [205].

6.2. Structural Characterization of UNCD films.

Several UNCD samples were investigated in this study. Unfortunately, more than one of the CVD growth parameters were varied from sample to sample which hindered systematic observation of the resulting microstructure's dependence on those parameters separately. For example, it would be interesting to observe UNCD film's granularity

dependence on the nitrogen doping concentrations only, or film/substrate interface quality on sonication time or growth temperature only.

In order to get some preliminary information about the degree of crystallinity, high-resolution imaging and diffraction was carried out prior to FEM studies. Grain size values were estimated to be in a broad range of 2-30 nm both by low-resolution dark field TEM and high-resolution bright field STEM. Fig. 34 (d) shows an example of the dark-field image from one of the UNCD samples. The low resolution BF TEM image along with the selected area and the diffraction pattern are also presented in Fig. 34 (a), (b) and (c), respectively. The grain structure is best illustrated by high-resolution images of Fig. 35. As seen in the left-side area of the image of Fig. 35 (a), the sample was melted and amorphized by Ga-ion beam treatment during the FIB lift-out TEM sample preparation. An amorphous interlayer of about 1.5 nm is visible between the UNCD and silicon layers.

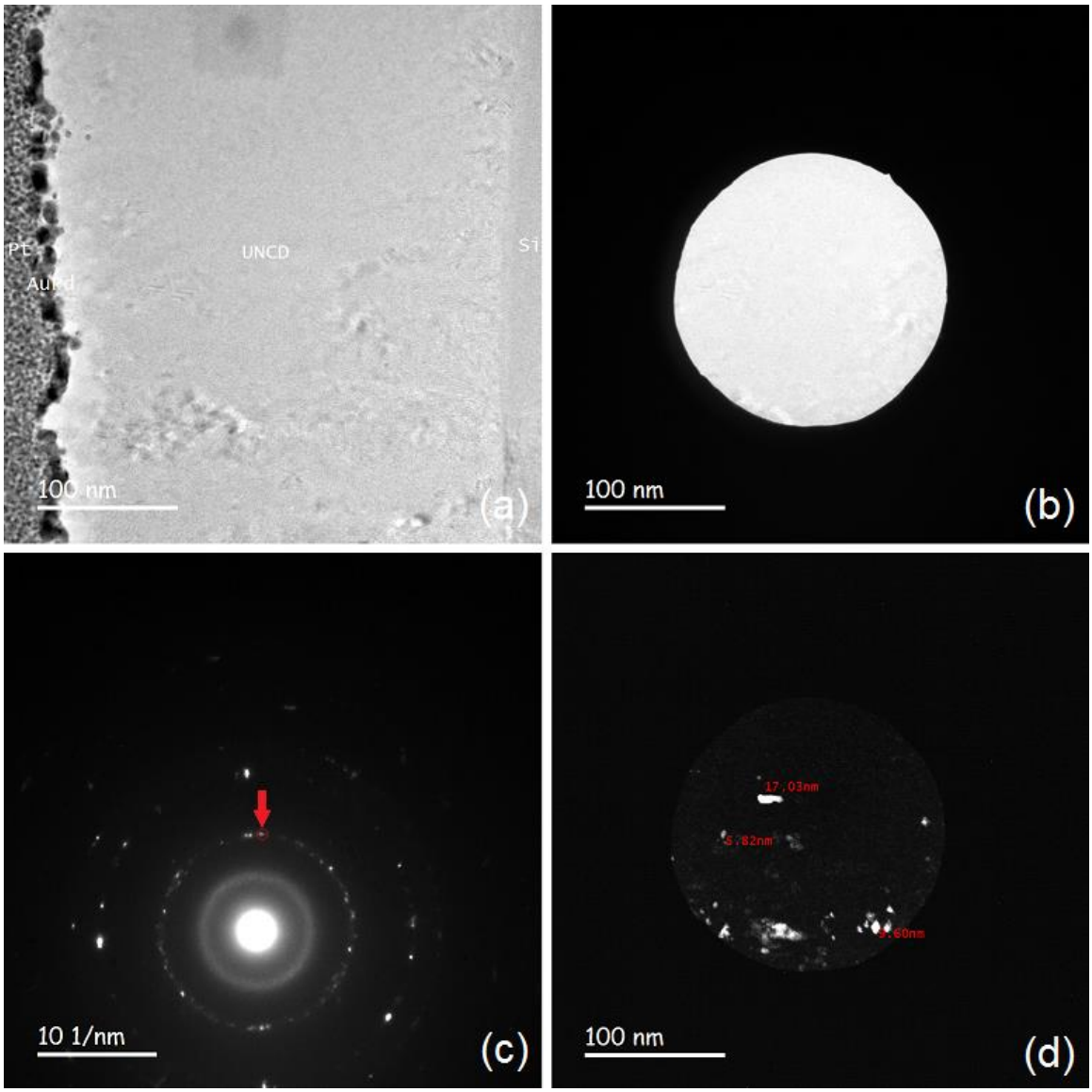

Fig. 34. Dark-field TEM imaging of the UNCD film. (a) – Low-resolution BF TEM image of the cross-sectional UNCD sample. (b) – Area select on the UNCD layer by a selected area aperture. (c) – Selected area diffraction pattern (SADP). The red arrow shows the reflection selected later to form a dark-field image. (d) – Dark-field TEM image of the selected area. Grain sizes are indicated in red.

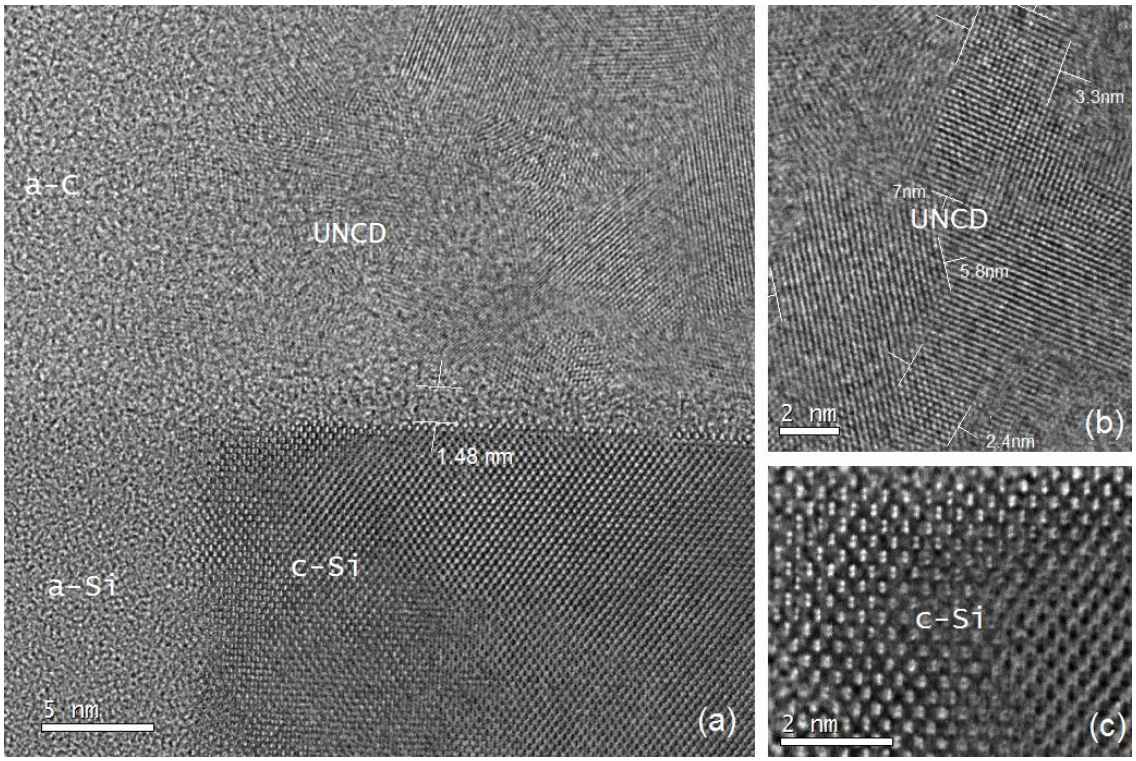

Fig. 35. Aberration corrected BF STEM image of the cross section view of the UNCD film grown on a (100) Si substrate, taken at 200 keV (a) – Area close to the tip of the wedge-shaped sample. Part of the area closer to the tip (i.e. to the left) has been melted by the FIB treatment. UNCD layer is polycrystalline. Thin amorphous layer of about 1.5 nm is formed between the Si and UNCD layers. (b) – Magnified view of the UNCD layer showing the grain structure. (c) – Magnified view of the Si substrate at [110] zone axis with resolved 136 pm dumbbells.

Relative elemental concentrations of C, Si and O were roughly estimated from EELS line-scans across the film-substrate interface, which are shown in Fig. 36 (b). Fig. 36 (a) shows the line-scan location relative to the interface. Concentrations of 69%, 26% and 5% for C, Si and O, respectively, imply that the interlayer can't be a silicon oxidation layer, which is known to form on silicon wafers and is usually about 1-1.5 nm thick [211-213]. This is also supported by the fact that the diamond layer was grown in high-temperature (850°C) hydrogen plasma. The silicon carbide stoichiometry is not satisfied. It is possible that the sonication in diamond the slurry amorphized the Si wafer at the surface, and the subsequent interdiffusion of C and Si formed the observed interlayer.

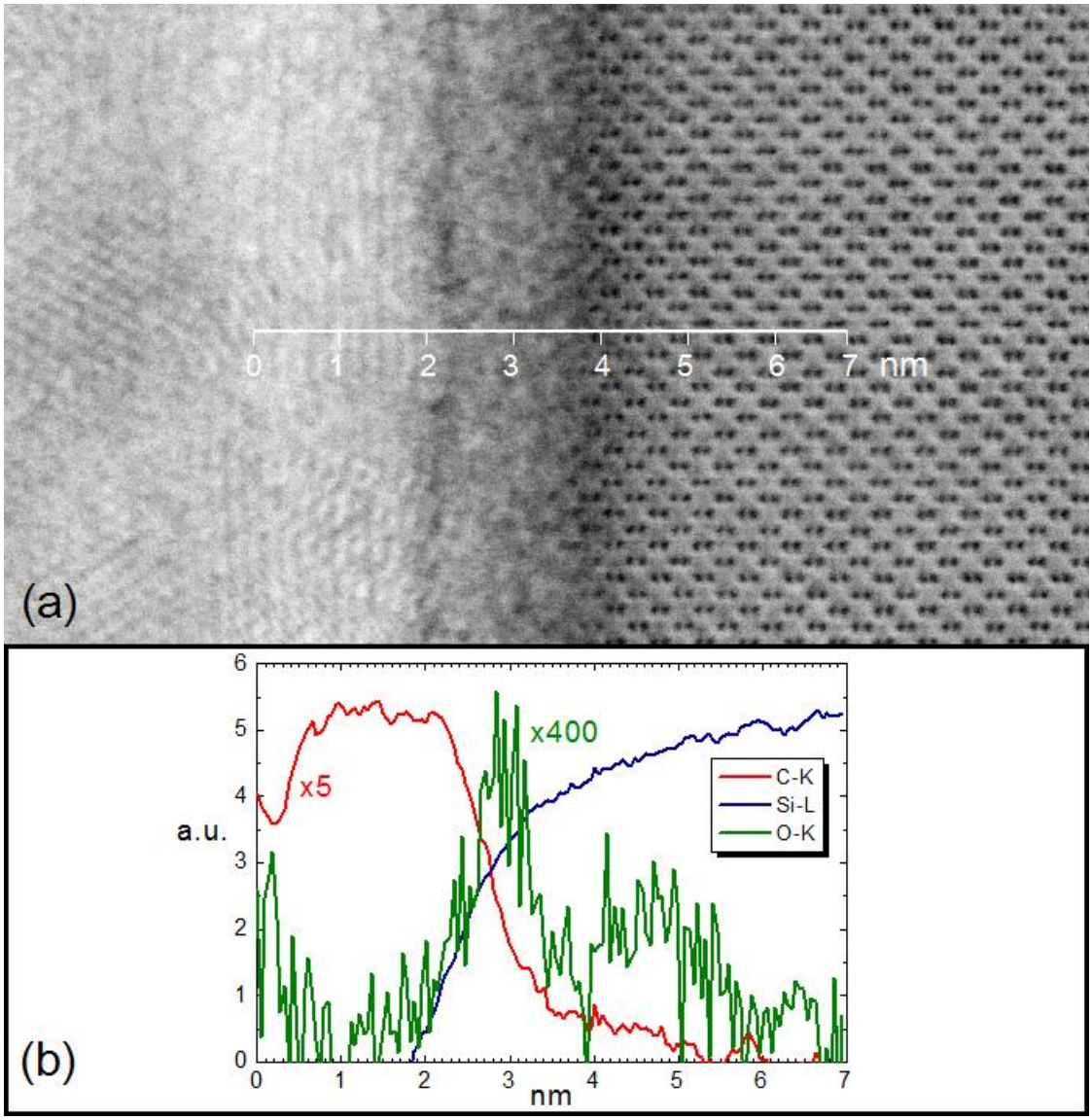

Fig. 36. Chemical analysis of the interlayer between the Si substrate and the UNCD film. (a) – The EELS linescan area on a STEM BF image (not the actual survey image for linescan). The scale mark has the actual scan line length. (b) – Line profiles obtained by a probe of about 0.5 nm of C, Si and O. The relative quantification of the corresponding elements gives about 69%, 26% and 5% respectively.

Although the preliminary investigation showed that the UNCD films are essentially polycrystalline both in high-resolution images and diffraction, and therefore are not interesting candidates for FEM studies, a number of STFEM experiments were conducted in the square areas shown in the low resolution image of Fig. 37 (a). The tip of

the wedge-shaped cross-section sample was amorphized. Fig. 37 (b) is a typical diffraction pattern from that area. The diffraction pattern from a thicker area, which attests its polycrystalline structure, is given in Fig. 37 (c).

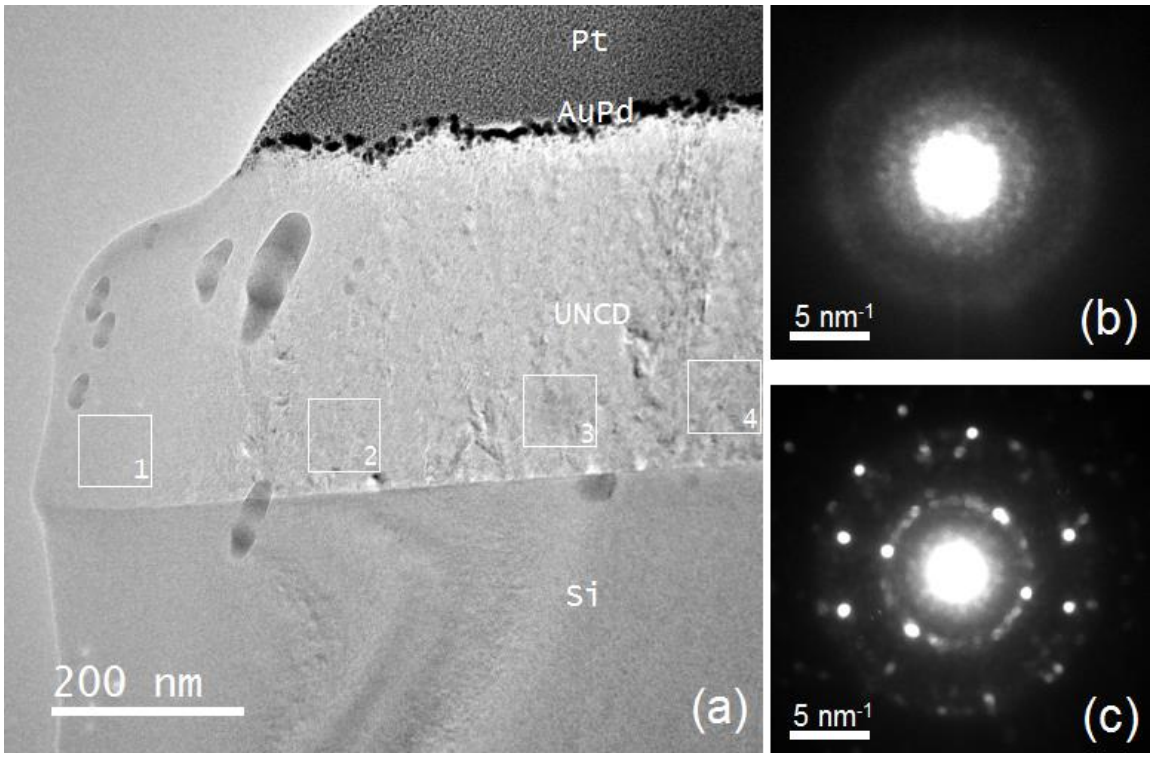

Fig. 37. (a) – TEM image of the FIB-liftout sample consisting of a 100 Si substrate, UNCD layer, AuPd coating layer and Pt layer, taken at 200 keV. White, numbered squares show approximately the area where FEM data was collected. Dark elongated spots on Si and UNCD layers are beam contamination spots. The tip of the sample is partly amorphized by the focused Ga-ion beam during preparation. (b) – Typical diffraction pattern from the amorphized tip area. (c) – Typical diffraction pattern from a thicker area.

Variance plots from the eight areas are shown in Fig. 38. The probe 3 of Table 1 with 1.5 nm resolution and 2.44×10^{8} electrons/($nm^2\times sec$) flux was used. The plots from areas 1 and 5 are similar to the variance plot from the amorphous carbon support film – the green trace of the Fig. 17 (a) – except the peak at about 2.9 nm^{-1}, appeared similar to the stepped amorphous carbon film in Fig. 19. This peak was previously attributed to Ga contamination. However, it may also correspond to graphite 200 reflections (see the next

paragraph), or to both. The rest of the plots show large peaks at the diamond carbon characteristic *k* values as expected for a polycrystalline film. However, the ordering and orientation differences of the grains between the regions may introduce large variance differences, so the variance from the thicker area may appear to be larger than that from a thinner one despite its inverse dependence on thickness. For instance, the 111 peak of Fig. 38 decreases with the increasing thickness from area 2 to area 4, which is consistent with the inverse relationship between variance and thickness, but the opposite is true for the 220 peak. In the latter case the "ordering variance" dominates the "thickness variance".

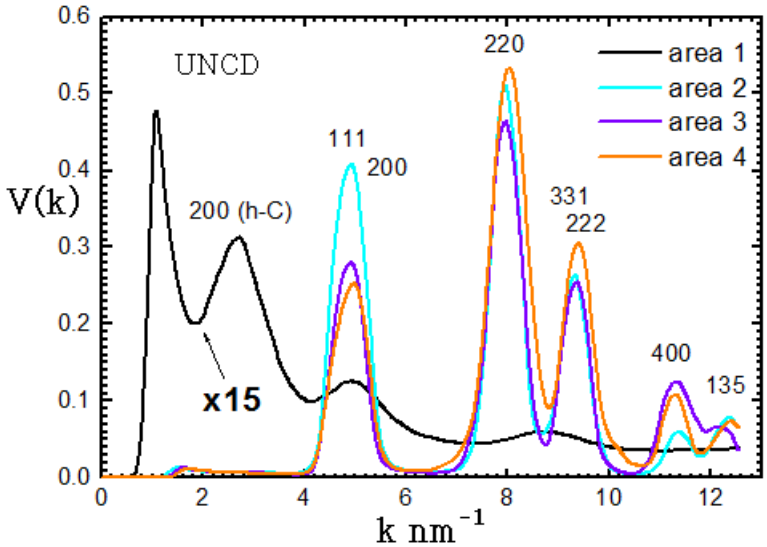

Fig. 38. Normalized variance plots for the UNCD film obtained by 200 keV STFEM using condenser system configuration that gives a 1.5 nm nominal diffraction-limited resolution. Each trace corresponds to one of the square areas indicated in Fig. 37 (a) Exposure time was adjusted to 0.5 sec resulting in about 1.22×10^{8} electrons/nm^{2} fluence. Large diamond peaks are observed in all areas, except at the amorphized tip (1 and 5). The graphite 200 peak is observed at about 2.9 nm in the area 1 along with two diamond peaks.

The amorphous tip of the same UNCD sample was further investigated after additional Ar plasma thinning. Fig. 39 and Fig. 40 show results from different areas of the tip. Note that additional peaks that appear to correspond to hexagonal-carbon

spacings are observed (at about 4.7 nm^{-1}, 5.8 nm^{-1} and 6.5 nm^{-1}) in Fig. 39 in contrast to the black traces of Fig. 38. Supposedly, the graphite is formed after melting of the sample tip, which is observed live during the FIB thinning, and may also occur during plasma thinning. This conclusion is supported by the results of [183], where a large 200 graphite peak, simultaneously with diminished diamond peaks, were observed when annealing diamond-like amorphous carbon, just like in the black trace of the Fig. 38 (b). Our tip was basically annealed by the FIB due to lack of efficient thermal conduction away from the ion beam target (towards the tip). Note that none of the preceding FEM data, from carbon samples that were not treated by FIB or plasma cleaning, show the 200 graphite peak. As mentioned in Chapter 3, the peak at about 7 nm^{-1} in Fig. 40 (b) is a forbidden reflection in graphite but it is allowed in curved, 5-ring rich, carbon allotropes. Although interesting, this peak has never been reproduced in subsequent FEM experiments of disordered carbons. Note that the curved structure although vaguely is visible near the left upper corner of the white square in image Fig. 40 (a).

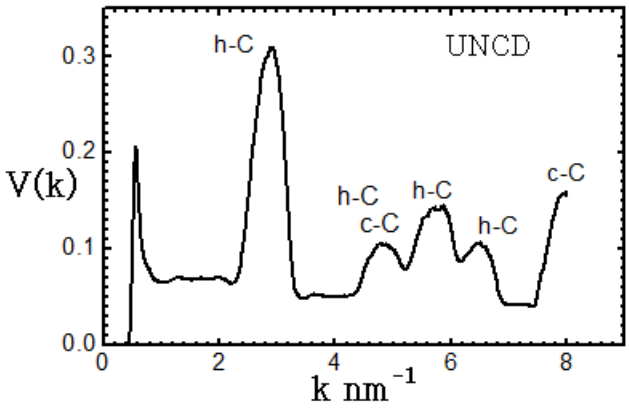

Fig. 39. Normalized variance plot from the UNCD sample. The STFEM data was collected from an 8×8 grid of probe positions with 8 nm step, located at the tip of the cross sectional FIB-liftout sample, which was amorphized by the FIB and Ar plasma thinning. Exposure time was adjusted to 1 sec resulting in about 2.44×10^{8} electrons/nm^2 fluence. Both cubic and hexagonal carbon peaks are present.

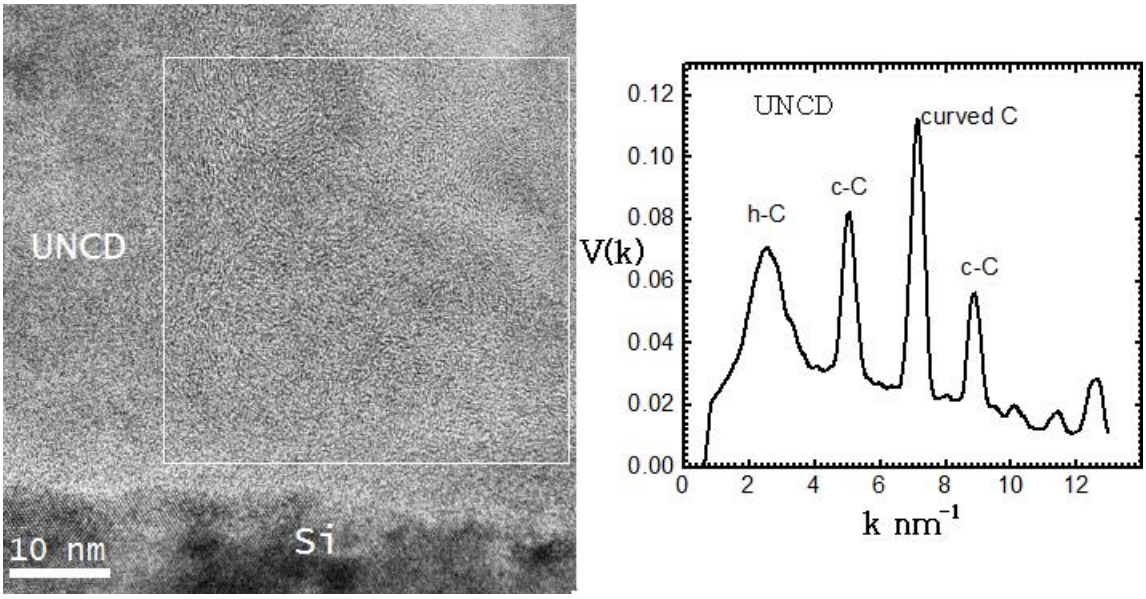

Fig. 40. (a) – High-resolution TEM image of the UNCD layer at the amorphized tip after additional Ar plasma thinning, taken at 200 keV. The white square shows the area in which FEM data was collected. (b) – Normalized variance plot showing both cubic and hexagonal carbon peaks as well as the peak at 7.1 nm^{-1} which is a signature of the curved carbon allotropes. STFEM data was collected from a 5×5 grid of probe positions with 8 nm step. Exposure time was adjusted to 0.2 sec resulting in about 0.49×10^{8} electrons/nm^2 fluence.

6.3. Decoherence in STFEM Explored Through Electron Dose Variation on UNCD Films

The extent of disorder in the diamond layers may be an important factor altering the emitter performance. Conventional imaging and diffraction techniques are not sensitive to MRO, especially at the 1 to 2 nm lengthscales. For this reason it was thought initially that FEM characterization of the UNCD samples described in this study will be useful, in particular, in the regions of the film that look amorphous on TEM images. However, according to the structural analysis of the UNCD films described above one can conclude that the amorphous regions appear only at thin areas and are TEM sample preparation artefacts. Areas representative of the as-deposited UNCD appeared not to be disordered enough to be interesting for FEM.

Nevertheless, FEM of UNCD samples appeared to be useful for investigation of the electron dose dependence of decoherence. This is enabled by the fact that in polycrystalline samples much intensity is scattered at particular *k* values, so it is reasonable to neglect the noise effects on variance, which are otherwise pronounced at low exposure times. Thus, the changes in variance at characteristic *k* values (sharp peaks) between different exposure times can be attributed solely to the electron fluence received by the probed area, especially at the smallest characteristic *k* values (i.e. the 111 peak) and short exposure times. Fig. 41 shows variance plots for FEM data collected from the same area using the probe 4 of Table 1 at three different exposure durations. The strongest variance peaks occur for the shortest exposure time of 0.01 sec for individual diffraction patterns. The variance peaks at about 111 and 220 cubic diamond reflections decrease as the exposure increases. This is because longer exposures result in larger number of decoherence events which suppress the variance as discussed in Chapter 4.

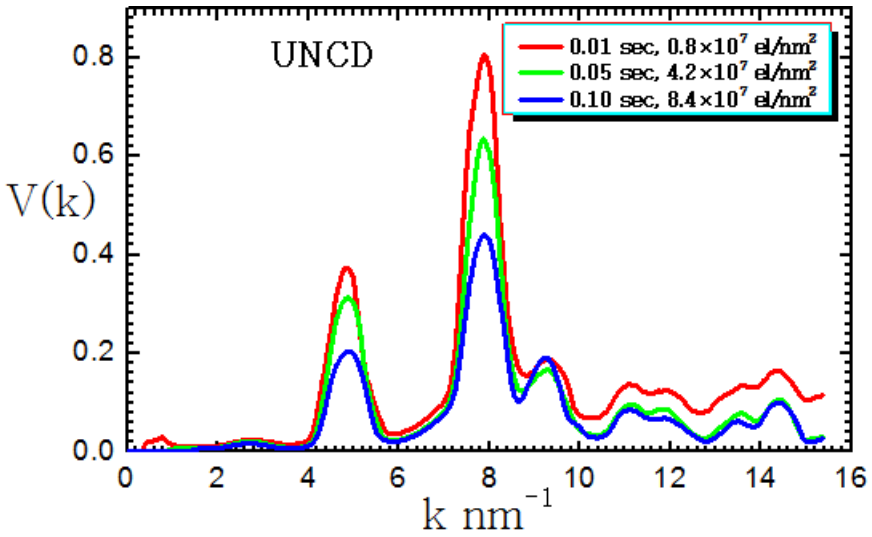

Fig. 41. Experimental STFEM normalized variance plots for about 60 nm thick UNCD film area obtained at 80 keV. The probe 4 configuration of the condenser system provided about 2 nm resolution and 0.84×10^9 electrons/(nm$^2\times$sec). Strong variance peaks arise at the cubic diamond reflections, 111, 220, etc. Variance peaks are suppressed more with longer exposure in accordance with the decoherence argument.

Similar plots were obtained for amorphous samples (a-C, a-Si and a-Si_3N_4), however, it was impossible to separate the effects of decoherence and shot-noise on the FEM data variance since both result in its decrease at longer exposure times, especially at high-*k* values. An example is presented in Fig. 42.

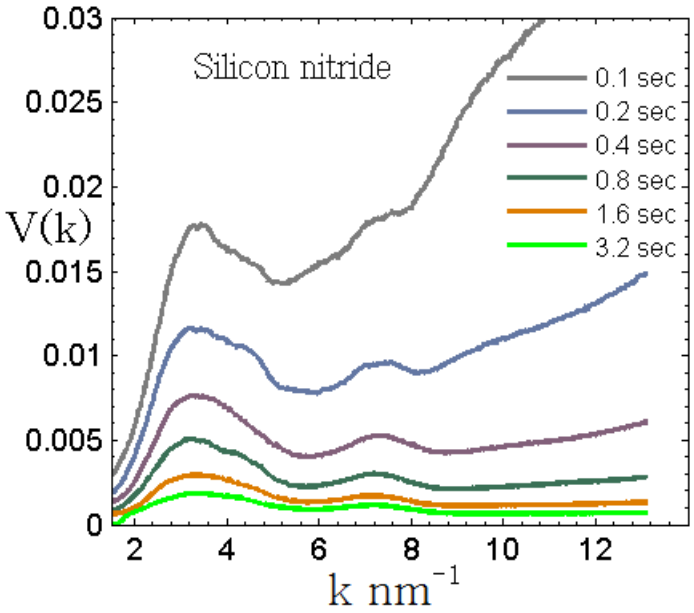

Fig. 42. Experimental STFEM normalized variance plots for 50-nm thick amorphous Si_3N_4 film obtained at 200 keV. The probe 3 configuration of the condenser system provided about 1.5 nm resolution and 2.44×10^8 electrons/(nm^2×sec). Low exposure time variance is dominated by shot noise.

In summary; high-resolution imaging and diffraction of UNCD was carried out prior to FEM characterization, in order to get some preliminary information about the degree of crystallinity. Unfortunately, the observed polycrystalline structure of UNCD films made impossible the study of variance dependence on the sample thickness. On the other hand, the polycrystallinity enabled the study of variance dependence on the electron beam fluence, which supported the decoherence argument about the discrepancy between experimental and computed variance.

CHAPTER 7

CONCLUSION

A series of tilted dark-field FEM data from amorphous carbon was analyzed. It was confirmed that despite the use of a coherent electron source the experimental normalized variance is at least an order of magnitude smaller than that predicted by kinematical scattering theory. Decoherence during scattering was proposed as a mechanism to explain this discrepancy. It was realized that it mimics the effect of the partial spatial coherence of illumination, which known to affect the variance. In fact, one of the original modes of FEM was referred to as Variable Coherence FEM.

In order to explore various mechanisms of decoherence, the experimental variance from amorphous silicon was compared to the results from modeling of diffuse scattering, knock-on displacements, energy loss events, partial illumination coherence and multiple scattering. It was found that the partial spatial coherence of the illumination results in variance suppression at all k. The inelastic scattering also results in uniform suppression but only peaks are affected. Multiple scattering does not affect the variance unless the illumination is partially coherent, or if decoherence is occurring. Atomic displacements, presumably caused by the electron beam interaction with the sample, turned out to emulate experimental variance suppression best.

Although the simulations suggest that atomic displacements by the beam are the primary cause of decoherence, the actual picture is probably far more complicated than in the simple model where displacements with unrealistically large amplitudes occur, which exceed half the silicon bond length. What is clear is that the sample is not static under the electron beam bombardment and an averaged signal from this structural motion is

recorded during the exposure times of individual diffraction patterns. A more realistic picture is possible where the sample constantly rearranges by local small-angle tilts in response to the structural disruptions introduced by the electron impact. It is also possible that such collective tilts of small regions result in a bigger picture of long-range, continuous, flexural rearrangements of the structure. This is consistent with the twinkling that is observed in diffraction patterns as the small-angle tilts are capable of altering the Bragg conditions for the tilting regions.

An interesting conclusion results from the simulation decoherence in the CRN model for amorphous silicon. The displacement decoherence introduces characteristic variance peaks at the positions corresponding to the cubic diamond topology. A possible explanation is that there is more medium-range order present in the CRN model than was previously thought, and the shrinking of the coherence volume, due to decoherence in the sample, in effect suppresses speckle from the long-range random atomic alignments.

Several STEFEM experiments were designed and implemented in order to explore decoherence. Perfectly consistent with the latter, a suppression of the experimental variance was observed with increasing electron beam energy, which was switched between 80 keV and 200 keV in order to alter the extent of the electron beam impact on amorphous carbon and silicon samples.

Another important result reinforcing the decoherence argument came out of the FEM studies of the UNCD samples. The suppression of variance with increasing exposure time is perfectly consistent with decoherence as the accumulation of atomic displacement events during the exposure is expected to decrease the diffraction speckle

sharpness. Further, these results confirm that decoherence is not limited to amorphous structures.

An interferometric diffraction experiment was conducted as a sidetrack of another experiment, which was designed to explore decoherence. Bilayer amorphous carbon and silicon films were prepared using a unique sample preparation technique developed in this study. The interference fringes, which are intensity variations due to reciprocal space modulations in the beam direction sampled by the Ewald sphere, arise in diffraction patterns because of the bilayer shape factor of the sample. The fringes and their appearance were explained in detail. In particular, it was noted that they fade away at smaller k values for larger bilayer separations. This was explained in terms of the partial temporal coherence of the source and the displacement decoherence.

It is clear that decoherence will be a persisting issue for any *quantitative* electron diffraction or imaging study. Ptychography employs phase retrieval algorithms to process diffraction data, that is collected similarly to STFEM but, with highly overlapping probe positions [214]. It is done routinely in the X-ray or optical versions [215]. Although electron ptychography studies were reported to work recently, they employ a low-energy SEM source [216-218]. Along with accurate probe positioning and drift issues, which are claimed to be the current limitation of the electron version of the technique [219], decoherence is undoubtedly another factor hampering ptychographical studies at higher-energies.

REFERENCES

1. R.W. Gundlach, *Xerography from the Beginning.* Journal of Electrostatics, 1989. **24**: p. 3-9.

2. J. Mort, *The Anatomy of Xerography: Its Invention and Evolution*. 1989, Jefferson, NC: McFarland.

3. S.O. Kasap, M.Z. Kabir, and J.A. Rowlands, *Recent Advances in X-Ray Photoconductors for Direct Conversion X-Ray Image Detectors.* Current Applied Physics, 2006. **6**(3): p. 288-292.

4. S. Kasap, J.B. Frey, G. Belev, O. Tousignant, H. Mani, J. Greenspan, L. Laperriere, O. Bubon, A. Reznik, G. DeCrescenzo, K.S. Karim, and J.A. Rowlands, *Amorphous and Polycrystalline Photoconductors for Direct Conversion Flat Panel X-Ray Image Sensors.* Sensors, 2011. **11**(5): p. 5112-5157.

5. S.R. Ovshinsky, *Reversible Electrical Switching Phenomena in Disordered Structures.* Physical Review Letters, 1968. **21**(20): p. 1450-1453.

6. S.R. Ovshinsky, *Amorphous and Disordered Materials – the Basis of New Industries. Materials Research Society.* Materials Research Society Proceedings, 1998. **554**: p. 339.

7. D. Strand, *Ovonics: From Science to Products.* Journal of Optoelectronics and Advanced Materials, 2005. **4**: p. 1679 – 1690.

8. R.E. Simpson, M. Krbal, P. Fons, A.V. Kolobov, J. Tominaga, T. Uruga, and H. Tanida, *Toward the Ultimate Limit of Phase Change in $Ge_2sb_2te_5$.* Nano Letters, 2010. **10**(2): p. 414-419.

9. S. Raoux, D. Ielmini, M. Wuttig, and I. Karpov, *Phase-Change Materials.* Materials Research Society Bulletin, 2012. **37**: p. 118 – 123.

10. A. Gyanathan and Y.-C. Yeo, *Phase-Change Random Access Memory with Multilevel Resistances Implemented Using a Dual Phase-Change Material Stack.* IEEE Transactions on Electron Devices, 2012. **37**: p. 118 – 123.

11. J. Lee, A. Urban, X. Li, D. Su, G. Hautier, and G. Ceder, *Unlocking the Potential of Cation-Disordered Oxides for Rechargeable Lithium Batteries.* Science, 2014. **343**(6170): p. 519-522.

12. S.C. Han, P.S. Lee, J.Y. Lee, J.Y. Lee, A. Züttel, and L. Schwabach, *Effects of Ti on the Cycle Life of Amorphous Mgni-Based Alloy Prepared by Ball Milling.* Journal of Alloys and Compounds, 2000. **306**: p. 219 – 226.

13. M.A. Fetcenko, S.R. Ovshinsky, B. Reichman, K. Young, C. Fierro, J. Koch, A. Zallen, W. Mays, and T. Ouchi, *Recent Advances in Nimh Battery Technology.* Journal of Power Sources, 2007. **165**(2): p. 544-551.

14. C. Iwakura, S. Nohara, S.G. Zhang, and H. Inoue, *Hydriding and Dehydriding Characteristics of an Amorphous Mg_2ni–Ni Composite.* Journal of Alloys and Compounds, 1999. **285**: p. 246 – 249.

15. R.M. de Vos, *High-Selectivity, High-Flux Silica Membranes for Gas Separation.* Science, 1998. **279**(5357): p. 1710-1711.

16. M.D. Dolan, N.C. Dave, A.Y. Ilyushechkin, L.D. Morpeth, and K.G. McLennan, *Composition and Operation of Hydrogen-Selective Amorphous Alloy Membranes.* Journal of Membrane Science, 2006. **285**(1-2): p. 30-55.

17. Y. Iwamoto, K. Sato, T. Kato, T. Inada, and Y. Kubo, *A Hydrogen-Permselective Amorphous Silica Membrane Derived from Polysilazane.* Journal of the European Ceramic Society, 2005. **25**(2-3): p. 257-264.

18. H.R. Lee, T. Shibata, M. Kanezashi, T. Mizumo, J. Ohshita, and T. Tsuru, *Pore-Size-Controlled Silica Membranes with Disiloxane Alkoxides for Gas Separation.* Journal of Membrane Science, 2011. **383**(1-2): p. 152-158.

19. Y.S. Lin, *Microporous and Dense Inorganic Membranes Current: Status and Prospective.* Separation and Purification Technology, 2001. **25**: p. 39–55.

20. T. Nagano, S. Fujisaki, K. Sato, K. Hataya, Y. Iwamoto, M. Nomura, and S.-I. Nakao, *Relationship between the Mesoporous Intermediate Layer Structure and the Gas Permeation Property of an Amorphous Silica Membrane Synthesized by Counter Diffusion Chemical Vapor Deposition.* Journal of the American Ceramic Society, 2008. **91**(1): p. 71–76

21. T. Nagano and K. Sato, *Degradation Mechanism of an H2-Permselective Amorphous Silica Membrane.* Journal of Materials Science, 2014. **49**(11): p. 4115-4120.

22. S.M. Saufi and A.F. Ismail, *Fabrication of Carbon Membranes for Gas Separation—a Review.* Carbon, 2004. **42**(2): p. 241-259.

23. J.K. Haleblian, *Characterization of Habits and Crystalline Modification of Solids and Their Pharmaceutical Applications.* Journal of Pharmaceutical Sciences, 1975. **64**: p. 1269 – 1288.

24. B. Shah, V.K. Kakumanu, and A.K. Bansal, *Analytical Techniques for Quantification of Amorphous/Crystalline Phases in Pharmaceutical Solids.* Journal of Pharmaceutical Sciences, 2006. **95**(8): p. 1641-1665.

25. A.J. Aguiar and J.E. Zelmer, *Dissolution Behavior of Polymorphs of Chloramphenicol Palmitate and Mefenamic Acid.* Journal of Pharmaceutical Sciences, 1969. **58**: p. 983 – 987.

26. B.C. Hancock and M. Parks, *What Is the True Solubility Advantage for Amorphous Pharmaceuticals?* Pharmaceutical Research, 2000. **17**: p. 397 – 404.

27. A.A. Elamin, C. Ahlneck, G. Alderborn, and C. Nyström, *Increased Metastable Solubility of Milled Griseofulvin.* International Journal of Pharmaceutics, 1994. **111**: p. 159 – 170.

28. A.R. Brás, E.G. Merino, P.D. Neves, I.M. Fonseca, M. Dionísio, A. Schönhals, and N.l.T. Correia, *Amorphous Ibuprofen Confined in Nanostructured Silica Materials: A Dynamical Approach.* The Journal of Physical Chemistry C, 2011. **115**(11): p. 4616-4623.

29. P. Kinnari, E. Makila, T. Heikkila, J. Salonen, J. Hirvonen, and H.A. Santos, *Comparison of Mesoporous Silicon and Non-Ordered Mesoporous Silica Materials as Drug Carriers for Itraconazole.* International Journal of Pharmaceutics, 2011. **414**(1-2): p. 148-156.

30. D. Singhal and W. Curatolo, *Drug Polymorphism and Dosage Form Design: A Practical Perspective.* Advanced Drug Delivery Reviews, 2004. **56**(3): p. 335-347.

31. G.G. Zhang, D. Law, E.A. Schmitt, and Y. Qiu, *Phase Transformation Considerations During Process Development and Manufacture of Solid Oral Dosage Forms.* Advanced Drug Delivery Reviews, 2004. **56**(3): p. 371-390.

32. W.J.Weber, A. Navrotsky, S. Stefanovsky, E.R. Vance, and E. Vernaz, *Materials Science of High-Level Nuclear Waste Immobilization.* Materials Research Society Bulletin, 2009. **36**: p. 46-53.

33. M.I. Ojovan and W.E. Lee, *Glassy Wasteforms for Nuclear Waste Immobilization.* Metallurgical and Materials Transactions A, 2010. **42**(4): p. 837-851.

34. W.E. Lee, M. Gilbert, S.T. Murphy, R.W. Grimes, and D.J. Green, *Opportunities for Advanced Ceramics and Composites in the Nuclear Sector.* Journal of the American Ceramic Society, 2013. **96**(7): p. 2005-2030.

35. R.C. Ewing, *Nuclear Waste Forms for Actinides.* Proceedings of the National Academy of Sciences, 1999. **96**: p. 3432–3439.

36. J.V. Crum, L. Turo, B. Riley, M. Tang, A. Kossoy, and C. Jantzen, *Multi-Phase Glass-Ceramics as a Waste Form for Combined Fission Products: Alkalis, Alkaline Earths, Lanthanides, and Transition Metals.* Journal of the American Ceramic Society, 2012. **95**(4): p. 1297-1303.

37. V. Bernardet, S. Gomes, S. Delpeux, M. Dubois, K. Guérin, D. Avignant, G. Renaudin, and L. Duclaux, *Protection of Nuclear Graphite toward Fluoride Molten Salt by Glassy Carbon Deposit.* Journal of Nuclear Materials, 2009. **384**(3): p. 292-302.

38. J. Blink, J. Farmer, J. Choi, and C. Saw, *Applications in the Nuclear Industry for Thermal Spray Amorphous Metal and Ceramic Coatings.* Metallurgical and Materials Transactions A, 2009. **40**(6): p. 1344-1354.

39. W. Klement, R.H. Willens, and P. Duwez, *Non-Crystalline Structure in Solidified Gold–Silicon Alloys.* Nature, 1960. **187**: p. 869 – 870.

40. M. Ashby and A. Greer, *Metallic Glasses as Structural Materials.* Scripta Materialia, 2006. **54**(3): p. 321-326.

41. A.L. Greer, *Metallic Glasses.* Science, New Series, 1995. **267**: p. 1947 – 1953.

42. A. Takeuchi and A. Inoue, *Classification of Bulk Metallic Glasses by Atomic Size Difference, Heat of Mixing and Period of Constituent Elements and Its Application to Characterization of the Main Alloying Element.* Materials Transactions, 2005. **46**: p. 2817 – 2829.

43. T. Bitoh, A. Makino, A. Inoue, and A.L. Greer, *Large Bulk Soft Magnetic* $[(Fe_{0.5}co_{0.5})_{0.75}b_{0.2}si_{0.05}]_{96}nb_4$ *Glassy Alloy Prepared by* B_2o_3 *Flux Melting and Water Quenching.* Applied Physics Letters, 2006. **88**(18): p. 182510.

44. C. Suryanarayana and A. Inoue, *Iron-Based Bulk Metallic Glasses.* International Materials Reviews, 2013. **58**(3): p. 131-166.

45. M.M. Trexler and N.N. Thadhani, *Mechanical Properties of Bulk Metallic Glasses.* Progress in Materials Science, 2010. **55**(8): p. 759-839.

46. J. Schroers, T. Nguyen, S. O'Keeffe, and A. Desai, *Thermoplastic Forming of Bulk Metallic Glass—Applications for Mems and Microstructure Fabrication.* Materials Science and Engineering: A, 2007. **449-451**: p. 898-902.

47. Y. Yokoyama, Y. Akeno, T. Yamasaki, P.K. Liaw, R.A. Buchanan, and A. Inoue, *Evolution of Mechanical Properties of Cast* Zr_{50} Cu_{40} Al_{10} *Glassy Alloys by Structural Relaxation.* Materials Transactions, 2005. **46**: p. 2755 – 2761.

48. J. Xu, U. Ramamurty, and E. Ma, *The Fracture Toughness of Bulk Metallic Glasses.* JOM, 2010. **62**: p. 10 – 18.

49. G. Kumar, A. Desai, and J. Schroers, *Bulk Metallic Glass: The Smaller the Better.* Advanced Materials, 2011. **23**(4): p. 461-476.

50. W.H. Wang, C. Dong, and C.H. Shek, *Bulk Metallic Glasses.* Materials Science and Engineering R, 2004. **44**(2-3): p. 45-89.

51. A. Inoue and N. Nishiyama, *New Bulk Metallic Glasses for Applications as Magnetic-Sensing, Chemical, and Structural Materials.* Materials Research Society Bulletin, 2007. **32**: p. 651 – 658.

52. M. Davidson, S. Roberts, G. Castro, R.P. Dillon, A. Kunz, H. Kozachkov, M.D. Demetriou, W.L. Johnson, S. Nutt, and D.C. Hofmann, *Investigating Amorphous Metal Composite Architectures as Spacecraft Shielding.* Advanced Engineering Materials, 2013. **15**: p. 27 – 33.

53. G. Kumar, H.X. Tang, and J. Schroers, *Nanomoulding with Amorphous Metals.* Nature, 2009. **457**(7231): p. 868-872.

54. M. Carmo, R.C. Sekol, S. Ding, G. Kumar, J. Schroers, and A.D. Taylor, *Bulk Metallic Glass Nanowire Architecture for Electrochemical Applications.* ACS Nano, 2011. **5**: p. 2979–2983.

55. J. Schroers, G. Kumar, T.M. Hodges, S. Chan, and T.R. Kyriakides, *Bulk Metallic Glasses for Biomedical Applications.* JOM, 2009. **61**(9): p. 21-29.

56. L. Huang, D. Qiao, B.A. Green, P.K. Liaw, J. Wang, S. Pang, and T. Zhang, *Bio-Corrosion Study on Zirconium-Based Bulk-Metallic Glasses.* Intermetallics, 2009. **17**(4): p. 195-199.

57. S. Buzzi, K. Jin, P.J. Uggowitzer, S. Tosatti, I. Gerber, and J.F. Löffler, *Cytotoxicity of Zr-Based Bulk Metallic Glasses.* Intermetallics, 2006. **14**(7): p. 729-734.

58. K. Imai and S. Hiromoto, *In Vivo Evaluation of Zr-Based Bulk Metallic Glass Alloy Intramedullary Nails in Rat Femora.* Journal of Materials Science: Materials in Medicine, 2014. **25**(3): p. 759-768.

59. Y.B. Wang, X.H. Xie, H.F. Li, X.L. Wang, M.Z. Zhao, E.W. Zhang, Y.J. Bai, Y.F. Zheng, and L. Qin, *Biodegradable Camgzn Bulk Metallic Glass for Potential Skeletal Application.* Acta Biomaterialia, 2011. **7**(8): p. 3196-3208.

60. J.D. Cao, N.T. Kirkland, K.J. Laws, N. Birbilis, and M. Ferry, *Ca-Mg-Zn Bulk Metallic Glasses as Bioresorbable Metals.* Acta Biomaterialia, 2012. **8**(6): p. 2375-2383.

61. Y.-S. Sun, W. Zhang, W. Kai, P.K. Liaw, and H.-H. Huang, *Evaluation of Ni-Free Zr–Cu–Fe–Al Bulk Metallic Glass for Biomedical Implant Applications.* Journal of Alloys and Compounds, 2014. **586**: p. S539-S543.

62. G. Xie, F. Qin, S. Zhu, and A. Inoue, *Ni-Free Ti-Based Bulk Metallic Glass with Potential for Biomedical Applications Produced by Spark Plasma Sintering.* Intermetallics, 2012. **29**: p. 99-103.

63. H. Choi-Yim and W.L. Johnson, *Bulk Metallic Glass Matrix Composites.* Applied Physics Letters, 1997. **71**(26): p. 3808.

64. F. Barbir, *Pem Fuel Cells - Theory and Practice, 2nd Ed.*, 2013, Elsevier.

65. A. Kawashima, H. Habazaki, K. Asami, and K. Hashimoto, *Amorphous Alloy Electrodes for Fuel Cells.* Science Reports of the Research Institutes, Tohoku University A, 1996. **42**: p. 91 – 98.

66. J. Jayaraj, Y.C. Kim, K.B. Kim, H.K. Seok, and E. Fleury, *Corrosion Studies on Fe-Based Amorphous Alloys in Simulated Pem Fuel Cell Environment.* Science and Technology of Advanced Materials, 2005. **6**(3-4): p. 282-289.

67. E. Fleury, J. Jayaraj, Y.C. Kim, H.K. Seok, K.Y. Kim, and K.B. Kim, *Fe-Based Amorphous Alloys as Bipolar Plates for Pem Fuel Cell.* Journal of Power Sources, 2006. **159**(1): p. 34-37.

68. A. Inoue, T. Shimizu, S. Yamaura, Y. Fujita, S. Takagi, and H. Kimura, *Development of Glassy Alloy Separators for a Proton Exchange Membrane Fuel Cell (Pemfc).* Materials Transactions, 2005. **46**: p. 1706 – 1710.

69. M.U. Kim, D.H. Kim, S.H. Han, E. Fleury, H.K. Seok, P.R. Cha, and Y.C. Kim, *Surface Modification by Carbon Ion Implantation for the Application of Ni-Based Amorphous Alloys as Bipolar Plate in Proton Exchange Membrane Fuel Cells.* Metals and Materials International, 2011. **17**: p. 283 – 289.

70. R.C. Sekol, G. Kumar, M. Carmo, F. Gittleson, N. Hardesty-Dyck, S. Mukherjee, J. Schroers, and A.D. Taylor, *Bulk Metallic Glass Micro Fuel Cell.* Small, 2013. **9**(12): p. 2081-2085, 2026.

71. Y. Aoki, Y. Fukunaga, H. Habazaki, and T. Kunitake, *Thin Film Fuel Cell Based on Nanometer-Thick Membrane of Amorphous Zirconium Phosphate Electrolyte.* Journal of The Electrochemical Society, 2011. **158**(8): p. B866.

72. K. Brunelli, M. Dabala, and M. Magrini, *Cu-Based Amorphous Alloy Electrodes for Fuel Cells.* Journal of Applied Electrochemistry, 2002. **32**: p. 145–148.

73. J. Barroso, Á.R. Pierna, T.C. Blanco, and J.J. del Val, *Electro-Oxidation of Ethanol and Bioethanol in Direct Alcohol Fuel Cells by Microparticulated Amorphous $Ni_{59}nb_{40}pt_{0.6}cu_{0.4}$ and $Ni_{59}nb_{40}pt_{0.6}cu_{0.2}sn_{0.2}$ Alloys.* Physica Status Solidi (a), 2011. **208**(10): p. 2309-2312.

74. S. Li, X. Yang, H. Zhu, Y. Chen, and Y. Liu, *Investigation of Amorphous Cob Alloy as the Anode Catalyst for a Direct Borohydride Fuel Cell.* Journal of Power Sources, 2011. **196**(14): p. 5858-5862.

75. P. Heo, T.Y. Kim, J. Ha, K.H. Choi, H. Chang, and S. Kang, *Intermediate-Temperature Fuel Cells with Amorphous $Sn_{0.9}in_{0.1}p_2o_7$ Thin Film Electrolytes.* Journal of Power Sources, 2012. **198**: p. 117-121.

76. P. Yi, L. Peng, L. Feng, P. Gan, and X. Lai, *Performance of a Proton Exchange Membrane Fuel Cell Stack Using Conductive Amorphous Carbon-Coated 304 Stainless Steel Bipolar Plates.* Journal of Power Sources, 2010. **195**(20): p. 7061-7066.

77. C. Breyer and A. Gerlach, *Global Overview on Grid-Parity.* Progress in Photovoltaics: Research and Applications, 2013. **21**(1): p. 121-136.

78. M. Brown. *Gaining on the Grid*. 2007; Available from: http://web.archive.org/web/20131127115307/http://www.bp.com/liveassets/bp_internet/globalbp/globalbp_uk_english/reports_and_publications/frontiers/STAGING/local_assets/pdf/bpf19_14-18_solar.pdf.

79. P. Kelly-Detwiler. *Solar Grid Parity Comes to Spain*. 2012; Available from: http://www.forbes.com/sites/peterdetwiler/2012/12/26/solar-grid-parity-comes-to-spain/.

80. B. Prior. *Cost and Lcoe by Generation Technology, 2009-2020*. 2011; Available from: http://www.greentechmedia.com/images/wysiwyg/research-blogs/GTM-LCOE-Analysis.pdf.

81. S. Ringbeck and J. Sutterlueti, *Bos Costs: Status and Optimization to Reach Industrial Grid Parity.* Progress in Photovoltaics: Research and Applications, 2013. **21**(6): p. 1411-1428.

82. C.-J. Yang, *Reconsidering Solar Grid Parity.* Energy Policy, 2010. **38**(7): p. 3270-3273.

83. B. Rech and H. Wagner, *Potential of Amorphous Silicon for Solar Cells.* Applied Physics A, 1999. **69**: p. 155–167.

84. M.A. Kreiger, D.R. Shonnard, and J.M. Pearce, *Life Cycle Analysis of Silane Recycling in Amorphous Silicon-Based Solar Photovoltaic Manufacturing.* Resources, Conservation and Recycling, 2013. **70**: p. 44-49.

85. B. Yan, J. Yang, and S. Guha, *Amorphous and Nanocrystalline Silicon Thin Film Photovoltaic Technology on Flexible Substrates.* Journal of Vacuum Science & Technology A: Vacuum, Surfaces, and Films, 2012. **30**(4): p. 04D108.

86. S. Adhikari, M.S. Kayastha, D.C. Ghimire, H.R. Aryal, S. Adhikary, T. Takeuchi, K. Murakami, Y. Kawashimo, H. Uchida, K. Wakita, and M. Umeno, *Improved Photovoltaic Properties of Heterojunction Carbon Based Solar Cell.* Journal of Surface Engineered Materials and Advanced Technology, 2013. **03**(03): p. 178-183.

87. M. Ma, Q. Xue, H. Chen, X. Zhou, D. Xia, C. Lv, and J. Xie, *Photovoltaic Characteristics of Pd Doped Amorphous Carbon Film/Sio_2/Si.* Applied Physics Letters, 2010. **97**(6): p. 061902.

88. T. Soga, T. Kondoh, N. Kishi, and Y. Hayashi, *Photovoltaic Properties of an Amorphous Carbon/Fullerene Junction.* Carbon, 2013. **60**: p. 1-4.

89. J. de Wild, A. Meijerink, J.K. Rath, W.G.J.H.M. van Sark, and R.E.I. Schropp, *Towards Upconversion for Amorphous Silicon Solar Cells.* Solar Energy Materials and Solar Cells, 2010. **94**(11): p. 1919-1922.

90. S. Zhao, S. Xu, G. Jia, D. Deng, L. Huang, and H. Wang, *Er^{3+}/Yb^{3+} Codoped Oxyfluoride Borosilicate Glass Ceramic Containing $Nayf_4$ Nanocrystals for Amorphous Silicon Solar Cells.* Materials Letters, 2011. **65**(15-16): p. 2407-2409.

91. O.E. Daif, E. Drouard, G. Gomard, A. Kaminski, A. Fave, M. Lemiti, S. Ahn, S. Kim, P.R. Cabarrocas, H. Jeon, and C. Seassal, *Absorbing One-Dimensional Planar Photonic Crystal for Amorphous Silicon Solar Cell.* Optics Express, 2010. **18**(S3): p. A293.

92. N. Dwivedi, S. Kumar, S. Singh, and H.K. Malik, *Oxygen Modified Diamond-Like Carbon as Window Layer for Amorphous Silicon Solar Cells.* Solar Energy, 2012. **86**(1): p. 220-230.

93. L. Hong, X. Wang, Rusli, H. Wang, H. Zheng, and H. Yu, *Crystallization and Surface Texturing of Amorphous-Si Induced by Uv Laser for Photovoltaic Application.* Journal of Applied Physics, 2012. **111**(4): p. 043106.

94. J. Kim and M. Kaviany, *Phonon-Coupling Enhanced Absorption of Alloyed Amorphous Silicon for Solar Photovoltaics.* Physical Review B, 2010. **82**(13).

95. T. Lanz, L. Fang, S.J. Baik, K.S. Lim, and B. Ruhstaller, *Photocurrent Increase in Amorphous Si Solar Cells by Increased Reflectivity of Lif/Al Electrodes.* Solar Energy Materials and Solar Cells, 2012. **107**: p. 259-262.

96. C. Martella, D. Chiappe, P. Delli Veneri, L.V. Mercaldo, I. Usatii, and F. Buatier de Mongeot, *Self-Organized Broadband Light Trapping in Thin Film Amorphous Silicon Solar Cells.* Nanotechnology, 2013. **24**(22): p. 225201.

97. I.s. Massiot, C.m. Colin, N. Péré-Laperne, P. Roca i Cabarrocas, C. Sauvan, P. Lalanne, J.-L. Pelouard, and S.p. Collin, *Nanopatterned Front Contact for*

Broadband Absorption in Ultra-Thin Amorphous Silicon Solar Cells. Applied Physics Letters, 2012. **101**(16): p. 163901.

98. F.-J. Tsai, J.-Y. Wang, J.-J. Huang, Y.-W. Kiang, and C.C. Yang, *Absorption Enhancement of an Amorphous Si Solar Cell through Surface Plasmon-Induced Scattering with Metal Nanoparticles.* Optics Express, 2010. **18**(S2): p. A208.

99. E. Fortunato, D. Ginley, H. Hosono, and D.C. Paine, *Transparent Conducting Oxides for Photovoltaics.* Materials Research Society Bulletin, 2007. **32**: p. 242-247.

100. S. Calnan and A.N. Tiwari, *High Mobility Transparent Conducting Oxides for Thin Film Solar Cells.* Thin Solid Films, 2010. **518**(7): p. 1839-1849.

101. C. Baratto, A. Ponzoni, M. Ferroni, L. Borgese, E. Bontempi, and G. Sberveglieri, *Sputtering Deposition of Amorphous Cadmium Stannate as Transparent Conducting Oxide.* Thin Solid Films, 2012. **520**(7): p. 2739-2744.

102. N. Zhou, D.B. Buchholz, G. Zhu, X. Yu, H. Lin, A. Facchetti, T.J. Marks, and R.P. Chang, *Ultraflexible Polymer Solar Cells Using Amorphous Zinc-Indium-Tin Oxide Transparent Electrodes.* Advanced Materials, 2014. **26**(7): p. 1098-1104.

103. S. Muthmann and A. Gordijn, *Amorphous Silicon Solar Cells Deposited with Non-Constant Silane Concentration.* Solar Energy Materials and Solar Cells, 2011. **95**(2): p. 573-578.

104. S. De Wolf, A. Descoeudres, Z.C. Holman, and C. Ballif, *High-Efficiency Silicon Heterojunction Solar Cells: A Review.* Green, 2012. **2**(1): p. 7-24.

105. L. Yu, B. O'Donnell, M. Foldyna, and P. Roca i Cabarrocas, *Radial Junction Amorphous Silicon Solar Cells on Pecvd-Grown Silicon Nanowires.* Nanotechnology, 2012. **23**(19): p. 194011.

106. S.Y. Myong and L.S. Jeon, *N-Type Amorphous Silicon-Based Bilayers for Cost-Effective Thin-Film Silicon Photovoltaic Devices.* Current Applied Physics, 2014. **14**(2): p. 151-155.

107. M.J. Powell, *The Physics of Amorphous-Silicon Thin-Film Transistors.* IEEE Transactions on Eelectron Devices, 1989. **36**(12): p. 2753-2763.

108. R.A. Street, *Thin-Film Transistors.* Advanced Materials, 2009. **21**(20): p. 2007-2022.

109. T. Minami, *Substitution of Transparent Conducting Oxide Thin Films for Indium Tin Oxide Transparent Electrode Applications.* Thin Solid Films, 2008. **516**(7): p. 1314-1321.

110. E.M.C. Fortunato, L.s.M.N. Pereira, P.M.C. Barquinha, A.M. Botelho do Rego, G.a. Gonçalves, A. Vilà, J.R. Morante, and R.F.P. Martins, *High Mobility Indium Free Amorphous Oxide Thin Film Transistors.* Applied Physics Letters, 2008. **92**(22): p. 222103.

111. E. Fortunato, P. Barquinha, and R. Martins, *Oxide Semiconductor Thin-Film Transistors: A Review of Recent Advances.* Advanced Materials, 2012. **24**(22): p. 2945-2986.

112. T. Minami, *Transparent Conducting Oxide Semiconductors for Transparent Electrodes.* Semiconductor Science and Technology, 2005. **20**(4): p. S35-S44.

113. S. Lee, B. Bierig, and D.C. Paine, *Amorphous Structure and Electrical Performance of Low-Temperature Annealed Amorphous Indium Zinc Oxide Transparent Thin Film Transistors.* Thin Solid Films, 2012. **520**(10): p. 3764-3768.

114. D.C. Paine, B. Yaglioglu, Z. Beiley, and S. Lee, *Amorphous Izo-Based Transparent Thin Film Transistors.* Thin Solid Films, 2008. **516**(17): p. 5894-5898.

115. S.-J. Seo, C.G. Choi, Y.H. Hwang, and B.-S. Bae, *High Performance Solution-Processed Amorphous Zinc Tin Oxide Thin Film Transistor.* Journal of Physics D: Applied Physics, 2009. **42**(3): p. 035106.

116. K. Nomura, H. Ohta, A. Takagi, T. Kamiya, M. Hirano, and H. Hosono, *Room-Temperature Fabrication of Transparent Flexible Thin-Film Transistors Using Amorphous Oxide Semiconductors.* Nature, 2004. **432**: p. 488-492.

117. T. Kamiya, K. Nomura, and H. Hosono, *Present Status of Amorphous in–Ga–Zn–O Thin-Film Transistors.* Science and Technology of Advanced Materials, 2010. **11**(4): p. 044305.

118. K. Nomura, A. Takagi, T. Kamiya, H. Ohta, M. Hirano, and H. Hosono, *Amorphous Oxide Semiconductors for High-Performance Flexible Thin-Film Transistors.* Japanese Journal of Applied Physics, 2006. **45**(5B): p. 4303-4308.

119. Dhananjay, C.-W. Chu, C.-W. Ou, M.-C. Wu, Z.-Y. Ho, K.-C. Ho, and S.-W. Lee, *Complementary Inverter Circuits Based on P-Sno_2 and N-In_2o_3 Thin Film Transistors.* Applied Physics Letters, 2008. **92**(23): p. 232103.

120. C.-W. Ou, Dhananjay, Z.Y. Ho, Y.-C. Chuang, S.-S. Cheng, M.-C. Wu, K.-C. Ho, and C.-W. Chu, *Anomalous P-Channel Amorphous Oxide Transistors Based on Tin Oxide and Their Complementary Circuits.* Applied Physics Letters, 2008. **92**(12): p. 122113.

121. G.-S. Heo, Y. Matsumoto, I.-G. Gim, H.-K. Lee, J.-W. Park, and T.-W. Kim, *Transparent Conducting Amorphous Zn–in–Sn–O Anode for Flexible Organic Light-Emitting Diodes.* Solid State Communications, 2010. **150**(3-4): p. 223-226.

122. Y. Kuo and C.-C. Lin, *A Light Emitting Device Made from Thin Zirconium-Doped Hafnium Oxide High-K Dielectric Film with or without an Embedded Nanocrystal Layer.* Applied Physics Letters, 2013. **102**(3): p. 031117.

123. C.-C. Lin and Y. Kuo, *White Light Emission from Ultrathin Tungsten Metal Oxide Film.* Journal of Vacuum Science & Technology B: Microelectronics and Nanometer Structures, 2014. **32**(1): p. 011208.

124. N.-M. Park, T.-S. Kim, and S.-J. Park, *Band Gap Engineering of Amorphous Silicon Quantum Dots for Light-Emitting Diodes.* Applied Physics Letters, 2001. **78**(17): p. 2575-2577.

125. R. Reyes, C. Legnani, M. Cremona, H.F. Brito, R. Távora Britto, and C.A. Achete, *Amorphous Carbon Nitride Thin Films as Buffer Layer in Organic Leds.* physica status solidi (c), 2004. **1**(S2): p. S229-S235.

126. R.-H. Yeh, G.-H. Chen, S.-Y. Lo, and J.-W. Hong, *Hydrogenated Amorphous Silicon Carbide Alternating-Current Thin-Film Light-Emitting Diodes.* Journal of The Electrochemical Society, 2007. **154**(8): p. H687-H690.

127. T.-J. Chen and C.-L. Kuo, *Structural, Electronic, and Dielectric Properties of Amorphous Hafnium Silicates.* Journal of Applied Physics, 2011. **110**(11): p. 114105.

128. J. Robertson, *High Dielectric Constant Gate Oxides for Metal Oxide Si Transistors.* Reports on Progress in Physics, 2006. **69**(2): p. 327-396.

129. Y. Wang, F. Zahid, J. Wang, and H. Guo, *Structure and Dielectric Properties of Amorphous High-Kappa Oxides Hfo_2, Zro_2 and Their Alloys.* Physical Review B, 2012. **85**(22): p. 5-9.

130. G.D. Wilk, R.M. Wallace, and J.M. Anthony, *Hafnium and Zirconium Silicates for Advanced Gate Dielectrics.* Journal of Applied Physics, 2000. **87**(1): p. 484-492.

131. L. Yuan, X. Zou, G. Fang, J. Wan, H. Zhou, and X. Zhao, *High-Performance Amorphous Indium Gallium Zinc Oxide Thin-Film Transistors with Hf $O_x N_y$ /Hf O_2 /Hf $O_x N_y$ Tristack Gate Dielectrics.* IEEE Electron Device Letters, 2011. **32**(1): p. 42-44.

132. M. Watanabe, M. Kanno, and E. Okunishi, *Atomic-Resolution Elemental Mapping by Eels and Xeds in Aberration Corrected Stem.* JEOL News, 2010. **45**(1): p. 8-15.

133. O.L. Krivanek, M.F. Chisholm, V. Nicolosi, T.J. Pennycook, G.J. Corbin, N. Dellby, M.F. Murfitt, C.S. Own, Z.S. Szilagyi, M.P. Oxley, S.T. Pantelides, and S.J. Pennycook, *Atom-by-Atom Structural and Chemical Analysis by Annular Dark-Field Electron Microscopy.* Nature, 2010. **464**: p. 571-574.

134. O.L. Krivanek, P.H. Gaskell, and A. Howie, *Seeing Order in 'Amorphous' Materials.* Nature, 1976. **262**: p. 454 - 457

135. M.M.J. Treacy, J.M. Gibson, L. Fan, D.J. Paterson, and I. McNulty, *Fluctuation Microscopy: A Probe of Medium Range Order.* Reports on Progress in Physics, 2005. **68**(12): p. 2899-2944.

136. S.L. Cheng, H.H. Lin, J.H. He, T.F. Chiang, C.H. Yu, L.J. Chen, C.K. Yang, D.Y. Wu, S.C. Chien, and W.C. Chen, *Evolution of Structural Order in Germanium Ion-Implanted Amorphous Silicon Layers.* Journal of Applied Physics, 2002. **92**(2): p. 910.

137. G.Y. Fan and J.M. Cowley, *Assessing the Information Content of Hrem Images.* Ultramicroscopy, 1988. **24**: p. 49-60.

138. A. Howie, *High Resolution Electron Microscopy of Amorphous Thin Films.* Journal of Non-Crystalline Solids, 1978. **31**: p. 41-55.

139. R. Egerton, *Electron Energy-Loss Spectroscopy in the Electron Microscope*. 3 ed., New York: Springer.

140. F. Lytle, D. Sayers, and E. Stern, *Extended X-Ray-Absorption Fine-Structure Technique. Ii. Experimental Practice and Selected Results.* Physical Review B, 1975. **11**(12): p. 4825-4835.

141. A.D. Cicco, A. Bianconi, C. Coluzza, and P. Rudolf, *Xanes Study of Structural Disorder in Amorphous Silicon.* Journal of Non-Crystalline Solids, 1990. **116**: p. 27-32.

142. P.J. Durham, J.B. Pendry, and C.H. Hodges, *Xanes: Determination of Bond Angles and Multi-Atom Correlations in Order and Disordered Systems.* Solid State Communications, 1981. **38**: p. 159-162.

143. F.M. Alamgir, H. Jain, D.B. Williams, and R.B. Schwarz, *The Structure of a Metallic Glass System Using Exelfs and Exafs as Complementary Probes.* Micron, 2003. **34**(8): p. 433-439.

144. J. Dixmier, P. Derouet, M. Essamet, and M. Laridjani, *Structural, Optical and Transport Properties of Sputtered Hydrogenated Amorphous Silicon Films in Relation to Si-H Bonding Configurations.* Philosophical Magazine Part B, 2006. **52**(5): p. 943-954.

145. D. Wang, Y. Li, H. Wei, C. Tang, H. Yan, and S.Huang, *Influence of Annealing on the Physical Properties and Atomic Structure of a-Si: H Films.* Journal of Non-Crystalline Solids, 1987. **95 & 96**: p. 841 - 848.

146. D.J.H. Cockayne and D.R. McKenzie, *Electron Diffraction Analysis of Polycrystalline and Amorphous Thin Films.* Acta Crystallographica, 1988. **A44**: p. 870–878.

147. S.R. Elliott, *Physics of Amorphous Materials*. 2 ed. 1990, Burnt Mill, Harlow, Essex, England: Longman Scientific & Technical.

148. Y.W. Bai, X.F. Bian, X.Q. Lv, S.P. Pan, J.Y. Qin, X.B. Qin, and L.N. Hu, *Heredity of Medium-Range Order Structure from Melts to Amorphous Solids.* Journal of Applied Physics, 2012. **112**(8): p. 083524.

149. U. Hoppe, G. Walter, R.K. Brow, and N.P. Wyckoff, *Structure of Potassium Germanophosphate Glasses by X-Ray and Neutron Diffraction: 2. Medium-Range Order*. Journal of Non-Crystalline Solids, 2008. **354**(29): p. 3400-3407.

150. L. Zhang, Y. Wu, X. Bian, H. Li, W. Wang, and S. Wu, *Short-Range and Medium-Range Order in Liquid and Amorphous $Al_{90}fe_5ce_5$ Alloys.* Journal of Non-Crystalline Solids, 2000. **262**: p. 169-176.

151. P. Lamparter and S. Steeb, *Small Angle X-Ray and Neutron Scattering for the Investigation of the Medium-Range Structure of Metallic Glasses.* Journal of Non-Crystalline Solids 1988. **106**(137-146).

152. S.-I. Muramatsu, H. Kajiyama, H. Itoh, S. Matsubara, and T. Shimada, *Structural Investigation of Hydrogenated Amorphous Silicon.* Photovoltaic Specialists Conference, 1988. **1**: p. 61 - 66.

153. R. Xie, G.G. Long, S.J. Weigand, S.C. Moss, T. Carvalho, S. Roorda, M. Hejna, S. Torquato, and P.J. Steinhardt, *Hyperuniformity in Amorphous Silicon Based on the Measurement of the Infinite-Wavelength Limit of the Structure Factor.* Proceedings of the National Academy of Sciences of the United States of America, 2013. **110**(33): p. 13250-13254.

154. W.J. Malfait, W.E. Halter, and R. Verel, *^{29}Si Nmr Spectroscopy of Silica Glass: T_1 Relaxation and Constraints on the Si–O–Si Bond Angle Distribution.* Chemical Geology, 2008. **256**(3-4): p. 269-277.

155. F. Mauri, A. Pasquarello, B.G. Pfrommer, Y.-G. Yoon, and S.G. Louie, *Si-O-Si Bond-Angle Distribution in Vitreous Silica from First-Principles ^{29}Si Nmr Analysis.* Physical Review B, 2000. **62**(9): p. R4786-R4789.

156. J.V. Smith, C.S. Blackwell, and G.L. Hovis, *Nmr of Albite–Microcline Series.* Nature, 1984. **309**(10): p. 140-142.

157. W.J. Malfait, W.E. Halter, Y. Morizet, B.H. Meier, and R. Verel, *Structural Control on Bulk Melt Properties: Single and Double Quantum ^{29}si Nmr Spectroscopy on Alkali-Silicate Glasses.* Geochimica et Cosmochimica Acta, 2007. **71**(24): p. 6002-6018.

158. J.M. Egan, R.M. Wenslow, and K.T. Mueller, *Mapping Aluminumphosphorus Connectivities in Aluminophosphate Glasses.* Journal of Non-Crystalline Solids, 2000. **261**: p. 115-126.

159. D. Beeman, R. Tsu, and M. Thorpe, *Structural Information from the Raman Spectrum of Amorphous Silicon.* Physical Review B, 1985. **32**(2): p. 874-878.

160. V.K. Kudoyarova, O.I. Konkov, E.I. Terukov, A.P. Sokolov, and A.P. Shebanin, *Correlation of Raman Spectra with Optical and Electronic Properties of a-Si: H.* Journal of Non-Crystalline Solids, 1989. **114**: p. 205-207.

161. S. Muthmann, F. Köhler, R. Carius, and A. Gordijn, *Structural Order on Different Length Scales in Amorphous Silicon Investigated by Raman Spectroscopy.* Physica Status Solidi (a), 2010. **207**(3): p. 544-547.

162. P.M. Voyles, N. Zotov, S.M. Nakhmanson, D.A. Drabold, J.M. Gibson, M.M.J. Treacy, and P. Keblinski, *Structure and Physical Properties of Paracrystalline Atomistic Models of Amorphous Silicon.* Journal of Applied Physics, 2001. **90**(9): p. 4437.

163. V.N. Novikov and A.P. Sokolov, *A Correlation between Low-Energy Vibrational Spectra and First Sharp Diffraction Peak in Chalcogenide Glasses.* Solid State Communications, 1991. **77**(3): p. 243-247.

164. A.P. Sokolov, A. Kisliuk, M. Soltwisch, and D. Quitmann, *Medium-Rnage Order in Glasses Comparison of Raman and Diffraction Measurments.* Physical Review Letters, 1992. **69**(10).

165. H. Tanaka, *Physical Origin of the Boson Peak Deduced from a Two-Order-Parameter Model of Liquid.* Journal of the Physical Society of Japan, 2001. **70**: p. 1178-1181.

166. V.K. Malinovsky, V.N. Novikov, N.V. Surovtsev, and A.P. Shebanin, *Investigation of Amorphous States of Si O_2 by Raman Scattering Spectroscopy.* Physics of the Solid State, 2000. **42**(1): p. 65–71.

167. R. Tsu, J. Gonzalez-Hernandez, J. Doehler, and S.R. Ovshinsky, *Order Prameters in a-Si Systems.* Solid State Communications, 1983. **46**(1): p. 79-82.

168. M.M.J. Treacy and J.M. Gibson, *Variable Coherence Microscopy: A Rich Source of Structural Information from Disordered Materials.* Acta Crystallographica, 1996. **A52**: p. 212-220.

169. P.M. Voyles and J.R. Abelson, *Medium-Range Order in Amorphous Silicon Measured by Fluctuation Electron Microscopy.* Solar Energy Materials and Solar Cells, 2003. **78**(1-4): p. 85-113.

170. J.M. Gibson and M.M.J. Treacy, *Diminished Medium-Range Order Observed in Annealed Amorphous Germanium.* Physical Review Letters, 1997. **78**(6): p. 1074-1077.

171. P.M. Voyles and D.A. Muller, *Fluctuation Microscopy in the Stem.* Ultramicroscopy, 2002. **93**: p. 147–159.

172. J.M. Gibson, M.M.J. Treacy, T. Sun, and N.J. Zaluzec, *Substantial Crystalline Topology in Amorphous Silicon.* Physical Review Letters, 2010. **105**(12): p. 125504.

173. J.M. Gibson, M.M.J. Treacy, P.M. Voyles, H.C. Jin, and J.R. Abelson, *Structural Disorder Induced in Hydrogenated Amorphous Silicon by Light Soaking.* Applied Physics Letters, 1998. **73**(21): p. 3093.

174. S.N. Bogle, P.M. Voyles, S.V. Khare, and J.R. Abelson, *Quantifying Nanoscale Order in Amorphous Materials: Simulating Fluctuation Electron Microscopy of Amorphous Silicon.* Journal of Physics: Condensed Matter, 2007. **19**(45): p. 455204.

175. M.M.J. Treacy, J.M. Gibson, and P.J. Keblinski, *Paracrystallites Found in Evaporated Amorphous Tetrahedral Semiconductors.* Journal of Non-Crystalline Solids, 1998. **231**: p. 99-110.

176. P. Voyles, J. Gerbi, M. Treacy, J. Gibson, and J. Abelson, *Absence of an Abrupt Phase Change from Polycrystalline to Amorphous in Silicon with Deposition Temperature.* Physical Review Letters, 2001. **86**(24): p. 5514-5517.

177. W.G. Stratton, J. Hamann, J.H. Perepezko, P.M. Voyles, X. Mao, and S.V. Khare, *Aluminum Nanoscale Order in Amorphous $Al_{92}sm_8$ Measured by Fluctuation Electron Microscopy.* Applied Physics Letters, 2005. **86**(14): p. 141910.

178. J.-Y. Cheng, *Diffraction Microscopy for Disordered Tetrahedral Networks.* Journal of Applied Physics, 2004. **95**(12): p. 7779.

179. J. Hwang, A.M. Clausen, H. Cao, and P.M. Voyles, *Reverse Monte Carlo Structural Model for a Zirconium-Based Metallic Glass Incorporating Fluctuation Microscopy Medium-Range Order Data.* Journal of Materials Research, 2011. **24**(10): p. 3121-3129.

180. J. Li, X. Gu, and T.C. Hufnagel, *Using Fluctuation Microscopy to Characterize Structural Order in Metallic Glasses.* Microsc Microanal, 2003. **9**(6): p. 509-515.

181. G. Zhao, M.M.J. Treacy, and P.R. Buseck, *Fluctuation Electron Microscopy of Medium-Range Order in Ion-Irradiated Zircon.* Philosophical Magazine, 2010. **90**(35-36): p. 4661-4677.

182. A. Liu, R. Arenal, and X. Chen, *Clustering in a Highly Hydrogenated Diamondlike Carbon Determined Using Fluctuation Electron Microscopy and Phenomenological Atomistic Simulations.* Physical Review B, 2007. **76**(12): p. 121401R.

183. X. Chen, J.P. Sullivan, T.A. Friedmann, and J.M. Gibson, *Fluctuation Microscopy Studies of Medium-Range Ordering in Amorphous Diamond-Like Carbon Films.* Applied Physics Letters, 2004. **84**(15): p. 2823.

184. G. Zhao, P.R. Buseck, A. Rougee, and M.M. Treacy, *Medium-Range Order in Molecular Materials: Fluctuation Electron Microscopy for Detecting Fullerenes in Disordered Carbons.* Ultramicroscopy, 2009. **109**(2): p. 177-188.

185. A. Liu, R. Arenal, D. Miller, X. Chen, J. Johnson, O. Eryilmaz, A. Erdemir, and J. Woodford, *Structural Order in near-Frictionless Hydrogenated Diamondlike Carbon Films Probed at Three Length Scales Via Transmission Electron Microscopy.* Physical Review B, 2007. **75**(20): p. 205402.

186. M.Y. Ho, H. Gong, G.D. Wilk, B.W. Busch, M.L. Green, P.M. Voyles, D.A. Muller, M. Bude, W.H. Lin, A. See, M.E. Loomans, S.K. Lahiri, and P.I. Räisänen, *Morphology and Crystallization Kinetics in Hfo_2 Thin Films Grown by Atomic Layer Deposition.* Journal of Applied Physics, 2003. **93**(3): p. 1477.

187. M.M. Treacy and K.B. Borisenko, *The Local Structure of Amorphous Silicon.* Science, 2012. **335**(6071): p. 950-953.

188. P. Biswas, D.N. Tafen, and D. Drabold, *Experimentally Constrained Molecular Relaxation: The Case of Glassy $Gese_2$.* Physical Review B, 2005. **71**(5): p. 054204.

189. M.M.J. Treacy and J.M. Gibson, *Coherence and Multiple Scattering in "Z-Contrast" Images.* Ultramicroscopy, 1993. **52**: p. 31-51.

190. K.B. Borisenko, B. Haberl, A.C.Y. Liu, Y. Chen, G. Li, J.S. Williams, J.E. Bradby, D.J.H. Cockayne, and M.M.J. Treacy, *Medium-Range Order in Amorphous Silicon Investigated by Constrained Structural Relaxation of Two-Body and Four-Body Electron Diffraction Data.* Acta Materialia, 2012. **60**(1): p. 359-375.

191. P. Biswas, R. Atta-Fynn, and D.A. Drabold, *Reverse Monte Carlo Modeling of Amorphous Silicon.* Physical Review B, 2004. **69**: p. 195207.

192. J.W. Goodman, *Probability Density Function of the Sum of N Partially Correlated Speckle Patterns.* Optics Communications, 1975. **13**(3): p. 244-247.

193. M.M.J. Treacy and J.M. Gibson, *Statistics of Partially Coherent Dark-Field Images of Amorphous Materials*, in *Electron Microscopy and Analysis, Institute of Physics Conference Series 153,* J.M. Rodenburg, Editor 1997. p. 433–436.

194. M.M. Treacy and J.M. Gibson, *Examination of a Polycrystalline Thin-Film Model to Explore the Relation between Probe Size and Structural Correlation Length in Fluctuation Electron Microscopy.* Microsc Microanal, 2012. **18**(1): p. 241-253.

195. C.E. Shannon, *A Mathematical Theory of Communication.* The Bell System Technical Journal, 1948. **27**: p. 379-423, 623-656.

196. M.M.J. Treacy, *Speckles in Images and Diffraction Patterns*, in *Hnadbook of Nanoscopy,* G.V. Tendeloo, D.V. Dyck, and S.J. Pennycook, Editors. 2012, John Wiley & Sons. p. 405-435.

197. P. Chaudhari, J. Graczyk, and H. Charbnau, *Coherent Scattering in a Random-Network Model for Amorphous Solids.* Physical Review Letters, 1972. **29**(7): p. 425-429.

198. A. Howie, O.L. Krivanek, and M.L. Rudee, *Interpretation of Electron Micrographs and Diffraction Patterns of Amorphous Materials.* Philosophical Magazine, 1973. **27**(1): p. 235-255.

199. T.T. Li, S.N. Bogle, and J.R. Abelson, *Quantitative Fluctuation Electron Microscopy in the Stem: Methods to Identify, Avoid, and Correct for Artifacts.* Microscopy and Microanalysis, 2014. **20**(5): p. 1605-1618.

200. A. Rezikyan, Z. Jibben, B.A. Rock, G. Zhao, F.A.M. Koeck, R.F. Nemanich, and M.M.J. Treacy, *Speckle Suppression by Decoherence in Fluctuation Electron Microscopy.* Microscopy and Microanalysis, 2015(submitted).

201. A. Howie, *Mechanisms of Decoherence in Electron Microscopy.* Ultramicroscopy, 2011. **111**(7): p. 761-767.

202. M. Wanner, D. Bach, D. Gerthsen, R. Werner, and B. Tesche, *Electron Holography of Thin Amorphous Carbon Films: Measurement of the Mean Inner Potential and a Thickness-Independent Phase Shift.* Ultramicroscopy, 2006. **106**(4-5): p. 341-345.

203. L. Reimer and H. Kohl., *Transmission Electron Microscopy: Physics of Image Formation*. 2008, New York: Springer.

204. A. Rezikyan, J.A. Belcourt, and M.M.J. Treacy, *Interferometric Diffraction from Amorphous Bilayers.* Microscopy and Microanalysis, 2015(submitted).

205. F.A.M. Koeck and R.J. Nemanich, *Low Temperature Onset for Thermionic Emitters Based on Nitrogen Incorporated Uncd Films.* Diamond and Related Materials, 2009. **18**(2-3): p. 232-234.

206. T. Sun, F.A.M. Koeck, A. Rezikyan, M.M.J. Treacy, and R.J. Nemanich, *Thermally Enhanced Photoinduced Electron Emission from Nitrogen-Doped Diamond Films on Silicon Substrates.* Physical Review B, 2014. **90**(12): p. 121302(R).

207. T. Sun, F.A.M. Koeck, C. Zhu, and R.J. Nemanich, *Combined Visible Light Photo-Emission and Low Temperature Thermionic Emission from Nitrogen Doped Diamond Films.* Applied Physics Letters, 2011. **99**(20): p. 202101.

208. J. van der Weide, Z. Zhang, P. Baumann, M. Wensell, J. Bernholc, and R. Nemanich, *Negative-Electron-Affinity Effects on the Diamond (100) Surface.* Physical Review B, 1994. **50**(8): p. 5803-5806.

209. P. Gröning, O. Gröning, L.-O. Nilsson, and L. Schlapbach, *Properties and Characterization of Chemical Vapor Deposition Diamond Field Emitters.* Solid State Electronics, 2001. **45**: p. 929-944.

210. J.E. Yater and A. Shih, *Secondary Electron Emission Characteristics of Single-Crystal and Polycrystalline Diamond.* Journal of Applied Physics, 2000. **87**(11): p. 8103.

211. F.Lukes, *Oxidation of Si and Gaas in Air at Room Temperature.* Surface Science, 1972. **30**: p. 91-100.

212. M.J. Kim and R.W. Carpenter, *Composition and Structure of Native Oxide on Silicon by High Resolution Analytical Electron Microscopy* Journal of Materials Research, 1990. **5**(2): p. 348-351.

213. H.R. Philipp, *An Optical Characterization of Native Oxides and Thin Thermal Oxides on Silicon.* Journal of Applied Physics, 1982. **53**(7): p. 5224.

214. J.M. Rodenburg, *Ptychography and Related Diffractive Imaging Methods.* Advances in Imaging and Electron Physics, 2008. **150**: p. 87-184.

215. A.M. Maiden, M.J. Humphry, F. Zhang, and J.M. Rodenburg, *Superresolution Imaging Via Ptychography.* Journal of the Optical Society of America, 2011. **28**(4): p. 604-612.

216. M.J. Humphry, B. Kraus, A.C. Hurst, A.M. Maiden, and J.M. Rodenburg, *Ptychographic Electron Microscopy Using High-Angle Dark-Field Scattering for Sub-Nanometre Resolution Imaging.* Nature Communications, 2012. **3**: p. 730.

217. O. Kamimura and T. Dobashi, *Low-Energy Electron Diffractive Imaging for Three Dimensional Light-Element Materials.* Hitachi Review, 2012. **61**(6): p. 269-273.

218. O. Kamimura, T. Dobashi, K. Kawahara, T. Abe, and K. Gohara, *10-Kv Diffractive Imaging Using Newly Developed Electron Diffraction Microscope.* Ultramicroscopy, 2010. **110**(2): p. 130-133.

219. F. Hüe, J.M. Rodenburg, A.M. Maiden, F. Sweeney, and P.A. Midgley, *Wave-Front Phase Retrieval in Transmission Electron Microscopy Via Ptychography.* Physical Review B, 2010. **82**(12): p. 121415(R).

APPENDIX A

GAMMA DISTRIBUTION DERIVATION FROM THE PRINCIPLE OF MAXIMUM ENTROPY

The standard Lagrange multiplier method applied to maximize the function $S = -\int P \ln(P) dI$ subject to the constraints, which are given by equations $c_i = \int g_i(I) P(I) dI$, yields

$$P(I) = \exp\left[-\lambda_0 - \sum_{i=2}^{n} \lambda_i g_i(I) \right]. \tag{A1}$$

with $\lambda_0 = \lambda_1 + 1$. If the constrains along with the normalization condition are given by the expressions

$$\int_0^\infty P(I) dI = 1, \tag{A2}$$

$$\int_0^\infty I \; P(I) dI = \langle I \rangle, \tag{A3}$$

$$\int_0^\infty \ln I \; P(I) dI = \langle \ln I \rangle. \tag{A4}$$

then the equation (A1) can be rewritten as

$$P(I) = \exp\left[-\lambda_0 - \lambda_2 I - \lambda_3 \ln I \right]. \tag{A5}$$

The λ_0 can then be expressed in terms of λ_2 and λ_3 by inserting (A5) into (A2)

$$\exp(\lambda_0) = \int_0^\infty \exp\left[-\lambda_2 I - \lambda_3 \ln I \right] dI \, . \tag{A6}$$

$$\lambda_0 = \ln \int_0^\infty \exp\left[-\lambda_2 I - \lambda_3 \ln I \right] dI = \ln \int_0^\infty I^{-\lambda_3} \exp\left[-\lambda_2 I \right] dI \, . \tag{A7}$$

or

$$\lambda_0 = (\lambda_3 - 1) \ln \lambda_2 - \ln(\Gamma(1 - \lambda_3)), \tag{A8}$$

where I used the table integral $\int_0^\infty x^n \exp\left(-ax^b\right)dx = \frac{1}{b}a^{-\frac{n+1}{b}}\Gamma\left(\frac{n+1}{b}\right)$. Inserting (A8) into (A6) yields

$$P(I) = \frac{\lambda_2^{1-\lambda_3}}{\Gamma(1-\lambda_3)} I^{-\lambda_3} \exp\left(-\lambda_2 I\right). \tag{A9}$$

At this point it is necessary to obtain Lagrange multipliers λ_2 and λ_3 in terms of constraints c_i. Differentiating (A7) results in $\frac{\partial \lambda_0}{\partial \lambda_2} = \frac{\int_0^\infty I \exp\left[-\lambda_2 I - \lambda_3 \ln I\right]dI}{\int_0^\infty \exp\left[-\lambda_2 I - \lambda_3 \ln I\right]dI}$ and $\frac{\partial \lambda_0}{\partial \lambda_3} = \frac{\int_0^\infty \ln I \exp\left[-\lambda_2 I - \lambda_3 \ln I\right]dI}{\int_0^\infty \exp\left[-\lambda_2 I - \lambda_3 \ln I\right]dI}$. Note that the integrals in the denominators are equal to $\exp(\lambda_0)$ (see (A6)), so $\frac{\partial \lambda_0}{\partial \lambda_2} = \int_0^\infty I \exp\left[-\lambda_0 - \lambda_2 I - \lambda_3 \ln I\right]dI$ and $\frac{\partial \lambda_0}{\partial \lambda_3} = \int_0^\infty \ln I \exp\left[-\lambda_0 - \lambda_2 I - \lambda_3 \ln I\right]dI$. Invoking (A5) I get

$$\frac{\partial \lambda_0}{\partial \lambda_2} = -\left\langle I \right\rangle, \tag{A10}$$

$$\frac{\partial \lambda_0}{\partial \lambda_3} = -\left\langle \ln I \right\rangle. \tag{A11}$$

Also from (A8)

$$\frac{\partial \lambda_0}{\partial \lambda_2} = \frac{\lambda_3 - 1}{\lambda_2}, \tag{A12}$$

$$\frac{\partial \lambda_0}{\partial \lambda_3} = \ln \lambda_2 + \frac{1}{\Gamma(1-\lambda_3)} \frac{\partial}{\partial \lambda_3} \Gamma(1-\lambda_3) = \ln \lambda_2 - \psi(1-\lambda_3), \tag{A13}$$

where ψ is the Digamma function defined as $\psi(x) = \frac{1}{\Gamma(x)} \frac{\partial}{\partial x} \Gamma(x)$. Further, comparing (A11) and (A10) with (A13) and (A12) respectively, I get

$$\ln \lambda_2 - \psi(1-\lambda_3) = -\langle \ln I \rangle, \text{ and} \tag{A14}$$

$$\frac{1-\lambda_3}{\lambda_2} = \langle I \rangle. \tag{A15}$$

Taking the logarithm of both sides of the (A15) and combining with (A14) in order to eliminate $\ln \lambda_2$, the following expression is finally derived

$$\psi(1-\lambda_3) - \ln(1-\lambda_3) = \langle \ln I \rangle - \ln \langle I \rangle, \tag{A16}$$

which together with (A15), links the Lagrange multipliers with the constraints. Note that the expression (A9), derived here using the Lagrange multipliers method, turns into the general expression for the Gamma distribution if I redefine the multipliers λ_2 and λ_3, as follows $b \equiv 1-\lambda_3$ and $a \equiv 1/\lambda_2$. Indeed,

$$P(I) = \frac{1}{a\Gamma(b)} \left(\frac{I}{a} \right)^{b-1} \exp\left(-\frac{I}{a} \right). \tag{A17}$$

Moreover, equations (A15) and (A16) turn into

$$ab = \langle I \rangle, \text{ and} \tag{A18}$$

$$\psi(b) - \ln b = \langle \ln I \rangle - \ln \langle I \rangle. \tag{A19}$$